

# **DESIGN AND DEVELOPMENT OF MULTIFUNCTIONAL ENERGY HARVESTING AND STORAGE SYSTEMS FOR SENSOR APPLICATIONS**

**By**

**Noaman Makki**

A Thesis Submitted in Partial Fulfillment  
of the Requirements for the Degree of

Masters of Applied Science  
In  
Mechanical Engineering

The Faculty of Engineering and Applied Science  
University of Ontario Institute of Technology

June 2011

© Noaman Makki

# **DESIGN AND DEVELOPMENT OF MULTIFUNCTIONAL ENERGY HARVESTING AND STORAGE SYSTEMS FOR SENSOR APPLICATIONS**

**Noaman Makki**

Degree of Master of Applied Science, 2011  
Faculty of Engineering and Applied Science  
University of Ontario Institute of Technology

## **ABSTRACT**

This research focuses on the design and development of multifunctional components intended to provide three basic functions: (i) power generation, (ii) power storage, and (iii) structural support. They are made of composite multi-material systems that include smart materials. By combining various functions into the same component significant performance, weight, space, assembly and packing benefits can be achieved. A major portion of this thesis is devoted to the use of piezoelectric layers in order to generate few milliwatts of power and enhance the utility of electrical mobility products and subsystems while facilitating new venues for implementing such devices. Shoes and pneumatic tires were used to harvest energy from their innate motion and various useful applications of harvested energy have been demonstrated in the form of sensors and power sources for larger devices.

Shoe-based power generation can be used for charging Radio Frequency IDentification (RFID) tags, GPS sensors, portable electronics, etc. Tire-based power generation can be used for powering battery-less wireless Tire Pressure Monitoring Systems (TPMS), wireless Vehicle Speed Sensors (VSS), tire health monitoring sensors, etc. Fully functional proof-of-product prototypes of a variety of multifunctional components were developed and subjected to experimentation and testing using custom designed and built lab-scale made experimental machinery. Contrary to the paradigm, the possibility of using piezoelectric materials in automotive tires to produce few watts of power ( $>2$  watts) has been successfully demonstrated with applications ranging from powering more demanding sensors to onboard batteries. An Electronic Vehicle Control System (EVCS) with electronic differential and cruise control capabilities has also been designed, developed and tested on the Extended Range Plug-In Hybrid vehicle previously developed at UOIT.

*To my family, most of all my parents, Haji Makki and Zaibun  
Makki for their unfathomable support and sacrifices without  
which this would not have been possible*

*Thou didst create the night, but I made the lamp.  
Thou didst create clay, but I made the cup.  
Thou didst create the deserts, mountains and forests,  
I produced the orchards, gardens and groves.  
It is I who made the glass out of stone,  
And it is I who turn a poison into an antidote*

*Sir Allama Muhammad Iqbal*

**CERTIFICATE OF APPROVAL**

## **ACKNOWLEDGEMENTS**

First of all, I would like to thank the Creator for the countless blessings, opportunities and experiences that have made me the person I am today, for which I am ever grateful.

I would like to express my gratitude and appreciation to Dr. Remon Pop-Iliev for his continuous technical, financial and moral support during the course of my graduate studies. For having the trust and confidence in me and for considering me worthy of working under his supervision even beyond graduate level.

I would like to thank Mr. Naveed Khan and Mr. Harris Mushtaq for their valuable help with the Dune Buggy project and assistance in various projects related issues.

I would also like to Acknowledge Mr. Hidayat Shahid, Mr. Mike McLeod and Mr. Ali Sherazee for their support in the designing of various Dune Buggy Components.

## TABLE OF CONTENTS

ABSTRACT.....	II
CERTIFICATE OF APPROVAL .....	IV
ACKNOWLEDGEMENTS.....	V
LIST OF FIGURES.....	V
LIST OF TABLES.....	IX
NOMENCLATURE.....	X
<b>1    <i>Chapter 1:</i> BACKGROUND INFORMATION .....</b>	<b>1</b>
1.1    INTRODUCTION.....	1
1.2    MULTIFUNCTIONAL MATERIALS .....	2
1.3    SMART MATERIALS .....	3
1.3.1    Classification of Smart Materials .....	3
1.4    PIEZOELECTRIC MATERIALS.....	4
1.4.1    Synthesis of Lead Zirconate Titanate (PZT) Piezoelectric materials.....	5
1.4.2    Origin of Piezoelectricity .....	5
1.4.3    PZT Element types – polarization.....	7
1.5    POLYVINYLIDENE FLORIDE (PVDF) .....	11
1.6    COMPARISON BETWEEN PVDF AND PZT .....	12
1.7    SOME PIEZOELECTRIC CONSTANTS.....	12
1.8    APPROXIMATION OF PIEZOELECTRIC BEHAVIOUR .....	14
<b>2    <i>Chapter 2:</i> TESTING AND EXPERIMENTATION SETUP .....</b>	<b>15</b>
2.1    CONDITIONING AND STORAGE OF HARVESTED POWER .....	15
2.2    CAPACITOR CHARGING .....	15
2.3    BATTERY CHARGING .....	16
2.3.1    Nickel Metal Hydride (NiMH) Battery .....	16
2.3.2    Lithium-Ion (Li-Ion) Battery.....	17
2.4    TESTING EQUIPMENT - DYNAMOMETER .....	18
2.5    COMMUTATOR ASSEMBLY .....	22
<b>3    <i>Chapter 3:</i> LITERATURE SURVEY.....</b>	<b>23</b>
3.1    PIEZOELECTRIC POWER HARVESTING SHOES .....	23
3.1.1    Power generating Insole Insert .....	23

3.1.2	PVDF shoe-heel insert.....	24
3.1.3	Microstructured polymer shoe-heel insert.....	25
3.2	POWER GENERATION IN TIRES .....	26
3.2.1	PZT Impact Energy Harvesting .....	26
3.2.2	Electromagnetic Power Generation in wheels .....	27
3.2.3	Piezoelectric Power Generation in wheels .....	29
3.2.4	System for generating power inside the tire using piezoelectric cable .....	30
3.3	TIRE PRESSURE MONITORING SYSTEM (TPMS) SENSORS: .....	31
3.3.1	Batteryless TPMS based on contactless energy transfer:.....	33
3.3.2	Batteryless TPMS based on Radio Frequency Identification (RFID) technology....	33
3.3.3	Batteryless TPMS based on Piezoelectric harvesting .....	34
3.4	VEHICLE SPEED SENSOR .....	35
3.5	SCOPE OF WORK .....	36
4	<i>Chapter 4: SHOE-BASED MULTIFUNCTIONAL COMPOSITE COMPONENT WITH POWER GENERATION, STORAGE AND STRUCTURAL CAPABILITIES</i> .....	38
4.1	INTRODUCTION .....	38
4.2	MULTIFUNCTIONAL COMPOSITE FOR SHOEs .....	38
4.3	FOOT PRESSURE DISTRIBUTION.....	39
4.4	MULTIFUNCTIONALITY.....	40
4.4.1	Piezo power generation.....	41
4.4.2	Structure – walking comfort .....	47
4.4.3	Storage .....	49
4.5	HARVESTING CIRCUIT OPTIMIZATION .....	50
5	<i>Chapter 5: PNEUMATIC TIRE-BASED PIEZOELECTRIC POWER GENERATION</i> .....	52
5.1	POWER GENERATION METHODOLOGY .....	52
5.1.1	Treadwall/Contact patch deformation .....	53
5.1.2	Sidewall deformation.....	53
5.2	TIRE PATCH CONSTRUCTION.....	54
5.2.1	Piezo element selection .....	54
5.2.2	Element layout .....	57
5.2.3	Adhesive Selection .....	59
5.3	TESTING.....	59

5.4	EXPERIMENTAL RESULTS.....	60
5.4.1	Power Output and tire contact patch length (L).....	63
5.5	ELECTRICAL CIRCUITRY.....	64
5.5.1	Power transmission from piezo patch to rim .....	64
5.5.2	Power loss in Commutator: .....	65
5.5.3	Power loss across rectifiers.....	66
5.6	IDENTIFIED METHODS OF INCREASING POWER OUTPUT.....	66
5.6.1	Piezo element density.....	66
5.6.2	Piezo stacking.....	67
5.6.3	Sidewall coverage .....	67
6	<i>Chapter 6: PIEZOELECTRIC POWER GENERATION FOR SENSOR APPLICATIONS: DESIGN OF A BATTERY-LESS WIRELESS TIRE PRESSURE SENSOR</i> .....	68
6.1	INTRODUCTION.....	68
6.2	POWER GENERATION METHODOLOGY .....	69
6.2.1	Approach I – Tire mounted PZT benders .....	69
6.2.2	Approach II – Wheel mounted PZT element.....	70
6.3	TIRE PRESSURE MONITORING SYSTEM DESIGN.....	72
6.4	RESULTS .....	75
6.5	FREQUENCY OF OPERATION .....	75
6.5.1	Elimination of Motion detection.....	76
6.5.2	Power consumption .....	77
6.5.3	TPMS Module placement options.....	78
7	<i>Chapter 7: PIEZOELECTRIC POWER GENERATION FOR SENSOR APPLICATIONS: DESIGN OF A PIEZO-POWERED WIRELESS VEHICLE SPEED SENSOR</i> .....	80
7.1	INTRODUCTION.....	80
7.2	VECHICLE SPEED SEnsing.....	80
7.3	POWER GENERATION.....	82
7.4	SYSTEM PERFORMANCE .....	84
7.4.1	Power Consumption .....	84
7.4.2	Power Reservoir – Battery .....	84
7.4.3	Battery Charging .....	85
7.4.4	Power Conservation.....	88

7.5	VEHICLE SPEED SENSOR SYSTEM .....	89
7.5.1	Sleeping.....	90
7.5.2	Wakeup circuit .....	91
7.5.3	Battery-Free operation .....	92
7.6	MULTIFUNCTIONALITY.....	92
8	<i>Chapter 8: ELECTRONICS DIFFERENTIAL FOR PHEV</i> .....	93
8.1	BACKGROUND INFORMATION.....	93
8.1.1	Differential .....	93
8.1.2	Differential for Electric Vehicles .....	94
8.1.3	Theoretical background and principal of operation .....	95
8.1.4	Simplification of the Ackermann equation .....	96
8.1.5	PID Controller.....	99
8.2	HARDWARE .....	100
8.2.1	Speed control of Motors .....	100
8.2.2	DC Motors .....	101
8.2.3	Motor Controller .....	101
8.2.4	Microcontroller .....	102
8.2.5	Driver Input Parameters .....	103
8.2.6	Feedback - RPM Measurement.....	105
8.3	RESULTS AND DISCUSSION.....	106
8.3.1	Overall Differential System .....	106
8.3.2	Steering and Calculation of Ackermann angle .....	107
8.3.3	Inner and Outer Wheel Rotational Speed Difference.....	108
8.3.4	Differential Software Logic .....	111
8.3.5	Various PID test results .....	112
8.4	FURTHER TESTING.....	114
9	9. COST .....	115
10	10. FUTURE WORK .....	116
11	11. CONCLUSION .....	117
	REFERENCES.....	118

## LIST OF FIGURES

Figure 1-1: Perovskite Crystal of a piezoelectric material above the curie point (top). Below the curie point, the crystal elongates and attains a dipole giving it the piezoelectric capability [10]. .4	
Figure 1-2: Orientation of dipoles of different domains within the element. Orientation is random in (a) resulting in zero net dipole. Dipoles are aligned resulting in a net dipole due to the application of current (b) [10].....	6
Figure 1-3: Behavior of piezoelectric element under normal condition (a), under the application of force (b and c) and under then application of voltage (d and e) [10] .....	7
Figure 1-4: Stress in piezoelectric benders [10].....	8
Figure 1-5: Piezoelectric bender elements offered by americanpiezo.com [10]. .....	9
Figure 1-6: Shear mode piezoelectric element. Different electroding and polarization patterns are shown in (a), (b1) and (b2) [13]. .....	10
Figure 1-7: Radial type piezoelectric elements [10]. .....	11
Figure 1-8: Alignment of branches in PVDF molecules [14]. .....	11
Figure 1-9: Direction of piezoelectric polarization [10]. .....	13
Figure 2-1: Capacitor charging from piezoelectric source [18].....	16
Figure 2-2: NiMH battery charging from a piezoelectric source [20]. .....	17
Figure 2-3: Front view of tire testing machine .....	18
Figure 2-4: 48V battery pack, motor controller and other electronics.....	19
Figure 2-5: Pneumatic piston used to simulate vehicle weights .....	20
Figure 2-6: Tire mounted inside out on the wheel hub .....	21
Figure 2-7: Commutator assembly.....	22
Figure 3-1: Thunder piezo bender used in shoe as an insert [18]. .....	23
Figure 3-2: PVDF composite shoe heel [22].....	24
Figure 3-3: Microstructured piezoelectric polymer shoe insert [23].....	25
Figure 3-4: Impact back energy harvested module [24].....	27
Figure 3-5: Illustration of electromagnetic coupling arrangement [25].....	28
Figure 3-6: Cross-sectional view of tire with piezoelectric element attached [26]. .....	29
Figure 3-7: Cross-sectional view of tire with cable running along the circumference [27].....	30
Figure 3-8: Voltage response of two cables as a function of speed [27].....	31
Figure 3-9: Battery powered valve-stem TPMS module [28]. .....	32
Figure 3-10: (a) Schematic of the RFID based TPMS sensor (b) placement of RFID transponder on the wheel and the receiver coil on the chassis [33]. .....	34
Figure 3-11: Piezotag - Piezoelectric harvesting unit for batteryless TPMS modules [34].....	35
Figure 3-12: Traditional Hall Effect RPM sensor [3-17] .....	36
Figure 4-1: Composite comprising of power generating and storage layers, storage medium being a Thin-film battery (top) or a capacitor (bottom) .....	39
Figure 4-2: Foot pressure distribution [22].....	40

Figure 4-3: Cantilever piezoceramic stack with foam filling the space between piezoceramic layers. (b) The bottom view of the simply supported PZT heel insert assembly. The wooden supports at either end can be seen here.....	42
Figure 4-4: Shoe with piezo stack installed. No Exterior modification was required. (b) inner rubber rib structure of the shoe which was later cut out for the in-heel insert as shown in the image (c) and (d). .....	43
Figure 4-5: Average voltage produced by the PZT stack across various resistive loads .....	44
Figure 4-6: Power delivered by the PZT stack into a 50 k $\Omega$ resistive load .....	44
Figure 4-7: Rise in voltage across of a 47 $\mu$ F capacitor with each step from the heel based piezo composite. Three trials were conducted to confirm the accuracy of results. 12.4V is accumulated after 6 steps .....	45
Figure 4-8: Side view of the foam insole with piezoceramic element (blue) neat the heel portion. ....	46
Figure 4-9: Foam insole with piezoceramic element near the heel area. (a) The thickness taper and the slanted angle of the custom made sole can be seen. (b) A commercially available foam insole with PZT bimorph placed between tapers layers.....	46
Figure 4-10: Capacitor charging from insole.....	47
Figure 4-11: Layers of the composite with PZT/brass bimorph layers bonded to epoxy structural layers.....	48
Figure 4-12: Rectification circuit fabricated directly onto the fiberglass (left), and (b) single layer of piezo stack with circuit .....	48
Figure 4-13: (a) An unsealed Thin-Film electrolytic capacitor at less than 0.05 mm thick, and (b) 0.7 mm Thin-film battery.....	49
Figure 4-14: Structure of a thin-film battery .....	50
Figure 4-15: Relative voltage gain in a 47 $\mu$ F capacitor from successive stepping.....	51
Figure 4-16: Schematic of the energy harvesting circuit .....	51
Figure 5-1: (a) Non-deformed tire at no loading and (b) Formation of contact patch due to deformation of a loaded tire (right). The reduction in sidewall height due to deformation is also visible i.e. A > B .....	52
Figure 5-2: Factory shipped PZT bender (right) compared to a penny, 25mm x 40 mm brass cut out (center) and 25mm diameter brass cut out (left) .....	56
Figure 5-3: Voltage response due single deformation from (a) full element (b) 40 x 25 mm cut out (c) 25 mm diameter cut out and (d) 40 x 25 mm upside down bonded piezo bender element .....	56
Figure 5-4: (a) PZT bender patch installed on the treadwall of the tire. (b) 2-row small patch ready to be bonded to the tire .....	57
Figure 5-5: Concave and convex deformation of piezoceramic elements .....	58
Figure 5-6: (a) Flexibility of the piezo patch. (b) Centerline bonding of the piezo element onto rubber substrate .....	59
Figure 5-7: Power and voltage across a 1 k $\Omega$ load as a function of RPM .....	61
Figure 5-8: Power vs. resistive load at 540 RPM (60km/h) and 840 RPM (100 km/h) .....	61
Figure 5-9: Demonstration of the independance of power output on tire contact patch length. 63	

Figure 5-10: (a) Inner side of the rim with wires connected to the steel electrodes. (b) Close-up of the electrode assembly with wire, bolt, steel and rubber washer visible.....	65
Figure 6-1: (a) PZT bender element of size 1" x 1.5". (b) PZT bender elements bonded to the inner treadwall of the tire.....	69
Figure 6-2: Charging of (a) 22 $\mu$ F, (b) 47 $\mu$ F, (c) 100 $\mu$ F, and (d) 150 $\mu$ F capacitor from tire bonded PZT benders at 80 RPM (~10 km/h).....	70
Figure 6-3: (a) PZT element for tire bead-rim interface (b) element placed between the rim and tire at the bead-rim interface (c) graphical representation of PZT element placement .....	71
Figure 6-4: Voltage build up in a 22 $\mu$ F capacitor from rim mounted PZT element .....	72
Figure 6-5: Schematic and circuit of the TPMS module.....	73
Figure 6-6: Voltage drop across the storage capacitor during different TPMS operation phases 1) Reading pressure from the sensor, 2) Wireless transmission of data and 3) Low power Sleep mode .....	74
Figure 6-7: Frequency of pressure reading transmission at various vehicle speeds .....	76
Figure 6-8: Discharge characteristics of various capacitors into a 4.5 mA load .....	77
Figure 6-9: (a) TPMS module built for testing and (b) receiving unit .....	79
Figure 7-1: PZT bender elements attached to the inner surface of a tire. Rectifiers can be seen above the elements .....	81
Figure 7-2: Piezo sensing circuit used for RPM measurements.....	81
Figure 7-3: Output of the sensing circuitry as read by the controller .....	82
Figure 7-4: Voltage buildup in two different capacitors from piezo charging.....	83
Figure 7-5: Power delivered to various loads by PZT harvester .....	83
Figure 7-6: PZT harvester battery charging circuit.....	85
Figure 7-7: 3.0V [11 mAh] battery discharging test.....	86
Figure 7-8: 3.0V [11 mAh] battery charging tests.....	86
Figure 7-9: Similarities between capacitor charging using PZT harvester and function generator .....	88
Figure 7-10: Vehicle speed sensor schematic.....	90
Figure 7-11: Sleeping sequence .....	91
Figure 7-12: Wakeup sequence .....	92
Figure 8-1: A Mechanical differential.....	94
Figure 8-2: Geometry of Ackermann angle during a turn. The difference of inner and outer wheel angles is noticeable.....	95
Figure 8-3: Closed loop control logic with Feedback for motor control.....	99
Figure 8-4: Affect of Proportional, Differential and Integral constants on PID controller. ....	100
Figure 8-5: Mars Electric 0708 motor. The motor has a diameter of 9 inches.....	101
Figure 8-6: Kelly KD72401 motor controller .....	102
Figure 8-7: Arduino microcontroller board.....	102
Figure 8-8: Identical electronic acceleration and brake pedals.....	103
Figure 8-9: Throttle, steering Interface with MCU .....	103
Figure 8-10: Feedback of Potentiometer mounted at the steering wheel.....	104
Figure 8-11: Hall effect RPM sensor .....	105

Figure 8-12: Output of Hall effect RPM sensor .....	106
Figure 8-13: Electronic Differential schematic.....	107
Figure 8-14: Variation in Ackermann angle with steering wheel rotation .....	108
Figure 8-15 Variation in inner and outer wheel RPM with varying speed during full turn .....	109
Figure 8-16: Distance travelled by inner and outer wheel during turns of various radii.....	110
Figure 8-17: Software side PID controller logic .....	111
Figure 8-18: PID wheel speed matching results.....	112
Figure 8-19: PID – Mixed turning results .....	113
Figure 8-20: PID - low speed differential turning.....	114

## LIST OF TABLES

Table 1-1: Comparison between PZT and PVDF .....	12
Table 5-1: Frequency of piezo bender deformation as a function of vehicle speed .....	53
Table 5-2: Required end-to-end deflection of piezo benders of different sizes.....	54
Table 5-3: Qualitative comparison of (PZT) and (PVDF) piezoelectric benders .....	55
Table 5-4: Effect of tire radius on number of piezo benders and their end-to-end deflection....	62
Table 5-5: Required RPM of various tire sizes for speeds of 60 and 100 km/h.....	63
Table 6-1: Time for which a 4.5mA load can be supported by various capacitances.....	75
Table 7-1: Capacitor charging frequencies .....	88
Table 8-1: Variation in inner and outer wheel angle with Ackermann.....	98
Table 8-2: Sample RPM values for 100 km/h.....	98
Table 8-3: Variation in Ackermann angle with steering angle.....	109

## NOMENCLATURE

AC	- Alternating current	$R_o$	- Outer radius
C	- Capacitor	RPM	- Rotation per minute
CC	- Constant Current	RX	- Receiver
CV	- Constant Voltage	SM	- Smart Material
<i>CV</i>	- Continuously Variable	t	- Time (S)
d	- Piezoelectric Voltage Constant	TPMS	- Tire Pressure Monitoring
DC	- Direct Current	System	
g	- Charge Constant	TX	- Transmitter
I	- Current	V	- Velocity
$I_a$	- Armature current	V	- Voltage
L	- Length	VSS	- Vehicle Speed Sensor
Li-Ion	- Lithium Ion	$\delta$	- Ackerman angle
MCU	- Microcontroller	$\delta_{in}$	- Angle of inner tire
NiMH	- Nickel Metal Hydride	$\delta_{out}$	- Angle of outer tire
PVDF	- Polyvinlydiene Floride	$\Phi$	- Flux
PZT	- Lead Zirconate Titanate	$\omega_{in}$	- Angular speed inner wheel
$R_I$	- Inner radius	$\omega_{out}$	- Angular speed outer wheel

## *Chapter 1: BACKGROUND INFORMATION*

### **1.1 INTRODUCTION**

The design and development of everyday use products nowadays has been strongly influenced by the need for a positive corporate market image to be achieved through a green initiative that has given rise to the current trends that emphasize the exploitation of alternative energy sources while reducing energy consumption and the usage of fewer material resources whenever possible. Two distinct approaches are being used in this regard: 1) improving the energy efficiency of existing systems through weight reduction, and 2) introducing cleaner technology that relies on renewable sources of energy rather than nonrenewable and limited sources. Although the first approach is effective, the energy and material savings achieved through it are limited. It involves the replacement of traditional materials with lighter alternatives that provide the same functionality without compromise in the quality [1]. The second approach however replaces conventional power sources such as batteries and the electrical grid with built-in power harvesting units comprising of either some kind of a mechanical generator or the more common piezoelectric vibration energy harvesting units [2-4]. These harvesters make use of readily available waste mechanical energy such as vibrations, impacts, deformations etc., and transform it into usable electrical energy with a satisfactory level of efficiency. Depending upon the magnitude of the mechanical disturbance and the properties of the harvester itself, adequate energy can be recovered to power small sensors for remote sensing. Various sensor applications of piezoelectric harvesters have been developed including temperature, pressure, gas sensors etc. However, their practical implementation has been mainly limited to industrial applications and no such application has surfaced for use within the automotive industry. With the paradigm shift towards more efficient and lighter vehicles, use of such sensors that do not require any external power source are regarded as becoming a norm in the near future.

Besides the obvious energy benefits, there are two prime reasons for using power harvesting for sensors: (i) powering remote sensors located in hard to reach locations that are not only mission critical but difficult to power with a hard wire and (ii) when a battery is not sufficient to power the sensor for long periods of time without requiring a replacement and a more stable power source is required. Tire pressure sensors that are mounted within the tire represent prime examples of such sensors. Replacing the battery with a power harvester in such sensors not only provides for a longer sensor life but also results in a much simpler system as power conservation strategies become unneeded [4].

## 1.2 MULTIFUNCTIONAL MATERIALS

A new class of materials known as Multifunctional Materials aims to combine multiple functionalities into an identical material component in order to achieve weight savings [5]. Multi-functional materials systems are composite material systems capable of performing multiple "primary" functions simultaneously or sequentially in time, and have been specifically developed to improve system performance by reducing the redundancy between sub-system materials and functions. One of the functions of these composites is always structurally related while others typically include sensing, power storage, and/or actuation. Examples include reinforcement materials for concrete and other structural elements [6].

Multifunctional smart materials are typically available in either of the following formats:

- (i) Layered structure: Layers of different materials are stacked and bonded together. Addition of electrically conductive layers in between structural layers of various materials is a common practice in multifunctional materials [7].
- (ii) Composite, with fibers/particles held in a matrix: The most common example is the addition of carbon black or carbon fibers to make the material electrically and/or thermally conductive [6].
- (iii) The combination of the two.

The American Army has developed many systems that incorporate power storage in the form of thin-film batteries and fuel Cells directly into the structural layers. These multifunctional composites provide direct weight and space savings

through the reduction of components [8]. Fuel savings are also realized as a result of weight reduction [1].

### 1.3 SMART MATERIALS

Smart materials are a special class of materials that exhibit some sort of feedback or a change in response to environmental stimuli such as temperature, pressure, electric current and magnetic fields [9]. Though every material reacts in some way in response to changing environmental conditions such as elongation of metal due to temperature rise, change in conductivity etc, these reactions are very limited in terms of their usability and occur at a much smaller scale compared to the responses of Smart Materials to suitable stimuli. Moreover, the range of responses offered by Smart Materials is much wider (generation of voltage, sudden changes in viscosity, change in color etc) compared to those offered by conventional material, which are limited to temperature based elongation, conductivity changes and changes in viscosity relative to applied pressure. For example, where a regular material may just deform under an applied load, piezoelectric materials generate a voltage. Such materials are of great use with a much wider and innovative application potential in comparison to conventional materials [9].

#### 1.3.1 *Classification of Smart Materials*

Smart materials are typically categorized as follows [9]:

- 1) Piezoelectric – capable of change in geometry upon the application of electric field and vice versa
- 2) Shape memory Polymers and Alloys – have ability to remember the original shape even after deformation due to applied stress loading. The original shape is usually restored through heating or cooling beyond a certain point.
- 3) Magnetic Shape Memory – change geometry upon exposure to a magnetic field. The effect is reversed by application of an opposite magnetic field.

- 4) pH-sensitive fluids – change volume due to the changes in the pH of their surroundings. Change is sustained until the pH is reversed back to the original state.
- 5) Ferrofluids – demonstrate polarization in the presence of magnetic field
- 6) Photomechanical materials – change shape upon exposure to light
- 7) Magnetorheological fluids – fluids that experience a change in viscosity in the presence of a magnetic field. The change in viscosity is directly proportional to the strength of the field.
- 8) Chromogenic systems – undergo change in color upon the application of electricity or a change in temperature.

## 1.4 PIEZOELECTRIC MATERIALS

Piezoelectric materials undergo a change in shape upon the application of an electric potential and vice versa [10]. They are typically 30-75% efficient in converting one form of energy into another and have a variety of applications in areas including power generators, sensors, actuators and transducers.

The piezoelectric was first discovered in 1880 by Jacques and Pierre Curie while experimenting with certain crystalline minerals. They discovered that the crystals produced an electric current when subject to tensile and compressive forces. They also elongated and shortened when exposed to electric fields of opposite polarities [10]. The primary piezoelectric materials in use today are Lead Zirconate Titanate (PZT), Lead Titanate ( $\text{PbTiO}_3$ ), Barium Titanate ( $\text{BaTiO}_3$ ), Polyvinylidene Flouride (PVDF) and composites

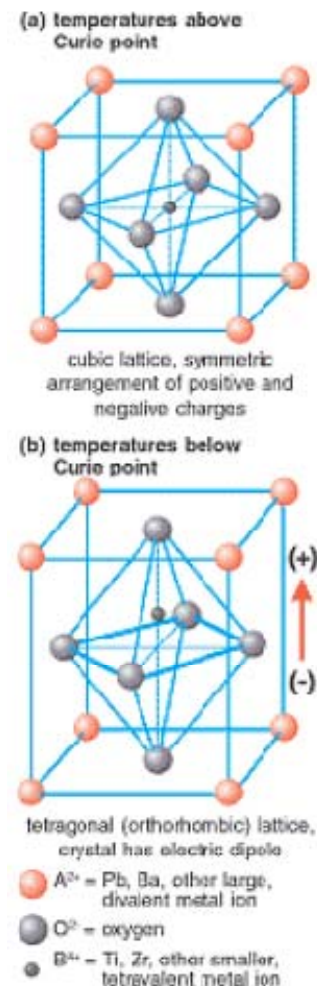


Figure 1-1: Perovskite Crystal of a piezoelectric material above the curie point (top). Below the curie point, the crystal elongates and attains a dipole giving it the piezoelectric capability [10].

of PZT and PVDF [11]. Out of these, PZT are the most commonly used and manufactured piezoelectric materials and will be the center of discussion in the report.

#### ***1.4.1 Synthesis of Lead Zirconate Titanate (PZT) Piezoelectric materials.***

Powder of three constituents Lead, Zirconate and Titanate are mixed in proportionate quantities and heated to form the compound. A binder is added to the powdered compound to ease the shaping process, which is achieved by die-pressing into desired shapes including rods, plates, discs, rings, blocks. The shaped elements are heated to between 600-700 °C for a couple of hours to burn off the binder. Then the temperature is raised to around 1300 °C to sinter the particles into a consolidated solid [10].

#### ***1.4.2 Origin of Piezoelectricity***

When the powdered mixture is heated, the particles sinter and form a dense crystalline structure. A critical temperature point called the Curie point exists above which each crystal exhibits a simple cubic geometry as presented in Figure 1-1. However, as the temperature drops the crystal structures changes to assume a tetragonal or rhombohedral symmetry and attains a dipole moment. Since different crystals are oriented in different directions, the individual dipoles cancel each other out i.e. zero net polarization results. Figure 1-2 shows the arrangement of dipoles in domains and their net effect [10]. To achieve piezoelectric effect, the dipoles need to be aligned to result in a net dipole. This is accomplished by applying a high potential difference across the piezoceramic element in the desired direction, a process known as ‘poling’ [11]. The magnitude of potential difference depends upon the chemistry; for PZT the typical poling voltage is about 2 kV/mm [12]. Figure 1-2 (a) shows the randomly organized dipoles while Figure 1-2(b) demonstrates the alignment of individual dipoles under the application of poling voltage. After the poling voltage is removed, the dipoles begin to revert back to some degree of randomness due to hysteresis as depicted in Figure 1-2 (c). However, there still exists a net dipole and the ceramic retains the piezoelectric effect [10].

Piezoelectric ceramics are only usable below the temperature maximum known as the Curie point. As discussed above, the crystal structure changes to simple cubic beyond

this temperature point effectively depoling the ceramic permanently. Besides temperature limit, the strain applied to the piezoelectric ceramic has upper limits. Beyond this limit, either the brittle ceramic breaks or depoling occurs even in the absence of mechanical defects.

Current research in *piezoelectric* materials is focused in two prime areas [10]:

**Single crystal:** PMN-PT (Lead Magnesium Niobate / Lead titanate) based composites are capable of handling ten times the strain compared to polycrystalline lead Zirconate Titanate.

**Relaxors:** in these materials, the transition from *piezoelectric* to non-piezoelectricity takes place over a range of temperatures instead of a single Curie point.

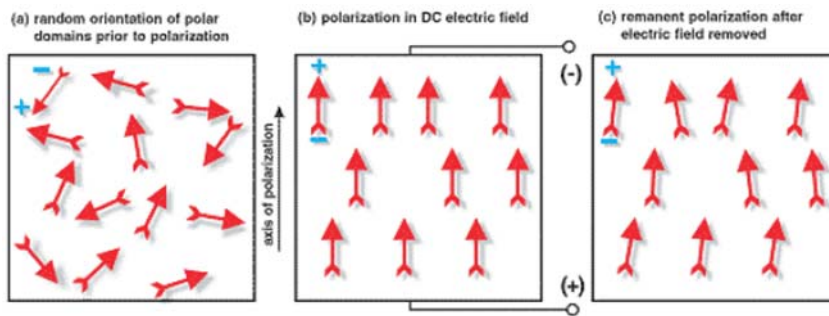


Figure 1-2: Orientation of dipoles of different domains within the element. Orientation is random in (a) resulting in zero net dipole. Dipoles are aligned resulting in a net dipole due to the application of current (b) [10]

Figure 1-3 shows the correlation between applied potential difference and the direction of shape change and vice versa. When the voltage is applied in the same direction as the dipole of the element, elongation occurs and vice versa. In case of applied stress, compression generates a voltage whose polarity is same as the dipole.

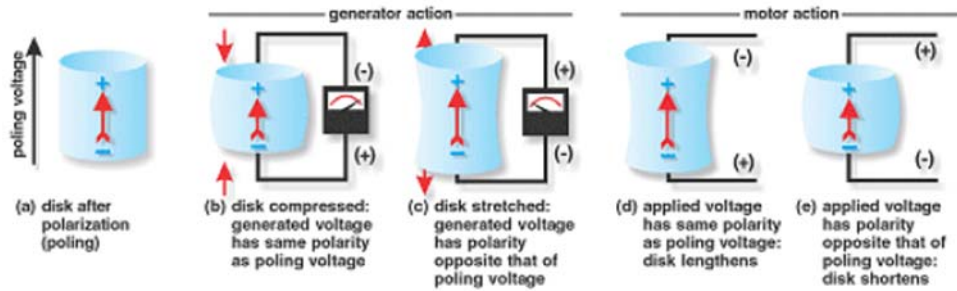


Figure 1-3: Behavior of piezoelectric element under normal condition (a), under the application of force (b and c) and under then application of voltage (d and e) [10]

#### 1.4.3 PZT Element types – polarization

This classification of piezoelectric ceramics (PZT) is based on the direction of polarization voltage and the nature of shape change with applied electric field after polarization. There are three main types:

##### 1) Tension/Compression

These include PZT element shaped into discs, rings, plates and blocks with the polarization voltage applied to opposite faces. The application of electric field produces a strain along the same direction as that of polarization i.e. that is elongation or shrinkage occurs in the direction of the net dipole due to electric field applied parallel to it. Figure 1-3 shows the relation between polarization, applied electric field and the resultant shape change [12].

For power generation, such elements are used either in compression or tension mode. In reverse mode, when a tensile strain is applied to the element the resulting voltage generated within the ceramic has the opposite polarity than the net dipole.

**Application:** these types of PZT elements are used in a variety of applications including igniters, ultrasonic vibrators, actuators, microphone transducers, and power harvesting where impacts are involved.

## 2) Bending mode

Piezoelectric ceramics, piezoceramic for short, used in bending mode are prepared in the same manner as the Tension/Compression mode elements. However, not all shapes can be or are used in bending mode; only discs and plates are used because of ease of bending due to low thickness. Furthermore, these regular ceramics cannot directly be employed in bending mode due to two reasons, 1) the ceramic by itself is too brittle and will break when subjected to a bending moment, and 2) the line of zero moment (the center of inertia) lies along the geometric center of the element with tension on side and equal and opposite compression on the other as shown in Figure 1-4(a). The voltage produced by the half under tension is negated by that produced by the half in compression thus zero output voltage results. To solve these two obstacles, the ceramic element is usually bonded to a metallic plate usually brass or silver. The metallic plate distributes the strain evenly across itself and the ceramic preventing stress concentration and damage to the ceramic thus increasing the maximum allowed deflection. Moreover, the plate shifts the line of zero bending moment from the element to itself resulting in either pure tension or compression within the ceramic and providing a net voltage output. Figure 1-4 (b) shows the shift in the line of zero moment away from the center. In this case, the metallic plate is attached at the top and the line of zero moment lies at the interface between the plate and the ceramic.

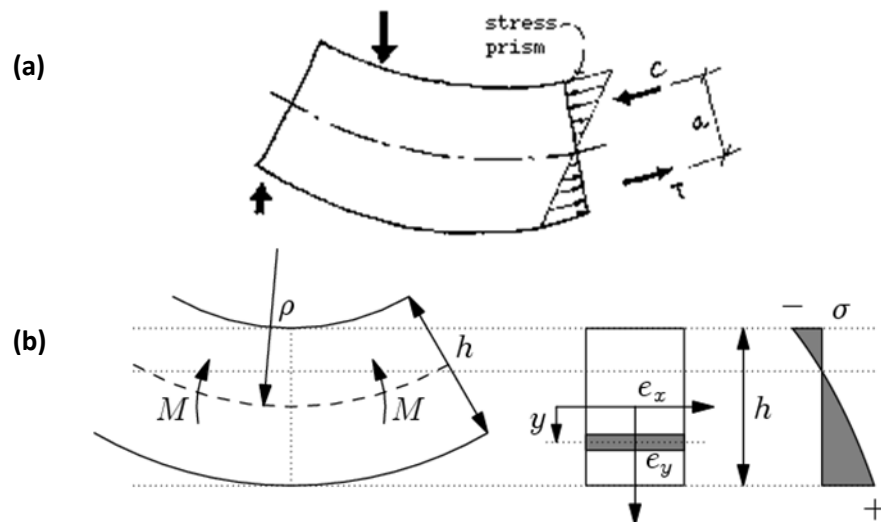


Figure 1-4: Stress in piezoelectric benders [10].

Figure 1-5 below shows PZT bender elements offered by piezo.com [4].

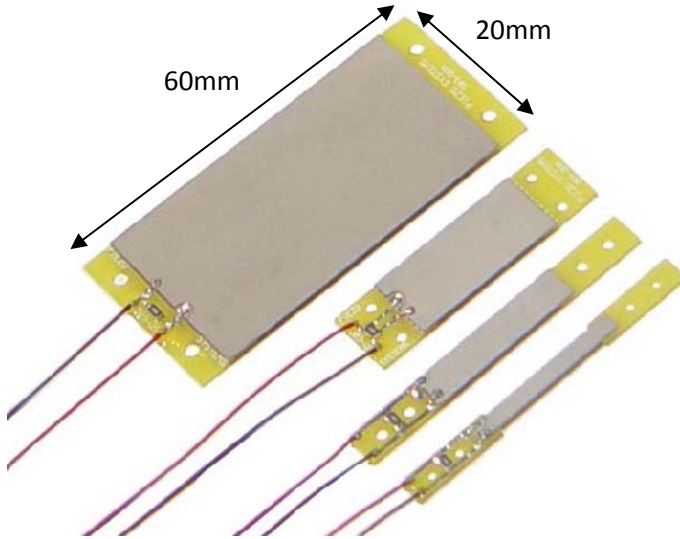


Figure 1-5: Piezoelectric bender elements offered by americanpiezo.com [10].

Most popular applications of piezoelectric benders include vibration energy harvesting, piezoelectric speakers, buzzers, and actuators etc.

### 3) Shear mode

Unlike tension/compression mode where the poling voltage is applied on opposite faces, shear mode element are poled along the surface parallel to the direction of the required shear strain. The Positive “+” and Ground connections are attached to the same surface either at opposite ends or the positive being in the center with ground connection near the two ends as depicted in Figure 1-6 [13]. The electrons flow from the center positive electrode attached to the ceramic to the two ground electrodes on either side. Figure 1-6 (b1) shows the regions are polarized as the result marked with ‘P’ and those that remain unaffected marked with “NP”. These regions fail to polarize because the electrons flee the ceramic to the metalized electrode due to lower resistance to flow offered by the latter. The electrodes may applied on the single side if the element is thin enough or both sides for relatively thicker electrodes as shown in Figure 1-6 (b2). The flow of electrons ‘hugs’ the surface of the ceramic rather than penetrating into its depth which makes it difficult to pole thicker elements

[13]. Moreover, use of three electrodes i.e. one positive and two negative reduce the distance to be travelled by the electrons into half thus effectively reducing the required polarization electric field into half as well. For example, poling a 20mm disc or plate element would require an electric field of 40 kV if only two electrodes are used; positive at one end and the ground at the other. Using three electrode configuration as in Figure 1-6 would require only 20 kV for the same element size.

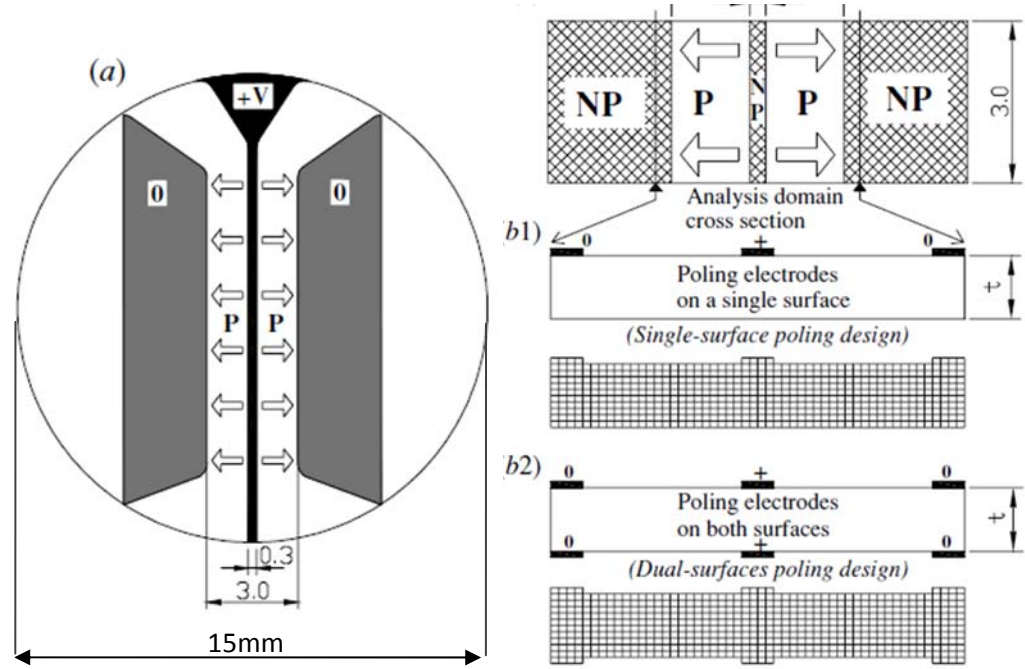


Figure 1-6: Shear mode piezoelectric element. Different electroding and polarization patterns are shown in (a), (b1) and (b2) [13].

#### 4) Radial mode

These are cylindrical tubes of piezoceramic elements with one electrode on the inner side of the tube and the other on the outer side. Thus the dipoles either emanate away from the center or towards it. The application of electric field results in the increase or decrease of the radius/diameter of the tube depending upon its alignment to the net dipole. Figure 1-7 shows a PZT tube with the direction of poling and elongation marked with arrows [10].

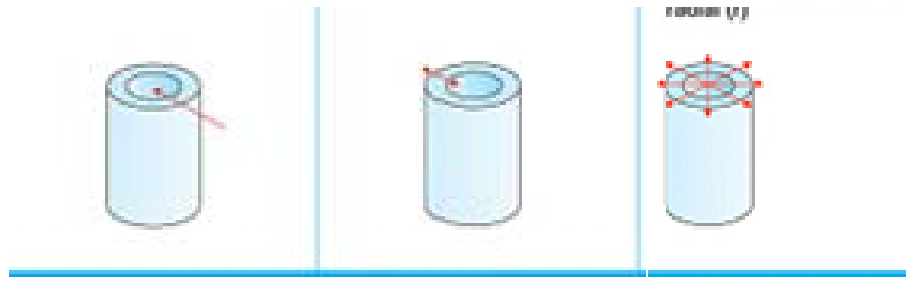


Figure 1-7: Radial type piezoelectric elements [10].

## 1.5 POLYVINYLIDENE FLORIDE (PVDF)

PVDF is the only polymer that exhibits strong and stable piezoelectric properties. It is a semicrystalline (55% crystalline) polymer of  $\text{CH}_2\text{-CF}_2$  monomer [14]. The positive hydrogen on one side of neutral carbon and negative fluorine on the other side result in a polar molecule. Five (5) distinct crystalline phases have been identified in PVDF polymers namely:  $\alpha$ ,  $\beta$ ,  $\gamma$ ,  $\delta$ , and  $\epsilon$  with a net dipole occurring only in the last four phases. The orientation of chains in  $\alpha$  phase is such that the poles are antiparallel resulting in zero net dipole as shown in Figure 1-8. Of the 4 crystalline phases,  $\beta$  has been identified as the phase of stable and permanent dipole and is of utmost important in PVDF polymers from the point of view of piezoelectricity. The dipoles and molecules in all the polar phases are perpendicular to the chain [14]. This is the why PVDF sheets are often stretched before poling to straighten out the chains and align the molecules relatively along the same axis. Poling is usually performed on the stretched PVDF at temperature of 80 – 100 ‘C to reduce poling time and to achieve higher remnant polarization [15].

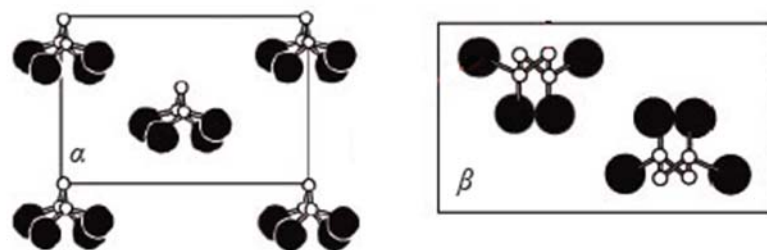


Figure 1-8: Alignment of branches in PVDF molecules [14].

## 1.6 COMPARISON BETWEEN PVDF AND PZT

Table 1-1 below presents a summarized comparison between PZT and PVDF piezoelectric materials based on a few common and very important factors to be considered before selecting between the two for specific applications. For applications point of view,  $d_{33}$ ,  $g_{33}$ , temperature and flexibility are major contributors. While PZT offers higher  $g_{33}$  coefficients, PVDF have much higher  $d_{33}$  coefficient. Though, the usable temperature range of PVDF much narrower than PZT, the former can still be used in a wide variety of applications especially those where room and regular atmospheric temperatures are encountered. The charge constant and voltage constant values of PVDF and PZT were taken from [16] while the temperature was taken from [17].

Table 1-1: Comparison between PZT and PVDF

	<b>PZT</b>	<b>PVDF</b>
<b>Charge constant (<math>g_{31}</math>)</b>	$110 \text{ pcN}^{-1}$	$18-20 \text{ pcN}^{-1}$
<b>Voltage Constant (<math>d_{31}</math>)</b>	10	216
<b>Poling Voltage</b>	20 kV/mm	50 kV/mm
<b>Depoling Temperature</b>	150 °C	90 °C
<b>Melting Temperature</b>	1600 °C	170 °C
<b>Flexibility</b>	Low (brittle)	Very High (ductile)
<b>Modes of Vibration</b>	Tension	Tension, Compression, Radial, Shear etc.

## 1.7 SOME PIEZOELECTRIC CONSTANTS

Piezoelectric ceramics and polymers are anisotropic which is why the direction of polarization and applied force/voltage affects the response of the element and is of great importance. As shown in Figure 1-9, direction 3 is assigned to the direction of polarization. Direction 1 is used for any force applied perpendicular to the direction of polarization while direction 2 is used for elements in shear mode [10][11].

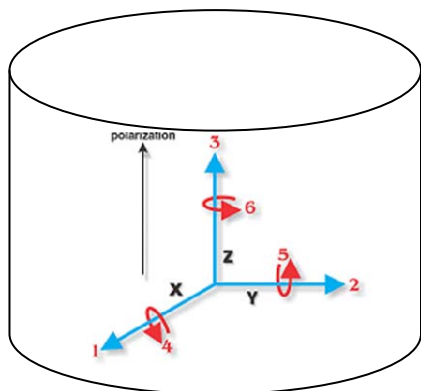


Figure 1-9: Direction of piezoelectric polarization [10].

When specifying piezoelectric constants, two subscripts are used to identify the relation between applied force/voltage with the direction of polarization. When the direction of applied force is along the axis of polarization a subscript ‘33’ is used, whereas ‘31’ is used when the applied force is perpendicular to the polar axis [10]. All the following definitions and formulas have been taken from the ‘American Piezo’ website [10]

### **1. Piezoelectric Voltage Constant (g)**

Electric field generated by the piezoelectric element as a result of an applied force and vice versa.  $g_{33}$  is used for a force parallel to the direction of polarization and  $g_{31}$  is used to characterize a force perpendicular to the polar axis.

### **2. Piezo electric Charge Constant (d)**

Polarization generated upon the application of stress.

### **3. Frequency Constants**

A piezoelectric element being vibrated at a particular high frequency value where the radial mode resonance frequency ( $N_p$ ) is at the same as the series resonance frequency ( $f_s$ ). for circular elements, the three resonance frequencies namely radial ( $N_p$ ), axial ( $N_T$ ) and longitudinal ( $N_L$ ) mode resonant frequency constant are related to three geometrical dimensions of diameter (D), thickness (h), and length (L) respectively as :

$$N_p = f_s D \quad \dots(1-1)$$

$$N_T = f_s h \quad \dots(1-2)$$

$$N_L = f_s L \quad \dots(1-3)$$

#### **4. Elastic Compliance ( $s$ )**

Is the measure of flexibility of the piezoelectric element. It is the reciprocal of the Young's Modulus of the material

$$s = 1/Y \quad \dots(1-4)$$

#### **5. Electromechanical Coupling Factor ( $k$ )**

It describes the efficiency of the piezoelectric material in converting mechanical energy input to electric energy output

$$k = \frac{\text{electrical energy output}}{\text{mechanical energy input}} \quad \dots(1-5)$$

### **1.8 APPROXIMATION OF PIEZOELECTRIC BEHAVIOUR**

Based on the above constants, the charge and Electric field generated from a specific piezoelectric element can be approximated from the following set of equations:

$$E = -g_{33}T \quad \dots(1-6)$$

$$T = F/A \quad \dots(1-7)$$

$$Q = -d_{33}F \quad \dots(1-8)$$

where  $E$ : electric field (V)

$T$ : stress on ceramic element (Pa)

$Q$ : generated charge (C)

$F$ : force (N)

$A$ : surface area on which  $F$  is applied ( $m^2$ )

## *Chapter 2: TESTING AND EXPERIMENTATION SETUP*

### **2.1 CONDITIONING AND STORAGE OF HARVESTED POWER**

The charge generated by piezoelectric materials is an alternating current (AC) sine waveform. In all cases, the harvested power needs to be stored before it is regulated and used in end application. Two different power storage components are used depending upon the length of time for which the charge needs to be held, namely: Capacitor and Battery. The former is mostly used for temporary or short term storage of power due to higher leakage currents. Batteries are used for long term power storage or in application where power generation using piezoelectric materials is unpredictable or occurs at irregular interval and thus a more stable and reliable power source is required.

Typical capacitor values used in most piezoelectric energy harvesting applications range between  $22 \mu\text{F}$  to  $100 \mu\text{F}$ . Power produced by piezoelectric harvesters is only limited to a few micro or at the most milliwatts because of which the voltage rise across the capacitor requires some time.

### **2.2 CAPACITOR CHARGING**

The capacitor charging circuit is shown in Figure 2-1. The output from the piezo element is rectified and fed to the capacitor for storage. The size of the capacitor as well as the level of charge generated by the piezo element determines how fast the capacitor reaches a certain threshold. The capacitor should be sized appropriately according to the maximum voltage generated by the piezoelectric element [18][19].

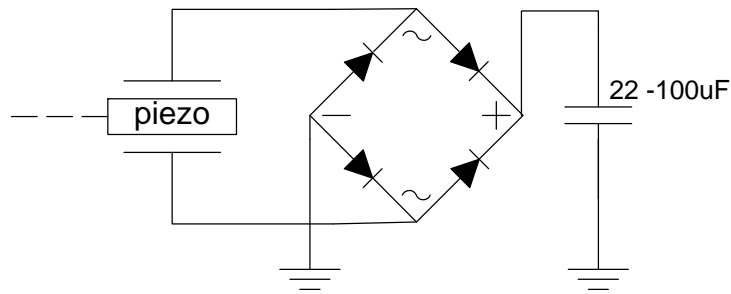


Figure 2-1: Capacitor charging from piezoelectric source [18].

## 2.3 BATTERY CHARGING

Since capacitors can hold very small charge compared to the batteries the device being supplied often only operates intermittently depending upon the rate of capacitor charging. On the other hand, due to the high charge capacity of batteries they can support the device for longer periods of time but also require long time duration for recharging by a piezoelectric harvester. The nature of the device dictates the type of energy storage to be utilized. In any case, the power harvested from piezoelectric sources must be more than the power required by the device to allow sustainable operation.

### 2.3.1 *Nickel Metal Hydride (NiMH) Battery*

NiMH batteries have a cell voltage of 1.2V and offer medium energy density of 140-300 W-h/L. these batteries can be charged between 500-1000 times depending upon discharge characteristics including rate of discharge, depth of discharging and rate of charge. NiMH batteries are very attractive for charging from a piezoelectric source because of the simplicity of the circuit required for charging. As shows in Figure 2-2, only an additional zener diode is required between the temporary storage capacitor and the battery [20]. The zener diode acts as a voltage reference for constant voltage (CV) charging of the battery.

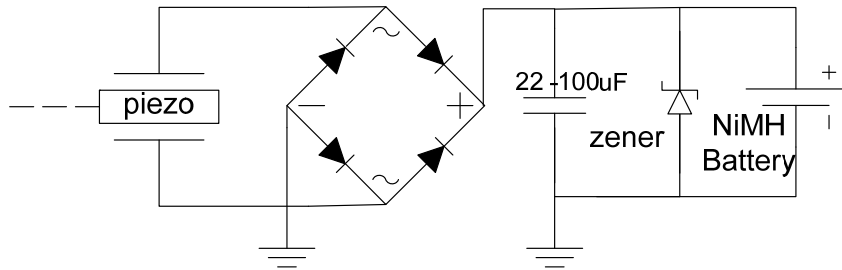


Figure 2-2: NiMH battery charging from a piezoelectric source [20].

One of the main disadvantages of NiMH batteries is their limited operating temperature range of -20 to 60 °C, outside which the charge capacity as well as the discharge rate are adversely affected. Their usually high self-discharge rates also make them undesirable candidates in applications with large time intervals between successive recharging.

### 2.3.2 *Lithium-Ion (Li-Ion) Battery*

Compared to NiMH, Li-Ion batteries offer a higher cell voltage of 3V, more charging cycles (usually 1000 times rechargeable), greater energy density of 370 W-h/L and lower self discharge rate. However, the main disadvantage is the use of specialized CV and constant current (CC) circuitry required for controlled recharging. Many Li-Ion battery management ICs are available that can be utilized. However, since the voltage curve for a piezoelectric source is parabolic rather than a near constant voltage straight line, the charge management IC must have a broad voltage range. Moreover, such ICs including microchip's MCP73811/2, Linear Technologies's LT®1512, Semtech's SC806 and Texas Instrument's BQ2401 require supply currents between 1.5 – 5 mA, which are very high to be supported by low power piezoelectric sources and thus unusable. Even with lower power ICs that require between .8 – 1.5 mA supply current, the power delivered to the battery to actually recharge it is very low leading to a highly inefficient battery recharging circuit. Such high current requirements of Li-Ion battery management ICs makes the use of Li-Ion batteries very complicated and challenging [21].

## 2.4 TESTING EQUIPMENT - DYNAMOMETER

A small scale tire testing dynamometer was developed to test and measure the power generation in tires from the piezoelectric bender elements. To simulate the formation of tire contact patch due to vehicle weight on the road, the tire is spun on a conveyer belt assembly. The conveyer belt is driven by two 6 inch pulleys, one of which is connected to a 48V DC motor. A 200 Amp motor controller along with an RPM sensor enables the control of tire rotational speed allowing the simulation of different vehicle velocities. A hub assembly connects the wheel to a vertical slider assembly that is driven by a pneumatic piston. The piston presses the wheel assembly against the belt simulating vehicle weight creating a tire contact patch on the belt. The pressure in the piston can be adjusted to simulate different vehicle weights generating contact patches of different sizes. Camber and toe are inherently kept constant for design simplification.

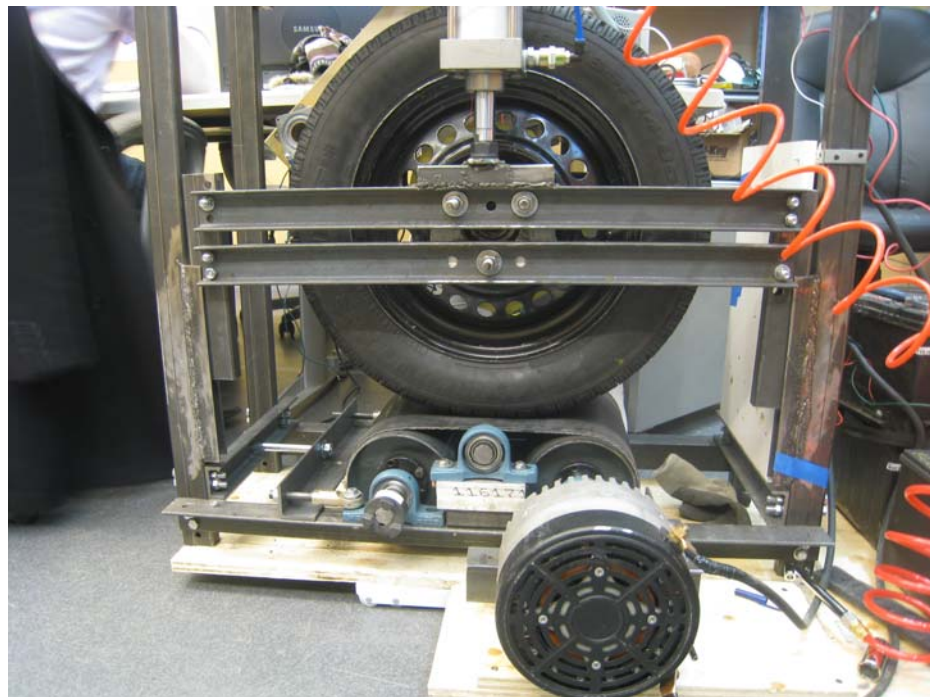


Figure 2-3: Front view of tire testing machine

Figure 2-3 shows the front view of the tire testing machine with the tire sitting on the conveyer belt. The DC motor connected to the pulley is also visible. The DC motor is driven by a 48V battery pack made up of four (4) 12V automotive batteries connected in series as shown in Figure 2-4. The batteries and the DC motor are interconnected through

a DC motor controller that allows speed control either using a 0-5k $\Omega$  potentiometer or a 0-5V throttle input. The throttle input can also be replaced with a signal from a microcontroller allowing precise control of motor speed. The 6kW motor has a maximum loaded RPM of 3200. Since the apparent gear ratio between the 6" pulley and the 24" tire is 1:4, this gives a maximum tire RPM of 800 or roughly 90 km/h. However, due to limited battery life and lack of thermal management of motor as well as the battery pack, the motor can only be driven at full speed for a few minutes. Moreover, since the tire dynamometer was designed to be movable rather than anchored to the floor, high speed operation causes considerable vibration of the entire structure and is unsafe of the laboratory environment. Thus the dynamometer is only used for low speed testing ensuring a safe working environment for other users of the laboratory.

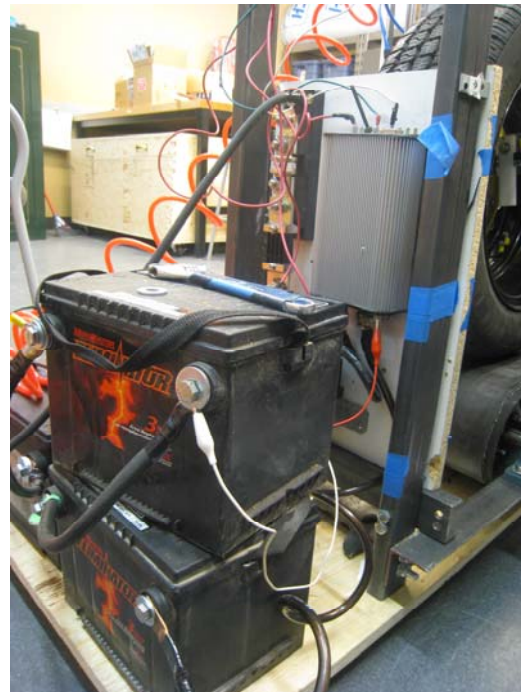


Figure 2-4: 48V battery pack, motor controller and other electronics

The pneumatic piston that is used to create a contact patch by pressing the wheel assembly against the conveyer belt is bolted onto the vertical sliding assembly. This arrangement allows the sliding assembly and thus the wheel attached to it to be lowered as well as raised. The piston is supplied by a 120 psi air compressor as shown in Figure 2-5 via a 3-position 5-way pneumatic switch, which allows the piston to be extended,

retracted or maintained at a particular position. By adjusting the pressure on the compressor and selecting the direction of the pneumatic switch, the tire can be lowered or raised. In the raised position, the tire can be changed, serviced and worked on with relative ease.



Figure 2-5: Pneumatic piston used to simulate vehicle weights

Vehicles make use of a Continuously Variable (CV) shaft to connect the hub assembly of the wheel to the chassis, however to keep the design of the dynamometer simple the CV shaft was omitted. Instead of an adjustable CV shaft, a solid ‘arm’ was used to connect the hub assembly to the vertical sliding assembly as can be seen in Figure 2-3. Due to the length of the arm, the applied simulated weight via the pneumatic piston would result in a negative chamber on the tire reducing the contact patch area along the width of the tire. To avoid this problem, the tire was attached to the hub with the inside out as shown in Figure 2-6.



Figure 2-6: Tire mounted inside out on the wheel hub

The conveyer belt is responsible for two main tasks, 1) creation of contact patch to simulate the road effect, and 2) transmission of torque from the driven pulley to the wheel in order to spin in - both of these roles are affected by the tension in the conveyer belt. For this reason, the tension of the conveyer belt needs to be adjustable and is achieved by the use of a tightening screw. The screw allows the distance between the two pulleys to be increased or decreased effecting the tension in the belt proportionally. Moreover, when the tire spins on the belt it applies a lateral force on the belt forcing it to slide off the pulleys and rub against the bearings and other structural components causing it to wear and increasing the rotational load. Two adjustment screws are used on either side of the pulley to apply a counter lateral force on the belt preventing it from sliding and reducing damage.

Since the piezoelectric elements generate power only due to deformation, the air pressure in the tire or the weight on the tire do not affect the power output. The only variable is the tire contact patch length and width.

## 2.5 COMMUTATOR ASSEMBLY

A DC motor style commutator was designed for the extraction of power from the continuously rotating wheel for measurement purposes. It consists of a thin fibreglass composite board with two circular copper rings, one connected to the positive and the other to the ground coming from the tire. The board is bolted to the rim using hub wheel threads and thus rotates with it. The stationary brush assembly consists of two carbon brushes bonded to the ends of electrically isolated steel screws. The screws pass through holes in the vertically oriented plastic plate and are pushed out by springs as shown in Figure 2-7. Nuts attached to the screw on the opposite side of the plastic plate prevent the screws from sliding out completely. As the wheel rotates, power is transferred from the copper rings to the carbon brushes rubbing against them and is extracted through wires connected to the screw. The height of the brush assembly, angle and its distance from the wheel can be adjusted by 3 different screws, one of which can be seen in Figure 2-7 attached to the vertical plastic. The entire commutator assembly has a low resistance of  $0.7\Omega$  for each of the two connections for a total series resistance of  $1.4\Omega$ .

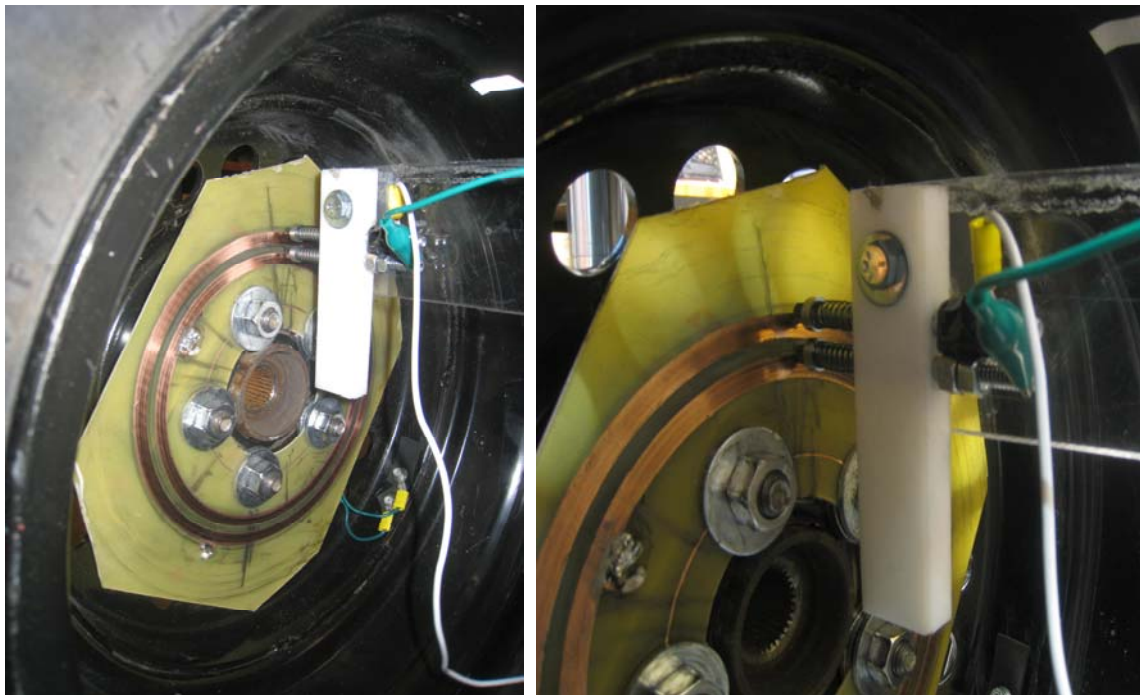


Figure 2-7: Commutator assembly

## *Chapter 3: LITERATURE SURVEY*

### **3.1 PIEZOELECTRIC POWER HARVESTING SHOES**

#### ***3.1.1 Power generating Insole Insert***

Kymmissis et al. [18] developed a dual approach piezoelectric power harvesting insole insert based on a PZT bender that sits under the heel to harvest strike energy upon stepping and a PVDF composite stack that rests under the front half of the foot to harvest power from the bending of the sole. A commercially available Thunder PZT unimorph, shown in Figure 3-1, which was developed in cooperation with NASA is used for the heel based harvester. The bender is designed to be curved in relaxed mode and flat when force (stress) is applied on it. It measures 5 x 5 cm and rises 2.5 mm in relaxed mode. Since the bender cannot be reverse bent, a solid metallic plate is placed under it to prevent damage during stepping.

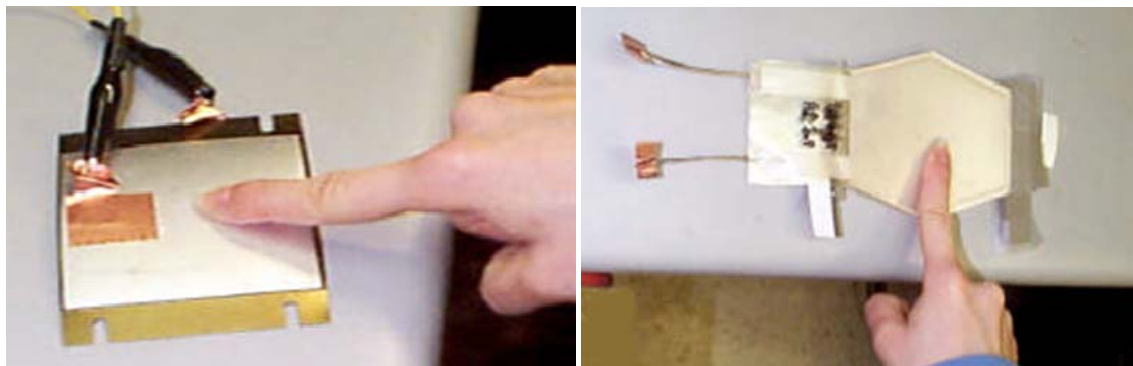


Figure 3-1: Thunder piezo bender used in shoe as an insert [18].

The second approach makes use of a 16 layer PVDF stacked shown in Figure 3-1 above. It consists of 8 layers of PVDF bonded to each other on either side of a thin brass plate. As the sole bends during walking, the PVDF stack bends with it producing a charge. In essence both harvesters rely purely on the bending mode for power generation. However, PVDF being inherently flexible does not require a solid support underneath it unlike the PZT bender but produces much less charge comparatively.

Using this combination Kymmissis et al. are able to generate 8.4 mW of average power which was used to run a shoe mounted RFID tag intermittently [19].

### 3.1.2 PVDF shoe-heel insert

D. Fourie [22] reinvents the shoe by replacing a conventional shoe-heel with his own PVDF composite structure as shown in Figure 3-2. It consists of 52  $\mu\text{m}$  thick PVDF unimorphs bonded to 4 mil thick PET sheets. The sheets are placed between equally spaced polycarbonate plates. When the weight of the body acts upon this structure, it causes the polycarbonate plates to deform which in turn bend the PET sheets and the PVDF unimorph attached to them thus generating power. Polycarbonate and PET sheets provide sufficient flexibility required for bending as well as the rebound necessary to restore the PVDF unimorphs to relaxed state without structural degradation. The entire structure is placed within a rubber sole cut out removed from an actual shoe. Figure 3-2 shows the composite heel installed in a test shoe with the rectifier and capacitor attached on the outside.

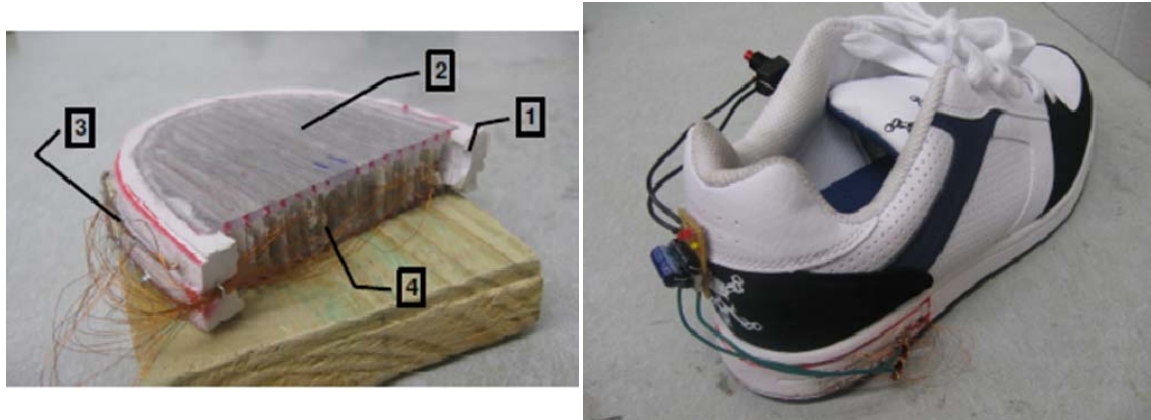


Figure 3-2: PVDF composite shoe heel [22].

This arrangement of PVDF unimorphs generates a mere 0.06 mW of maximum power and requires significant modifications to the shoe heel design.

### 3.1.3 Microstructured polymer shoe-heel insert

Kaajakari et al. Made use of a 80  $\mu\text{m}$  thick microstructured piezoelectric polymer film for power generation within the shoe heel. A 2 cm wide strip of this polymer is metalized on both sides and then wrapped around itself 60 times for a cylindrical thickness of 1 cm. The roll is placed within the shoe heel cavity for power generation from the striking of the shoe at each step. The polymer has microcells which result in a low young's modulus of 3-6 MPa and matches the elastic properties of regular shoe fillings. Figure 3-3 shows the microcell structure of the polymer as well as the polymer wrap that replaces the regular shock absorber installed in the shoe.

4.0 mW of power is generated from this arrangement. Author(s) also claim this polymer harvester to be very light weight, elastic and low cost [23].

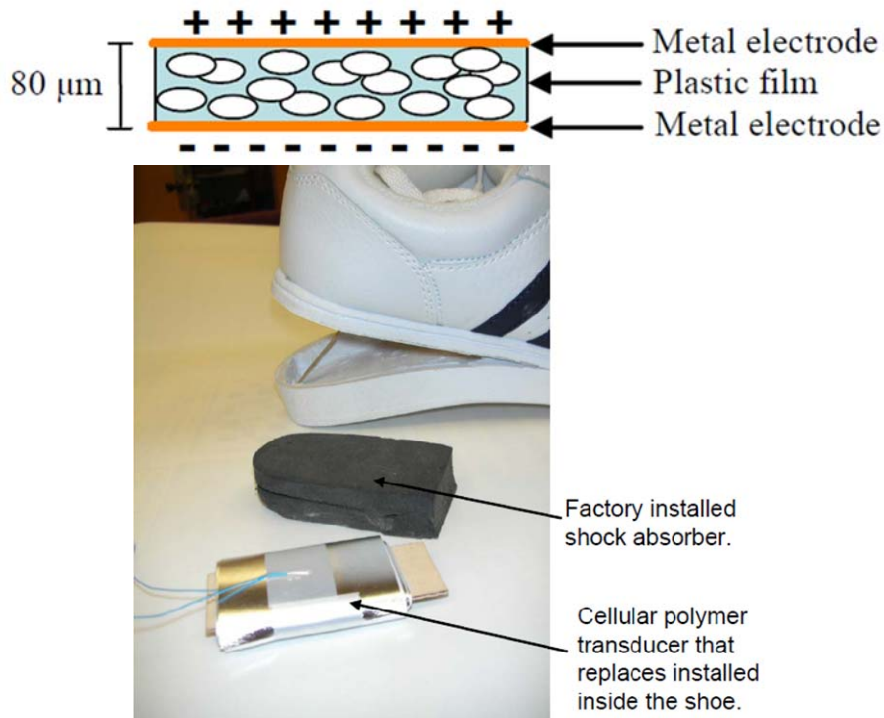


Figure 3-3: Microstructured piezoelectric polymer shoe insert [23].

### **3.2 POWER GENERATION IN TIRES**

Use of various sensors embedded within the wheel assembly has promoted the idea of being able to generate power within the wheel instead of relying on limited batteries. Running power cables from chassis to the wheel mounted sensor presents a great deal of challenge as the electrical contacts need to be maintained during wheel rotation excluding them from the list of possible power sources. Being able to generate power within the wheel has the obvious advantage of unlimited sensor life rather than relying on the limited battery. Moreover, methodologies required for the conservation of energy to provide a longer sensor life which are otherwise necessary may also be omitted. A lot of work has been done on developing various methods and techniques to harvest power from within the wheel assembly using mechanical magnet-coil assemblies to vibrating masses as well as piezoelectric bender harvester. However, the goal has always been to generate power only sufficient to run sensors while harvesting large amounts of power to be able to run onboard devices or recharge battery has yet to be realized. A few of the small scale power generation methods are discussed below.

#### ***3.2.1 PZT Impact Energy Harvesting***

This approach uses centripetal force developed during wheel rotation to generate an impact on the Thunder piezoelectric generator. Figure 3-4 shows the assembly of the impact generator that is mounted onto the vehicle rim. It consists of a piezoelectric generator mounted at one end of the housing, which is large enough allow a metallic ball to move inside it. When the wheel rotates, centripetal force, gravitational force and tangential force acts on the ball causing it to move from one end of the housing to another. When the ball moves towards the side with the piezoelectric generator, energy is produced due to impact. Noteworthy is the fact that the Thunder piezoelectric transducer utilized here is actually a unimorph bender that is curved in relaxed state. When the ball bearing strikes this bender, it flattens it out producing a charge. Thus the impacting force is not a factor in the magnitude of power produced as long as it is sufficient to fully flatten out the bender i.e. bender only produced charge due to deformation and not due to the actual impact [24].

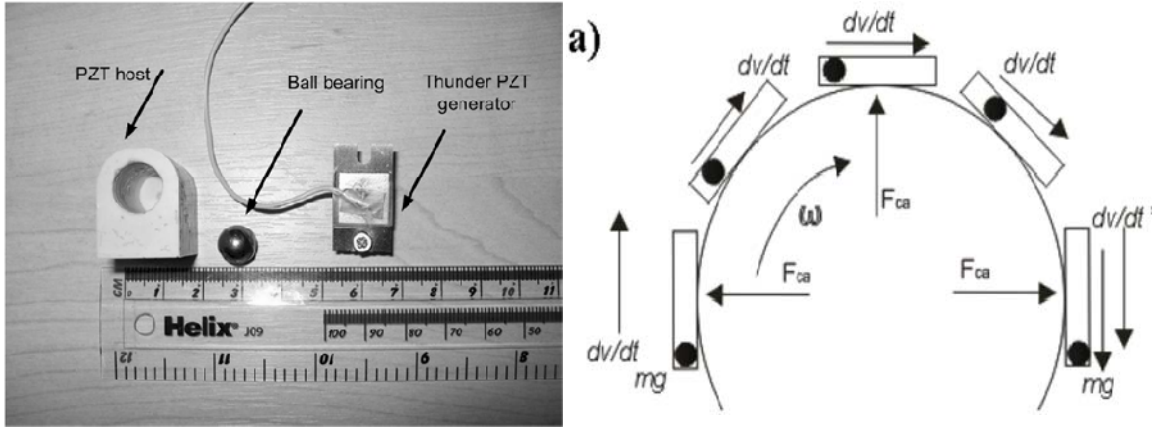


Figure 3-4: Impact back energy harvested module [24].

Using the above depicted configuration, a generator with a volume of  $2 \text{ cm}^3$  produced 4 mW of power when mounted on a 0.12m diameter wheel spun at 800 rpm.

### 3.2.2 *Electromagnetic Power Generation in wheels*

Alessandro Volpi presents an electromagnetic approach to generate power in the wheel assembly. He makes use of the ferrous steel wires in the bead of the tire as the core around which conductive wires are wound in a coil, making the modified tire bead the secondary side of the magnetic generator. The primary side comprises of a permanent magnet affixed to the chassis in close proximity to the bead. As the tire rotates, the changing magnetic field across the coil induces a current in it that can be accumulated in a capacitor for powering small sensors. This arrangement only produces power when the wheel is rotating. If the permanent magnet is replaced with an electromagnet, the transfer of power from the chassis to tire rather than production of power in the tire occurs, which can be sustained even when the tire is stationary. Such an arrangement is similar to a low efficiency transformer [25].

Figure 3-5 presents a hand sketched rendition of setup described above. Permanent magnetic (38) with coil wound around it (39) are attached to the chassis and remain

stationary relative to the hub, while the coil wound around the steel wires within the wheel (22 and 26) move relative to the fixed electromagnet as the wheel rotates.

If an electromagnet is used instead of a permanent magnet, then the approach simply reduces to a power transfer rather than power production and must be supplied by onboard batteries or other suitable power source. Since only AC currents work with electromagnets, a DC primary power source must be inverted into an AC signal before being supplied to the electromagnetic.

Figure 3-5 shows a side view of the entire arrangement. The other circular coil is part of the tire bead while the two electromagnetics on the side are supplied by onboard power sources. It should be noted that such an approach is only possible with a non-ferrous rim such as an aluminum alloy rim since ferrous rims would concentrate the electromagnetic fields within preventing any fields from ever reaching the bead integrated coil.

The power recovered in the tire is directly proportional to the power supplied in the primary side and inversely proportional to the losses of transmission [25].

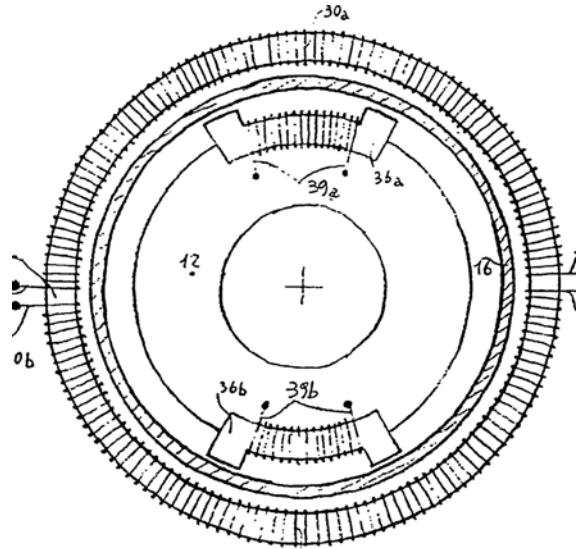
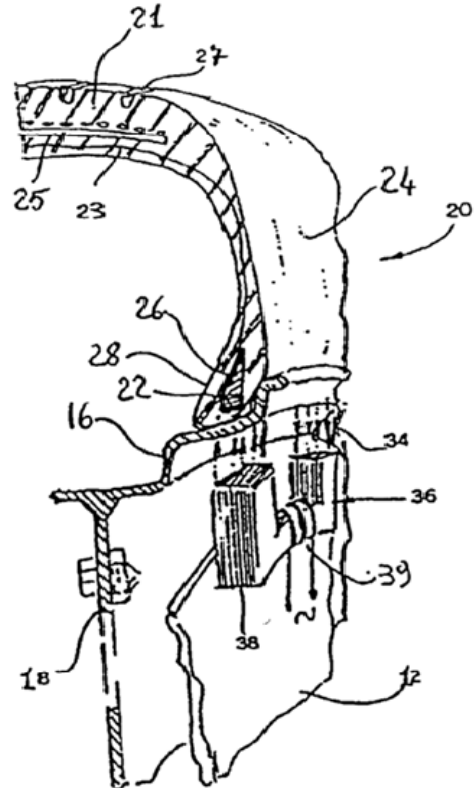


Figure 3-5: Illustration of electromagnetic coupling arrangement [25].

### 3.2.3 Piezoelectric Power Generation in wheels

This patent describes use of a piezoelectric structure bonded to the tire to generate electricity using the mechanical energy of the tire flexure. The power generated can be utilized to run small sensors such as the tire pressure sensor etc. Figure 3-6 shows the piezoelectric structure (14) bonded to the tire with the sensor module (12) attached on top of it [26].

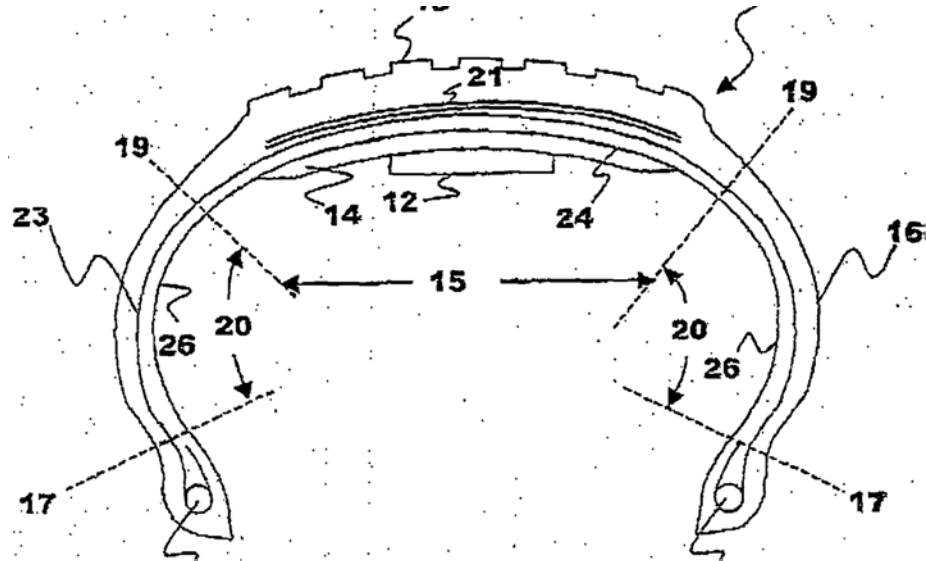


Figure 3-6: Cross-sectional view of tire with piezoelectric element attached [26].

The strain required to flex the piezoelectric element is supplied by deformation of the tire as it rotates, flattening out at the road contact. The charge produced by the generator is then stored in a capacitor, regulated and then used to power the electronics of the sensor in question.

The power generated by the piezoelectric element and its details, type and cost as well as the power required by the sensor etc. have not been specified. Moreover, it is unknown whether power generated exceeds the power requirement of the sensor or does the charge need to be accumulated over time through successive rotations of the tire. The patent does specify the tire crown (inner side opposing the treads) as the idea place to mount a piezoelectric harvester [26].

Another patent describes a similar approach but using a specific piezoelectric bender actuator known as the Multiple Fiber Composite (MFC) supplied by Smart Materials Corp. It consists of multiple  $\mu\text{m}$  diameter piezoceramic (PZT) fibers arrangement together in an epoxy matrix. This patent does include a method for regulating the power to be supplied to further electronic circuits including a microcontroller or a battery charger.

### **3.2.4 System for generating power inside the tire using piezoelectric cable**

Even though the idea is similar to previous methods using piezoelectric element to generate power, the type of transducer utilized for power generation is entirely different i.e. a piezoelectric cable bonded to the inner surface of the tire along the circumference. Figure 3-7 shows the crosssection of the tire with the cable (9) attached to it [27].

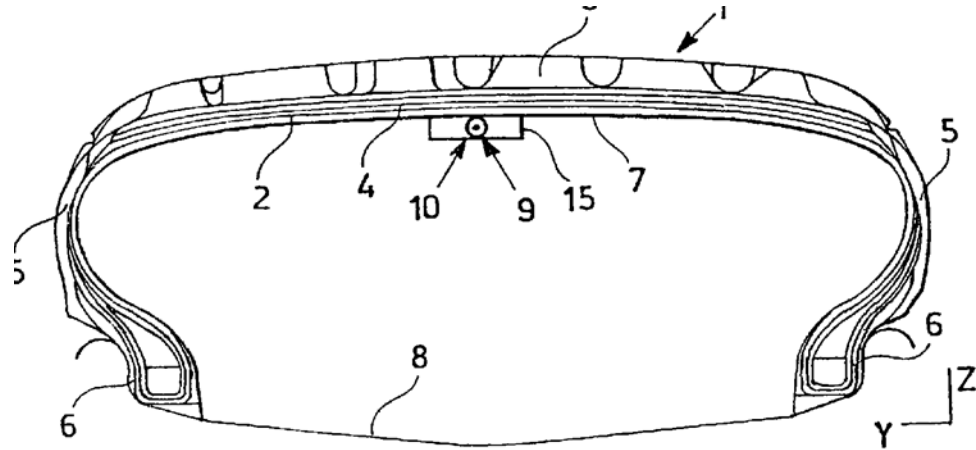


Figure 3-7: Cross-sectional view of tire with cable running along the circumference [27].

As the tire rotates, a section of the continuous cable flattens out with the tire at the road contact and generates power. Compared to other piezoelectric elements, the cable generates a very low voltage upon deformation as shown in Figure 3-8. This is due to the PVDF inner core as the power generating material as compared to piezoceramics used in

previous designed presented in this report. The voltage increases with the increasing vehicle velocity due to more deformations of the cable per second.

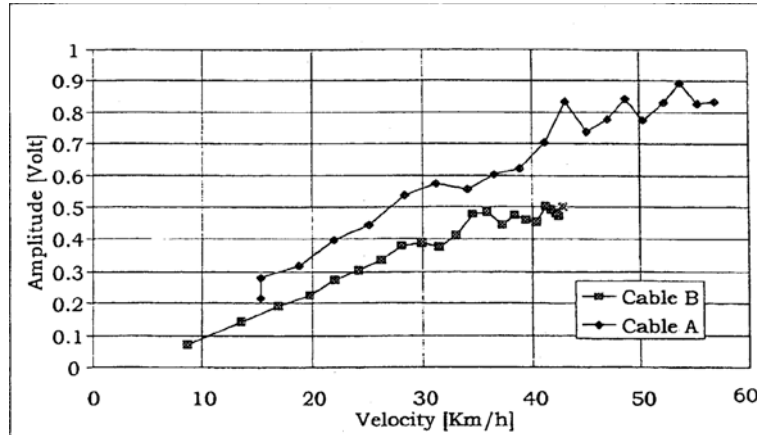


Figure 3-8: Voltage response of two cables as a function of speed [27].

Two different cables are tried and tested and the results are presented in Figure 3-8 above. This voltage is after rectification loses which typically range between 0.7 to 1.4V [27].

### 3.3 TIRE PRESSURE MONITORING SYSTEM (TPMS) SENSORS:

In recent years, monitoring of tire pressure has become important for two prime reasons: 1) Safety and 2) reduction of CO<sub>2</sub> emissions due to higher gas consumption caused by underinflated tires [28]. Some 250,000 accidents are reportedly caused by inappropriate tire pressure in the US every year [29]. Improved handling and braking distance are also attributed to proper air pressure inside the tire [28]. Thus the need for continuous monitoring of air pressure inside the tire is evident.

The predominant TPMS sensors used in most commercial vehicles are those incorporated into the valve stem as shown in Figure 3-9. These modules are powered by lithium coin cell battery(s) thus resulting in a finite life span. Since a lone module life, typically 10 years, is desired battery power management, conservation and consumption efficiency are of utmost important requiring complex overall system, use of highly efficient

components, and motion detection circuitry. The latter is used to reduce power consumption by disabling the module's controller and transmission components during vehicle idling periods when transmission of pressure data is not required.



Figure 3-9: Battery powered valve-stem TPMS module [28].

Battery powered TPMS modules have a built in wakeup timer that is used to power on the microcontroller (MCU) intermittently. The MCU reads the pressure data from the sensor, encodes and transmits it to the onboard receiver then goes back to sleep until the timer wakes up the system once again. This results in a fixed transmission frequency predetermined by the manufacturer. In summary, battery powered TPMS modules suffer from four major disadvantages: 1) Limited battery life, 2) Need of motion detection resulting in a complex system, 3) Use of highly efficient components to conserve battery power, and 4) Fixed low transmission frequency [30].

A few batteryless TPMS module alternatives exists that aim to overcome one or more of the above mentioned disadvantages of the battery power modules. Most of these include wireless energy transfer from the chassis to the module mounted inside the tire. Piezoelectric energy harvesting has also been realized but only energy harvesting modules have been developed that either harvest vibration energy or the bending of the tire surface during rotation, discussed in greater detail next.

### **3.3.1 Batteryless TPMS based on contactless energy transfer:**

This technology replaces battery with continuous wireless power transfer from the onboard transmitter to the receiver on the TPMS module mounted inside the wheel. An Inductor-Capacitor-Resistor (LCR) circuit is used to achieve wireless power transfer at a frequency determined by the inductance, L, and capacitance, C, as:

$$f = \frac{1}{2\pi\sqrt{CL}} \quad \dots(3.1)$$

By having a matching L-C pair at both the transmitting and receiving ends, a radio-frequency channel is created which is normally used for data transfer. However, the same concept is also applied to wireless power transfer by rectifying the incoming signal and charging a capacitor with it at the receiving end. The TPMS module works by draining the capacitor using power regulation circuitry, thus eliminating the battery from the circuit. Thomas et al. [31] used a 2.4 GHz microwave signal for power transfer using a similar method. The length of the transmission part determines the efficiency with which power is transferred requiring the transmitter to be mounted in close proximity to the wheel, usually within a few centimeters. As the distance between the transmitter and receiver increases, the transmission losses increase until no power reaches the receiver. Because of this, the power transfer is not continuous during tire rotation but only intermittent i.e. the transfer occurs when the transmitter and receiver are closest to each during the rotation and diminishes as the tire rotates increasing the distance between the two. Thus power is transferred for only a fraction of the tire rotation resulting in high losses during the remainder interval [32].

### **3.3.2 Batteryless TPMS based on Radio Frequency Identification (RFID) technology**

This technology is similar to wireless power transfer and utilizes a passive RFID transponder embedded within the wheel with pressure sensor, controller and transmitter.

During tire rotation, the transponder gets coupled with the receiver coil and the transfer of power to the transponder and data to the receiver occurs eliminating the need of a battery [33]. Figure 3-10 (a) shows the schematic of the RFID TPMS system. The reader side consists of a microcontroller to interpret the data received from the transponder as well as a Class-E power amplifier to supply power to the transponder. The transponder consists of a RF power rectifier, a pressure sensor and a microcontroller.

The prime disadvantage of this approach is the need of a separate antenna for power transfer both inside the tire and on the chassis. Moreover, the antenna distance is critical for power transfer and needs to be tightly controlled. The size and shape of the antenna also influences the performance and efficiency of power transfer and thus are important factors to consider. Since power needs to be supplied to the reader mounted very close to the wheel, additional wiring needs to be run from the battery to each of the wheel to run the TPMS transponder making the system only partially wireless [33].

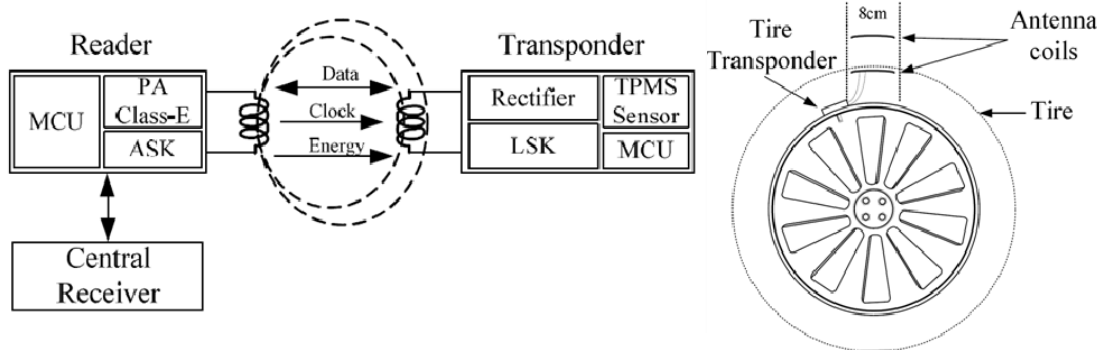


Figure 3-10: (a) Schematic of the RFID based TPMS sensor (b) placement of RFID transponder on the wheel and the receiver coil on the chassis [33].

### 3.3.3 Batteryless TPMS based on Piezoelectric harvesting

Replacement of a permanent and limited power reservoir i.e. a battery with power harvesting using piezoelectric materials has also been tested by various researchers and manufacturers. Piezotag limited [34] manufactures a piezoelectric module that is mounted on the inner surface of the tire as shown in Figure 3-11. During tire rotation, the module is deformed causing the piezoceramic (PZT) element within to bend generating

charge. Thus the piezoceramic element is used in bending mode. The charge is accumulated, regulated and used to power the electronics for TPMS operation. Siemens has also announced the development of a piezo powered TPMS module which will be commercially available by the end of 2011 [34].



Figure 3-11: Piezotag - Piezoelectric harvesting unit for batteryless TPMS modules [34].

### 3.4 VEHICLE SPEED SENSOR

There are three main types of speed sensors employed in a commercial vehicle, 1) Engine speed sensor, 2) Transmission speed sensor, and 3) Wheel speed sensor. As part of this thesis, only wheel speed sensors will be discussed. As obvious, they are used to detect the speed of each individual wheel for use in Automatic Braking System (ABS), Traction Control System (TCS) and Electronic Stability Control (ESC) [35]. The type of sensors used in vehicles for this purpose are known as Active wheel-speed sensors. They consist of a magnetoresistive IC that changes resistance with changing magnetic field. The ICs are mounted in close proximity to a multipole ring with alternating north and south poles as shown in Figure 3-12. The ring is attached to the wheel spindle and spins as the vehicle moves producing alternating magnetic flux fields at the IC. The electronics within IC produce a square pulse for each change in the magnetic field. Speed of rotation (RPM) is calculated from the frequency of these pulses [35].

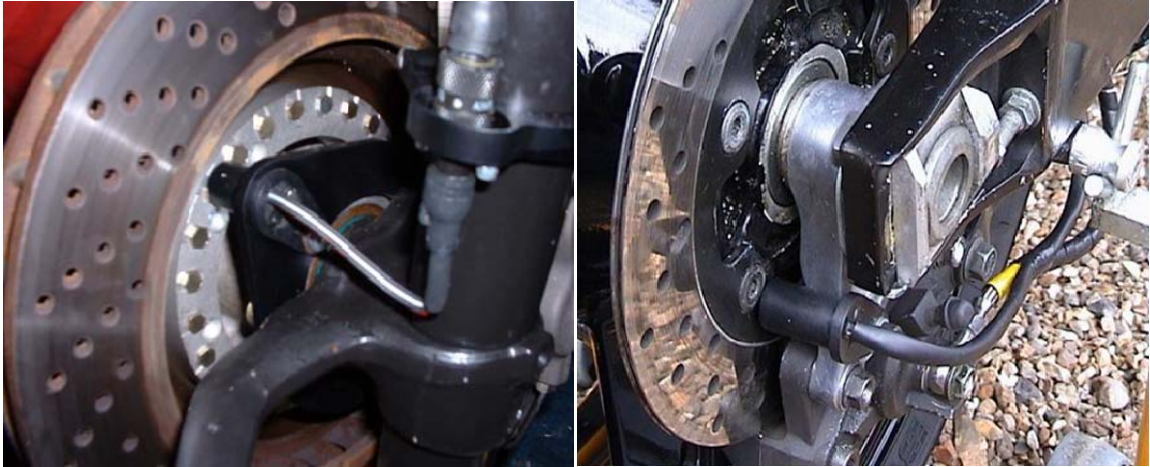


Figure 3-12: Traditional Hall Effect RPM sensor [3-17]

The main disadvantage of this approach is the need to run wires from the central processing unit of the vehicle to each of the four wheels adding to the overall weight and complexity of the system. A better approach that does not require power and wires to be run from the central unit to each wheel is needed.

### 3.5 SCOPE OF WORK

The research presented in this thesis focuses on the techniques of energy harvesting from mobile components such as shoes and pneumatic tires using their inherent motion in order to recover part of the waste energy. The design and integration of a composite with energy harvesting, storage and structural functionality is discussed for shoe applications. Such composites could be used to power GPS and RFID sensors or simply to recharge personal electronic gadgets such as a cell phone or an mp3 player. Power generation techniques for automotive applications have also been presented with a potential of powering onboard electronics or sensors embedded within the wheel. For the purpose of measuring the power output from PZT elements mounted within the wheel a dynamometer has been designed to simulate a tire contact patch eliminating the need of a test vehicle.

The subsequent part of the thesis focuses on the application of the energy harvested from the tire for powering TMPS and VSS. Replacing batteries and other permanent power sources with energy harvesting sources requires significant changes in the methodology of operation of the sensors since enough power needs to be accumulated in the temporary storage capacitor before it can be used, resulting in a intermittent operation of most sensors. Since TPMS need only work intermittently to read the pressure within the tire and transmit it, it can be run from a capacitor alone. A VSS on the other hand needs to operate continuously and must include a permanent and stable power source such as a battery, in which case the energy harvested from PZT sources may be used for recharging the battery. The design and operation of both these sensors is presented in great detail and their advantages over pre-existing battery powered designs are discussed.

The final part of this thesis deals with the design of an Electronic Differential system for the Plug-In Hybrid Electric Dune Buggy at UOIT which was built as a result of previous research. Since the buggy makes use of two electric motors (each mounted on each of the rear driving wheels) and thereby omits any transmission or a mechanical differential. Thus the differential has to be substituted with electronics which can achieve the same effect by differentiating the speed of the two motors. Various components required for the electronic differential are discussed and the experimental results from trials conducted by operating the Dune Buggy are presented to show the effectiveness of the current system.

## *Chapter 4: SHOE-BASED MULTIFUNCTIONAL COMPOSITE COMPONENT WITH POWER GENERATION, STORAGE AND STRUCTURAL CAPABILITIES*

### **4.1 INTRODUCTION**

A low cost multifunctional composite component is designed that is integrated into a shoe heel that generates 10 milliwatts of power through piezoceramic (PZT) stacks and stores this energy in a capacitor integrated within the composite. Thinfilm batteries are used as an alternative power storage method and are also integrated into the composite. PZT bimorph elements are stacked in a cantilever manner with space in-between and around elements filled with foam, which provides structural support as well as walking comfort. An insole composite with PZT layer is also developed that is capable of producing 2.2 milliwatts of power to give a total power output of 12.2 milliwatts for the in-heel insole combination. Use of PZT bimorph elements ( $d_{33} = 110$ ) instead of commonly used PVDF sheets ( $d_{33} = 20$ ) increases the power generation potential over five folds, which is further compounded by stacking of PZT elements.

### **4.2 MULTIFUNCTIONAL COMPOSITE FOR SHOES**

Shoe-based energy harvesters have focused primarily on charge production without taking walking comfort into consideration. Kymisis [18], Kaajakari [19], and Fouri [23] have developed piezo harvesting shoes using their own approaches but the focus has only been power generation using an insert. As with ordinary shoes, the in-sole is expected to provide cushioning and comfort, which requires the power harvesting unit to be added to the shoe as a separate component rather than seemlessly integrating it into the design of the shoe. Moreover, the storage of harvested energy is regarded as a totally separate function and thus assinged to a separate component. The objective of this research was to develop a layered composite that would not only generate power but also provide walking comfort by absorbing some of the pressure energy generated during walking and then store the harvested energy within itself. As a result, two multifunctional composites have been developed, one of which is integrated into the shoe-heel while other in the

insole. Furthermore, two different modes of energy storage have been explored: capacitative storage and a thin-film battery. Due to the difficulty associated with the fabrication of a thinfilm battery in-house, it has been purchased from existing manufacturers for demonstration in the proof-of-concept prototype. Figure 4-1 demonstrates the two composites, one with capacitor and the other with integrated thin-film battery. Layers of PZT stack are simply combined with power storage layers to achieve a simple-to-assemble composite.

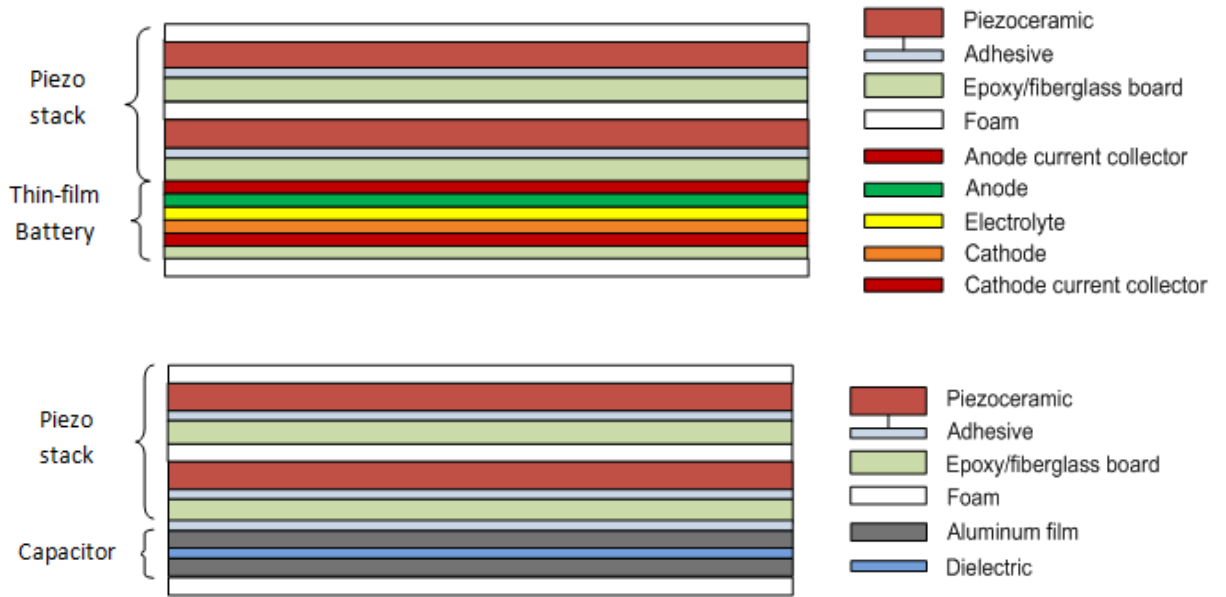


Figure 4-1: Composite comprising of power generating and storage layers, storage medium being a Thin-film battery (top) or a capacitor (bottom)

### 4.3 FOOT PRESSURE DISTRIBUTION

Before any practical power harvesting device could be fabricated it is vital to understand the kinetics associated with human movements such as walking and running with emphasis on the pressure distribution in the sole. According to Hessert [22], the weight of the body gets distributed unevenly across the foot sole during regular activities such as walking, running and standing. The pressure distribution for an average young adult is shown in Figure 4-2. The high pressure region at the heel is noticeable as well as the fact that the pressure is maximum at the center of the heel ball and minimal near the edges. A

simply supported PZT structure with one end free to slide can be placed under the heel to harvest power from the pressure energy exerted during stepping, which will bend the PZT elements. With the center of the structure aligned with that of the heel, it would experience bending defomration all across the length except for its ends. This is vital from the point of view of comfort since feeling the rigidity of the fixed end would be an unpleasant experience defying the objective of the research; multifunctionality with includes walking comfort.

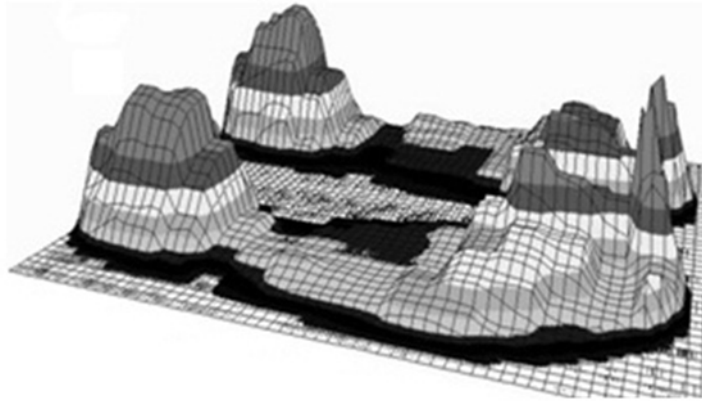


Figure 4-2: Foot pressure distribution [22].

The PZT bending structure as described above is capable of generating electrical energy due to periodic bending and rebounding of the PZT element during walking i.e. upon stepping, the piezo element would bend and relax as the foot is lifted.

#### 4.4 MULTIFUNCTIONALITY

Multifunctionality is achieved either by combining materials that perform different functions into a composite or by using materials that perform more than one function simultaneously, with the latter being multifunctional in the true sense of the word. The aim was to utilized individual material layers in such a manner whereby they would perform more than one function resulting in a compact system which can be easily scaled up to be used in other applications as well. The three (3) primary functions 1) power generation 2) power storage, and 3) walking comfort as well as secondary functions 1)

incorporation of power conditioning circuitry into the structure, and 2) elimination of separate cushioning components such as insoles, foams and compressible structures were to be achieved. These five (5) independent functions have been achieved by three distinct materials namely 1) piezoceramic, 2) epoxy fiberglass board, and 3) liquid spray foam which surrounds the entire assembly.

#### ***4.4.1 Piezo power generation***

While the primary focus is on the development of a multifunctional composite, adequate power generation still remains a priority for the composite to have any actual attractive value. With the simply supported PZT bending structure described in the previous section established as the mode of power generation, a stack needed to be developed that would generate power sufficient for charging a  $47 \mu\text{F} - 150 \mu\text{F}$  capacitor within a few steps. The voltage accumulated in the capacitor can then be regulated using a dc-dc buck/boost converter and used to power sensors, GPS locators, wireless transmitters or even recharging an ipod.

The type of PZT element being used is called a ‘bimorph’ because of its ability to bend in both directions and produce power. It consists of a thin brass plate with PZT material on either side. The two PZT discs are connected in parallel by design simply because one disc experiences compression while the other undergoes tension.

##### ***4.4.1.1 Heel integrated composite***

Shoe-heel presents itself as an ideal candidate for the integration of multifunctional composite for two reasons 1) it being a high pressure region during walking and running, and 2) the ample space available within the heel. A fact worth mentioning here is that most heels today are designed hollow from within to reduce the weight of the shoe, which means that minimal modification in the shoe design is required for the integration of the multifunctional power harvesting composite.

Figure 4-3 (a) shows a cantilever made of piezoceramic stack with space between the layers filled with foam. The foam along with elastic behavior of piezoceramic elements

attached to brass plates provide the cushioning action. The stack is attached to the base inclined at an angle to allow maximum deflection. The total height of the stack is over 1 cm and has a square footprint of 44 x 44 mm. The space underneath the stack is also filled with foam (not shown in the picture) to provide additional cushioning. Two of these stacks can be placed opposite to each other to harvest maximum energy.

Figure 4-3 (b) shows a simply supported piezoceramic stack, used as the final design due to dimensional and performance advantages as compared to the cantilever assembly. The stack has a footprint of 37 x 75 mm and rises 5mm above ground, less than half as much as the cantilever. It consists of two piezoceramic layers with two smaller elements on each layer, which are glued to Fiberglass sheets with foam layers covering the top and bottom face of the stack. By using two layers instead of four, the height of the assembly is significantly reduced in comparison to the cantilever design. The stack was placed inside the shoe with inner ribs carved out. The hollow interior of the shoe heel has a depth of 1 cm allowing 3mm layer of foam to be placed atop the stack. A few pictures of the shoe and the stack are in Figure 4-4.

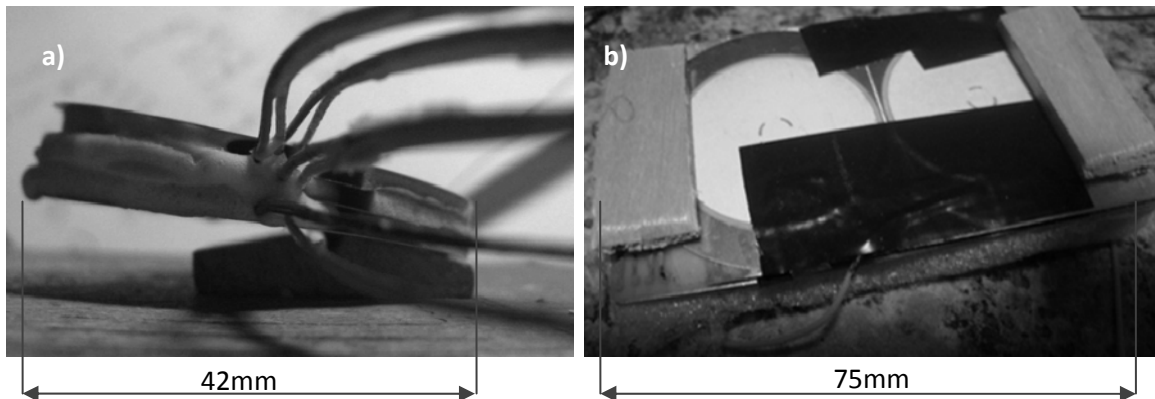


Figure 4-3: Cantilever piezoceramic stack with foam filling the space between piezoceramic layers. (b) The bottom view of the simply supported PZT heel insert assembly. The wooden supports at either end can be seen here.



Figure 4-4: Shoe with piezo stack installed. No Exterior modification was required. (b) inner rubber rib structure of the shoe which was later cut out for the in-heel insert as shown in the image (c) and (d).

For measuring the power generation capacity of the circuit, the voltage from the PZT stack is rectified and applied across various loads, the results of which are presented in Figure 4-5. The voltage rises with the resistance with global maxima at a resistance of  $50\text{ k}\Omega$  after which it starts to drop till about  $390\text{ k}\Omega$  was calculated to be  $10\text{ mW}$  with peaks rising as high as  $30\text{ mW}$ , as shown in Figure 4-6, before starting to rise once again with increasing resistances. For the  $50\text{ k}\Omega$  load, the average power of  $10\text{ mW}$  was measured with peaks rising as high as  $30\text{ mW}$ .

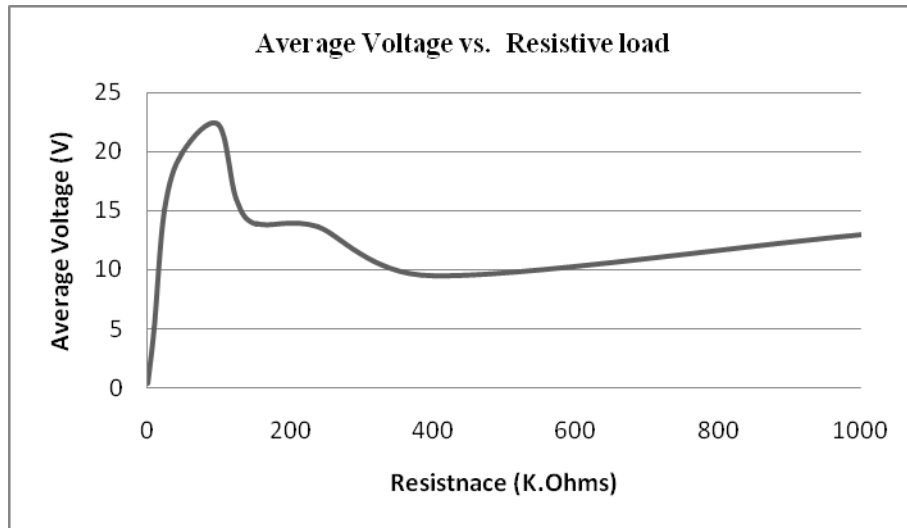


Figure 4-5: Average voltage produced by the PZT stack across various resistive loads

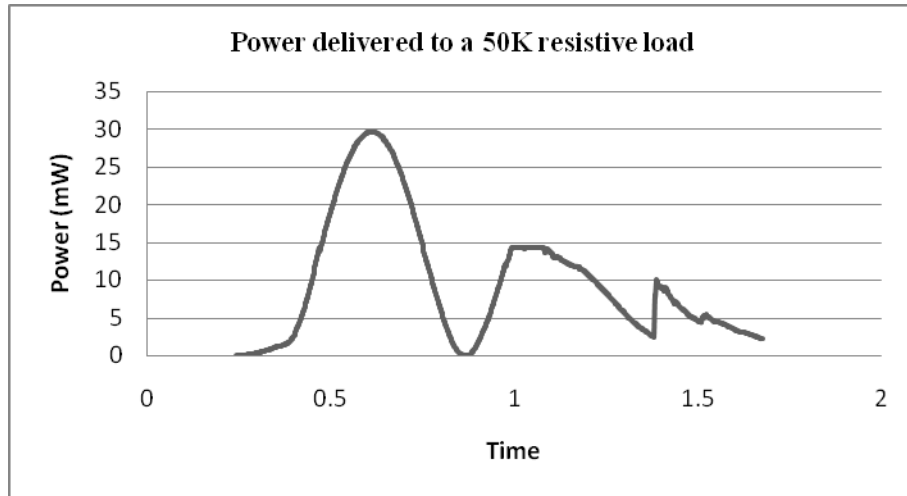


Figure 4-6: Power delivered by the PZT stack into a  $50\text{ k}\Omega$  resistive load

Even though power measurement is paramount for quantitative analysis and identification of loads supportable by the energy harvesting device in question, it is not the best measure and could be misleading to some degree. This is because of the vast difference in resistive loads used for estimating deliverable power and the resistive load of the device that is actually to be powered by the harvesting unit. The dependence of average voltage upon the resistance of the load and thus the power delivered has already been demonstrated in Figure 4-5. A better way to compare various energy harvesting units is the rate of voltage accumulation in a capacitor. Figure 4-7 shows voltage accumulation in

a  $47 \mu\text{F}$  capacitor due to successive stepping during regular walking action conducted at the rate of 1 step per second. Three (3) trials were conducted to verify the validity and repetitiveness of results as shown. 12.4V is accumulated in the capacitor after 6 steps with final voltage rising as high as 22V with 13 steps.

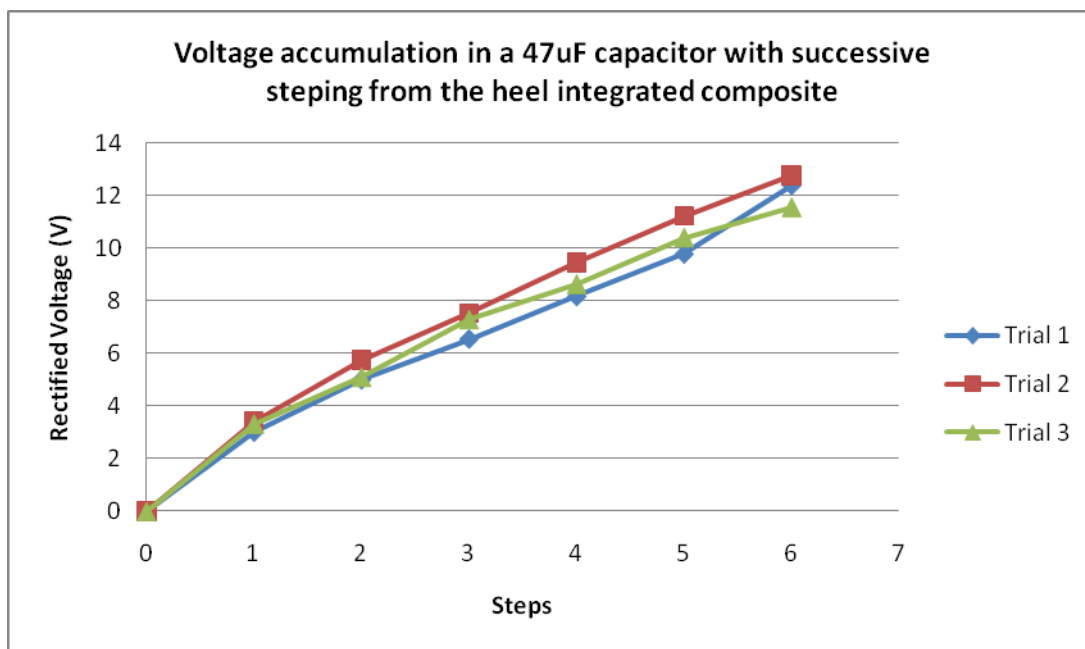


Figure 4-7: Rise in voltage across of a  $47 \mu\text{F}$  capacitor with each step from the heel based piezo composite.

Three trials were conducted to confirm the accuracy of results. 12.4V is accumulated after 6 steps

#### 4.4.1.2 In-sole integrated composite

A second design that is developed for power generation within the shoe involved the fabrication of a new multilayer in-sole composite as well as the modification of existing in-sole to incorporate power generation and storage layers. For this purpose, a circular PZT bimorph of 40 mm diameter and 0.5 mm thick is used for power generation. The bimorph, positioned to lie under the heel, is surrounded with foam cutout in the shape of the insole. The insole is kept thicker at the rear with a frontwards taper, which cause ceramic to lie slanted with respect to the ground, as shown in Figure 4-8. There is more foam under point B than is under point A, which means that point B can move down more compared to point A due to higher compressibility of foam section under the

element at point B. The less amount of foam under point A acts more like a fixed support. Upon the application of weight the thickness taper of foam causes the rear half of the piezoceramic element to move down more than the front half thus forcing it to bend – bending generates electricity. The actual pictures of the foam insole can be seen in Figure 4-9.

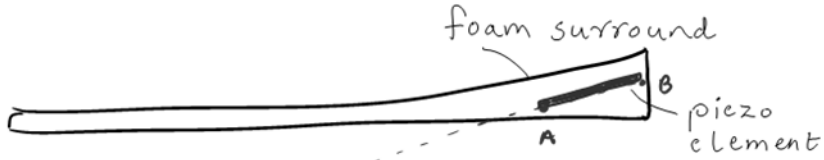


Figure 4-8: Side view of the foam insole with piezoceramic element (blue) near the heel portion.

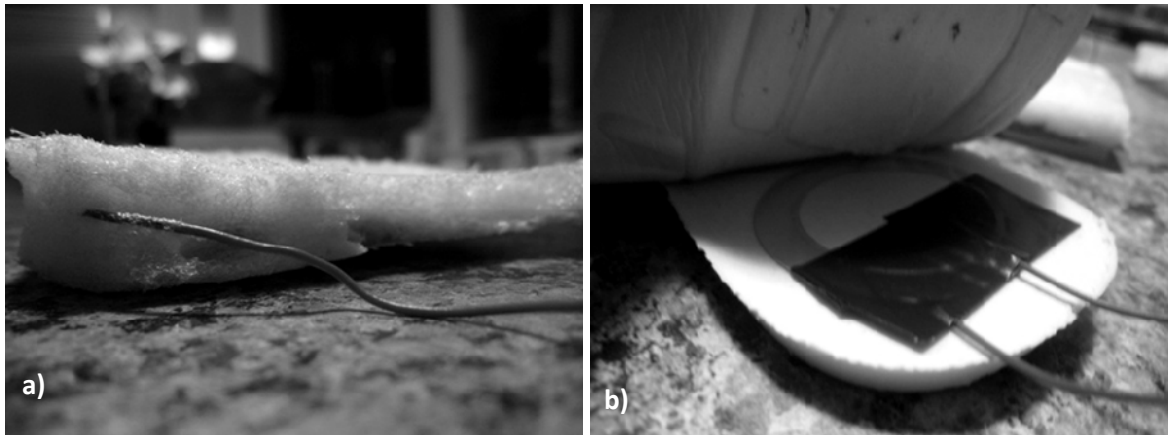


Figure 4-9: Foam insole with piezoceramic element near the heel area. (a) The thickness taper and the slanted angle of the custom made sole can be seen. (b) A commercially available foam insole with PZT bimorph placed between tapers layers

The charge from the insole is stored in a  $47\mu\text{F}$  capacitor in a manner similar to that for the in-heel design for the sake of comparison. As expected, the insole generates less charge, as shown in Figure 4-10, when compared to the results shown in Figure 4-7 due to reduced bending of the bimorph as well as less numbers of bimorph used; 1 for the insole compared to 4 for the in-heel. The capacitor is charged to 4V after 6 steps compared to 12.4V from the in-heel PZT bender stack. 2.1 milliwatts of power is harvested from the insole with integrated PZT bimorph. Nonetheless, the insole design is much closer to a regular insole due to minimal thickness (less than 0.5mm) of the piezo

element being used and seamless integration of the power harvesting element. The comfort is barely compromised as the element is soft enough to morph resulting in negligible change in walking comfort.

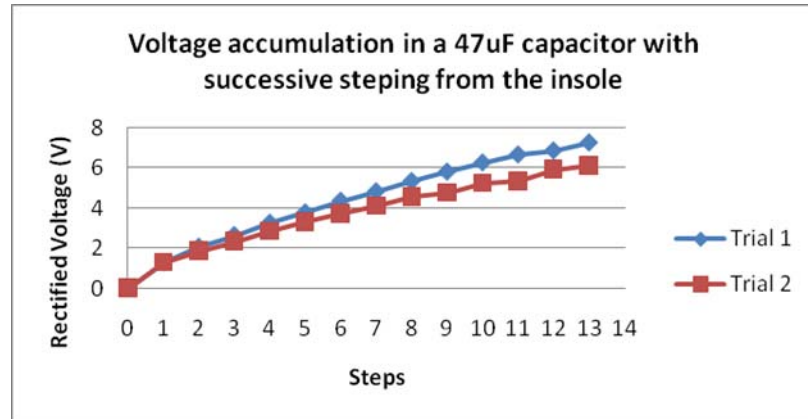


Figure 4-10: Capacitor charging from insole

#### 4.4.2 Structure – walking comfort

Regular shoes make use of a foam/silicone insole to provide cushioning of the heel during walking/running. The PZT bimorph stack developed here requires bending to generate power. The inherent elasticity of brass/epoxy layers used to reinforce the otherwise brittle PZT layers serve the same function as that of a compressible foam insole. The insole usually compresses by anywhere between 2 to 6 mm depending upon the type and unloaded thickness. The bending configuration developed here has a maximum deformation of under 3 mm; comparable to that of a regular insole, which could be increased or decreased easily by slight modification of the design. Moreover, surrounding the bending structure with foam provides an additional layer of cushioning further enhancing comfort. Figure 4-11 shows the different layers of the PZT stack.

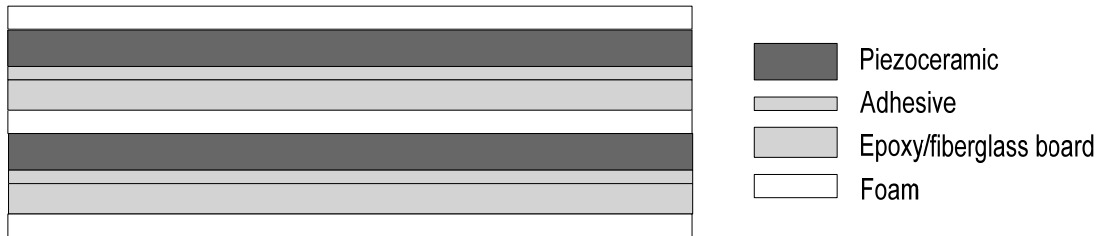


Figure 4-11: Layers of the composite with PZT/brass bimorph layers bonded to epoxy structural layers

as well as allows them to deform without failure. The epoxy-based fiberglass board also provides the elasticity required for the rebounding action at the removal of force eliminating the need for compressible foam or rubber structure. The use of fiberglass board means that the circuit required for rectification and storage of power can be made directly on it thus eliminating the need for separate components/layers while integrating everything into a compact design. In this manner, the fiberglass board provides true multifunctionality by fulfilling various structural roles as well as allowing the necessary circuit to be fabricated directly onto it. Figure 4-12 shows the PZT bimorphs attached to the fiberboard along with the rectification circuit.

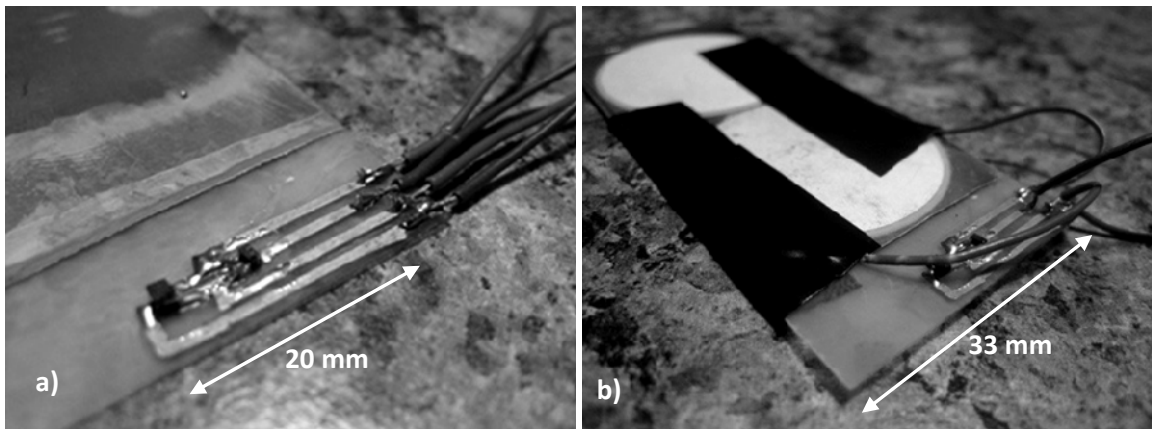


Figure 4-12: Rectification circuit fabricated directly onto the fiberglass (left), and (b) single layer of piezo stack with circuit

The rectification circuit shown above is required only on one of the layers of the piezo stack since all the piezo elements are connected together in parallel. Such an arrangement reduced the number of required electronics components (rectifiers and capacitors) thus simplifying the design of the structure and the electronic circuits.

#### 4.4.3 Storage

As mentioned earlier, two options for the storage of harvested power are considered, 1) thin-film capacitor and 2) Thin-film battery. Figure 4-13 (a) shows the thin-film polypropylene capacitor on the left, which is made simply made from two conductive films bonded to a very thin wax paper layer diped in an electrolyte. The layers are then packaged in a sealed envelope to prevent electrolyte evaporation and leakage. Capacitance value of  $10 \mu\text{F}$  is achieved for an area of  $2500 \text{ mm}^2$ . However, since the thickness of the capacitor is less than  $0.05 \text{ mm}$ , several layers can be folded and assembled together thus increasing the capacitance to any desired value. An aluminum-polymer capacitor type capacitor which utilizes aluminum oxide layer as the dielectric and a conductive polymer as one of the electrodes has been constructed in a thin-film format. These capacitors have a higher capacitance per unit area and will not require folding multiple capacitor layers to arrive at the desired capacitance. Moreover, since an electrolyte is not needed, the layers of the capacitor do not need to be packaged and sealed.

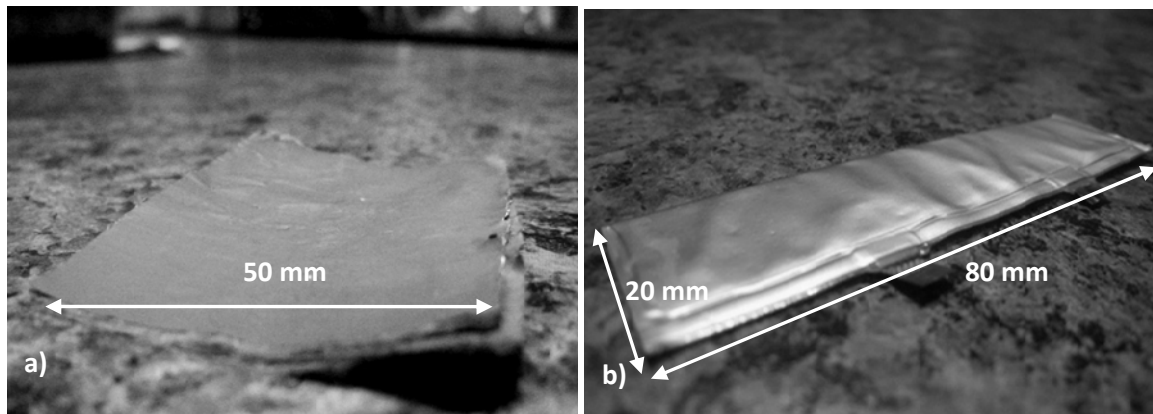


Figure 4-13: (a) An unsealed Thin-Film electrolytic capacitor at less than  $0.05 \text{ mm}$  thick, and (b)  $0.7 \text{ mm}$  Thin-film battery.

The second option of the thin-film battery is far too complicated for the skills and resources available at hand and thus a ready made battery with a capacity of  $100\text{mAH}$  at

A thinfilm 3.3V Lithium Ion battery, measuring  $20 \text{ mm} \times 80 \text{ mm}$  with a height of  $0.7 \text{ mm}$  is used for permanent storage of power – shown in Figure 4-13 (b). The structure of the

battery is shown in Figure 4-14. The substrate layer of the battery can be replaced with the fiberglass board from the piezo stack thus reducing the number of overall layers required. The thin-film battery is placed at the very bottom of the stack.

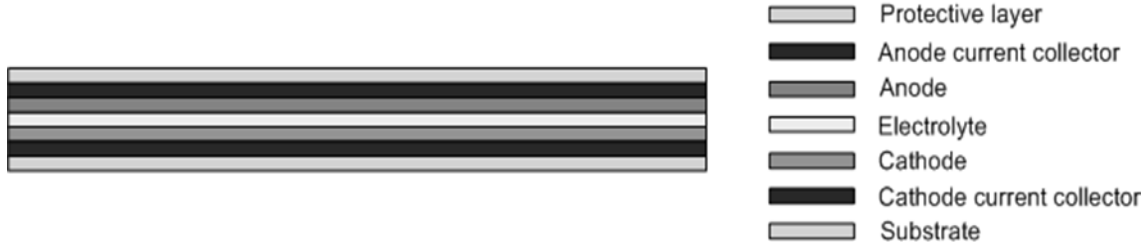


Figure 4-14: Structure of a thin-film battery

#### 4.5 HARVESTING CIRCUIT OPTIMIZATION

From Figure 4-7 and Figure 4-10, it is evident that the rate of voltage rise in the capacitor is higher at low capacitor voltages, primarily below 5V, simply because of the RC constant of the capacitor that dictates the charging behavior. Figure 4-15 shows the declining rate of voltage rise across the capacitor. The rise in voltage from the first step is around 3.5V whereas that from the third step is just 1.75V; half of the first step. Even though the voltage rise declines, the power delivered per step does not. For the 47  $\mu\text{F}$  capacitor, the power is highest at the 10<sup>th</sup> step when the capacitor voltage is around 17.87V. Thus more power can be recovered if the voltage of the capacitor is maintained above 15V, between 8<sup>th</sup> and 11<sup>th</sup> step. Bearing this fact in mind, a voltage regulator is used that only supplies power to the load when the capacitor voltage rises above 15 volts. As the voltage of the capacitor rises above this threshold, the regulator discharges the capacitor maintaining the capacitor voltage steady at 15V thus extracting maximum power. In this mode, the regulator works intermittently with the frequency of operation dependant upon walking speed. A similar approach of intermittently powering low-power devices is taken by Kymisis [18] and Kaajakari [19].

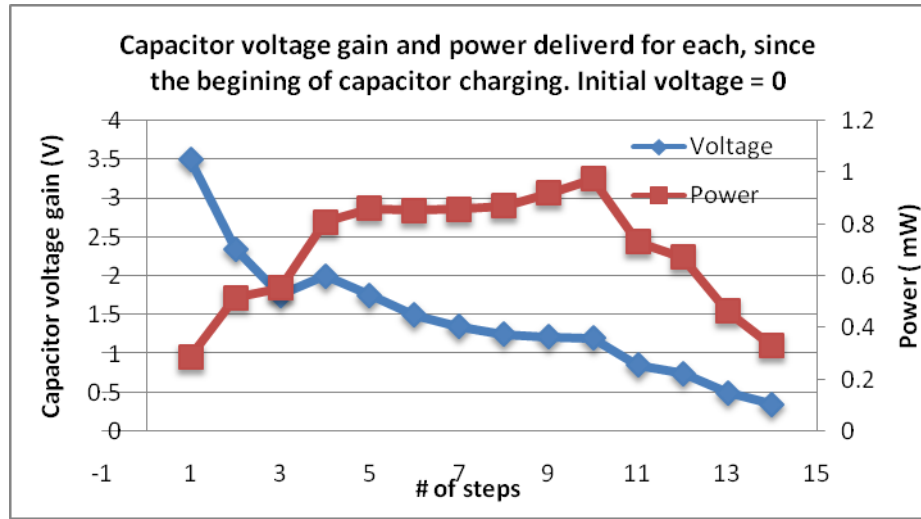


Figure 4-15: Relative voltage gain in a  $47\mu\text{F}$  capacitor from successive stepping.

Figure 4-16 shows the complete energy harvesting and regulation circuitry. 3.6V is supplied by the regulator, sufficient to charge a 3.3V lithium battery.

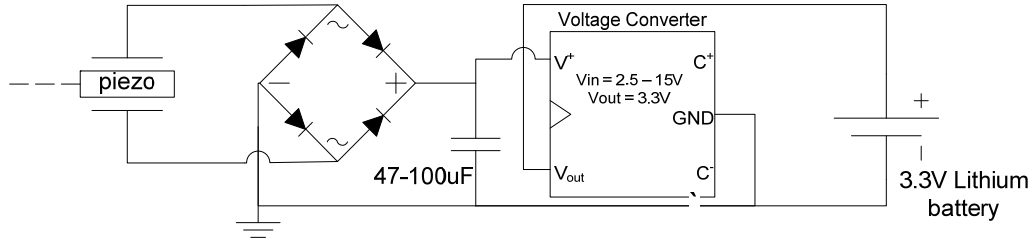


Figure 4-16: Schematic of the energy harvesting circuit

The 3.3V rechargeable lithium battery is presented as an example usage of the harvested energy. Other potential applications include intermittent GPS transmitters, RFID tags, Running/walking speed counters etc.

## *Chapter 5: PNEUMATIC TIRE-BASED PIEZOELECTRIC POWER GENERATION*

### **5.1 POWER GENERATION METHODOLOGY**

The weight of the vehicle acts on the tire-to-road contact interface surface with the sidewalls of the tire and the air pressure within the tire acting as intermediaries. When the weight on the tire is zero (0), the tire-road contact interface is nearly a line. As the load on the tire is increased, it causes the tire to deform and flatten out at the bottom resulting in a larger contact area between the tire and the road surface, called the contact patch. Furthermore, the sidewalls of the tire just above the contact patch experience deformation as well. As the tire rotates, the tread-wall as well as the sidewall undergoes cyclic deformation at a frequency that is a function of tire RPM, i.e., the vehicle speed. Thus, two opportunities exist for the generation of power using piezoelectric bending elements at the inner treadwall and the inner side-wall surfaces of the tire. The use of piezo benders for power generation was made popular through the development of THUNDER piezo bender, developed by NASA. One of the first uses of such benders appeared in piezo harvesting shoes [18]. As the tire rotates, piezoceramic benders attached to the inner surface of the tire experience periodic deformation and relaxation generating a periodically oscillating charge, the frequency of which is a function of tire RPM [36].

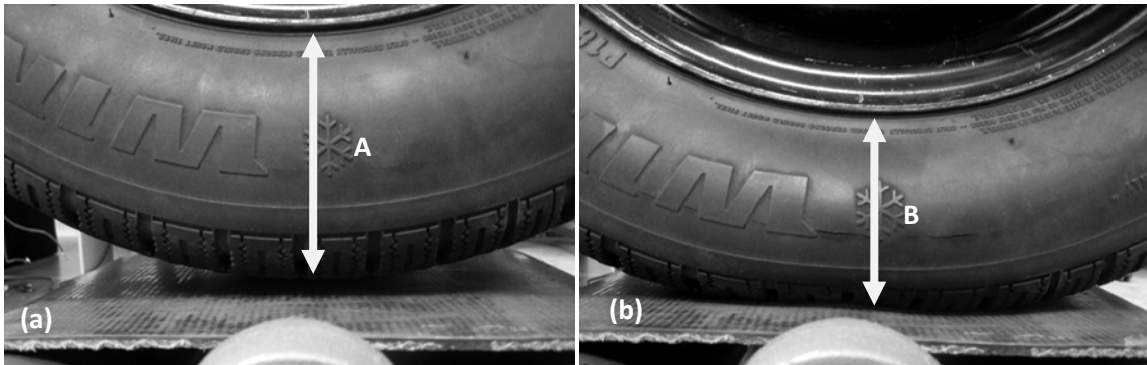


Figure 5-1: (a) Non-deformed tire at no loading and (b) Formation of contact patch due to deformation of a loaded tire (right). The reduction in sidewall height due to deformation is also visible i.e. A > B

### 5.1.1 Treadwall/Contact patch deformation

A 185/65R14 tire has an inner treadwall that is 5 inches wide and 69 inches long, an area of  $345 \text{ in}^2$  ( $222580 \text{ mm}^2$ ). Based on a contact patch length of 5.5 in (140 mm) for average size passenger vehicle, 8% of the treadwall area is deformed at all times during vehicle operation. A small piezo element attached to this surface would deform with the tire as shown in Figure 5-1 above at frequencies as presented in Table 5-1. The higher the velocity the more frequently the bender deforms thus increasing the power output. As a proof of concept, initial tests were conducted using generic benders of circular cross section glued directly to the tire, which produced voltages in excess of 25V at 1Hz.

Table 5-1: Frequency of piezo bender deformation as a function of vehicle speed

Tire diameter* (in)	Speed (km/h)	RPM (revs/min)	Frequency (Hz)
24	10	87.03	1.45
24	20	174.05	2.90
24	30	261.08	4.35
24	40	348.11	5.80
24	50	435.13	7.25
24	60	522.16	8.70
24	70	609.19	10.15
24	80	696.22	11.60
24	90	783.24	13.05
24	100	870.27	14.50

### 5.1.2 Sidewall deformation

Sidewall deformation occurs in a manner similar to that of the treadwall but occurs at a greater degree i.e. the same piezo bender attached to the sidewall would produce more power due to higher deformation. Even though the sidewall location seems to be ideal from a power generation point of view, there are however difficulties in attaching

piezoceramic bender elements to it because of its uneven and severe deformation during installation of the tire onto the rim and the removal thereof.

## 5.2 TIRE PATCH CONSTRUCTION

### 5.2.1 *Piezo element selection*

The piezoceramic elements used in this research project were selected based on 3 main criteria:

- 1) Bendability – the piezoelectric elements must be able to deflect/deform with the tire without damage
- 2) Output power – is a function of the piezoelectric charge constant,  $d_{33}$  and element thickness. The charge constant for Lead Zirconate Titanate (PZT) piezoceramic is 110 whereas that for Polyvinyl fluoride polymer (PVDF) is about 33.
- 3) Cost – low cost is an important factor for practicality of tire based power generation.

Of these factors, sufficient bendability of the element is of utmost important to match the cyclic deformation of the tire, which is 540 million cycles for a tire life of 100,000 kilometres. A highly bendable element is likely to last longer than one which suffers from limited bendability. Table 5-2 shows the required deflection of the piezo element as a function of element size for an internal tire radius of 11 inches.

Table 5-2: Required end-to-end deflection of piezo benders of different sizes

Tire radius (in)	Piezo length (in)	angle of deflection (degrees)	Required deflection (in)	Required deflection (mm)	# of Elements (1.75 in)
11	0.5	1.302	0.011	0.289	138
11	1	2.604	0.045	1.154	69
11	1.1	2.865	0.055	1.397	62.72727
11	1.2	3.125	0.065	1.662	57.5
11	1.3	3.386	0.077	1.951	53.07692
11	1.4	3.646	0.089	2.263	49.28571
11	1.5	3.907	0.102	2.597	46

The deflection values presented in the above table are beyond the capability of commercially available PZT elements. PVDF elements are popular for their inherent flexibility but suffer from poor charge output as well as very high costs as compare to their PZT counterpart. Table 5-3 compares PZT and PVDF based on the above mentioned criteria.

Table 5-3: Qualitative comparison of (PZT) and (PVDF) piezoelectric benders

Criteria	PZT	PVDF
Bendability	Low	Very High
Piezoelectric Charge constant ( $d_{33}$ )	High (110)	Low (33)
Cost	Element dependant	Very High
Temperature range (C)	High (up to 130)	Low (Up to 80)

Except for bendability, PZT elements are more attractive for power generation and were thus the primary choice. However, since bendability could not be ignored, unconventional piezo benders which are typically used for buzzers and have never before been used for power generation were selected. Similar elements have previously been used by the authors to harvest power from shoes through deformation in the show sole during walking motion. Shown in Figure 5-2, these elements have a depth of 0.23 mm including the brass plate making them highly bendable. The factory received element had a diameter of 44 mm (the, however, excess metal was cut out attain a rectangular shape of size 40 x 25 mm. These benders were tested to deform in excess of 10 mm, far greater than the required deformation values of Table 5-2.

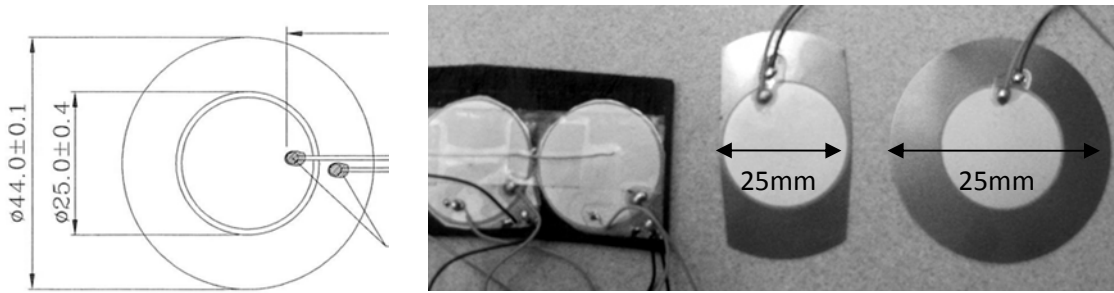


Figure 5-2: Factory shipped PZT bender (right) compared to a penny, 25mm x 40 mm brass cut out (center) and 25mm diameter brass cut out (left)

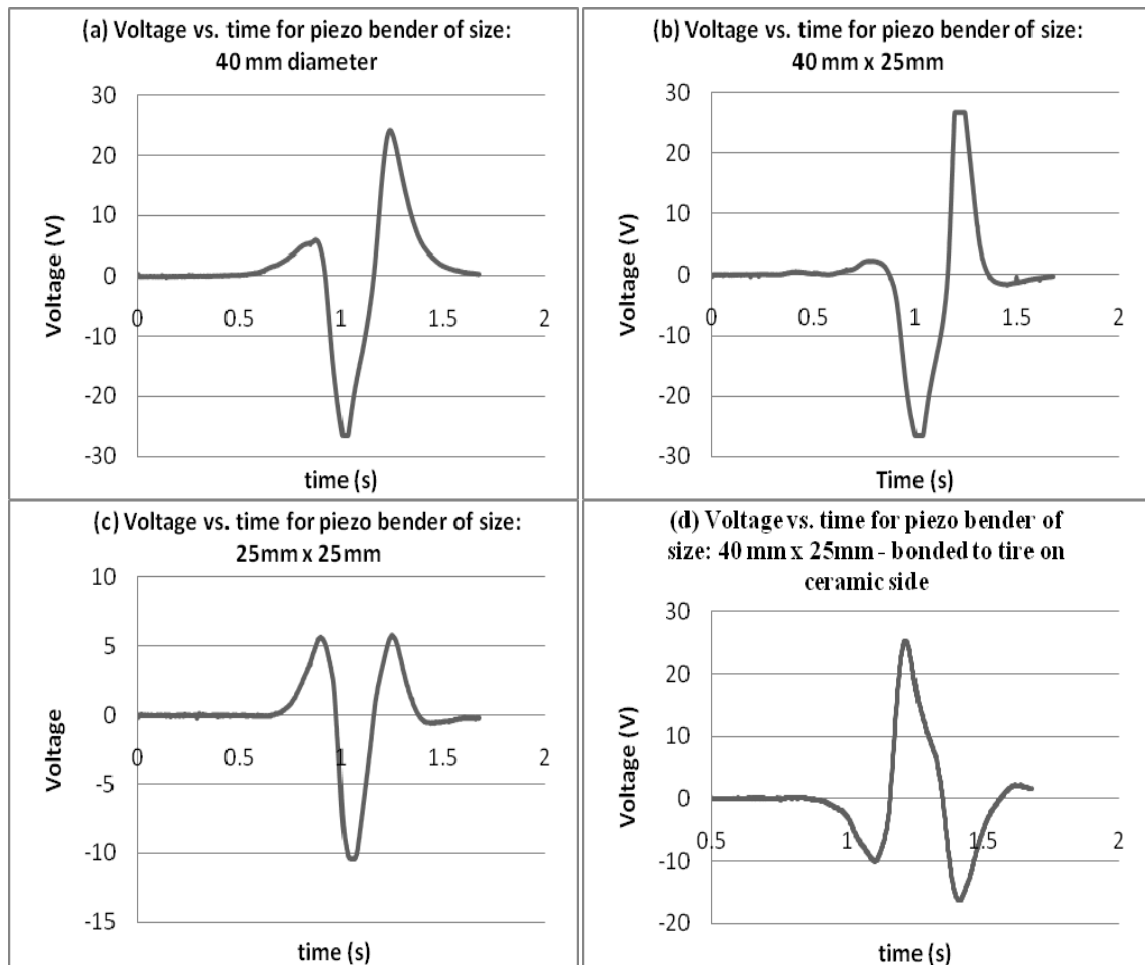


Figure 5-3: Voltage response due single deformation from (a) full element (b) 40 x 25 mm cut out (c) 25 mm diameter cut out and (d) 40 x 25 mm upside down bonded piezo bender element

For space optimization and attaining higher piezo coverage densities, excess brass was cut out in different ways to test the dependence of charge output on element shape, the results of which are presented next in Figure 5-3. As evident, removal of excess brass around the ceramic disc reduces the voltage output significantly. However, reshaping the element down to 40 mm x 25 mm and bonding it so that the longer edge is along the circumferential direction doesn't affect the voltage output as can be seen from Figure 5-3 (a) and (b). Removal of excess brass allows more elements to fit into the same area.

### 5.2.2 Element layout

The piezo elements were arranged in 40 rows of 4 elements each as shown in Figure 5-4 (a). Since elements within a row would undergo deformation simultaneously, they were connected in parallel to a rectifier with all the rectifiers then themselves connected in parallel. The first piezo-patch was created by gluing piezo elements onto a 4.5 inches wide and 69 inches long rubber sheet; enough to cover the entire inner circumference of a 185/65R14 tire. Creating a rubber based patch allowed easy assembly of the patch itself, which included PZT element adhesion, wire connections, rectifier board soldering to each row and interconnection of rectifiers in parallel. However, one continuous patch proved troublesome for manual adhesion onto the tire resulting in large air bubbles and thus loss of power output during initial tests. This problem was remedied by splitting the one-piece patch into 20 smaller patches that could be bonded separately to the tire ensuring all-round adhesion with no air pockets.

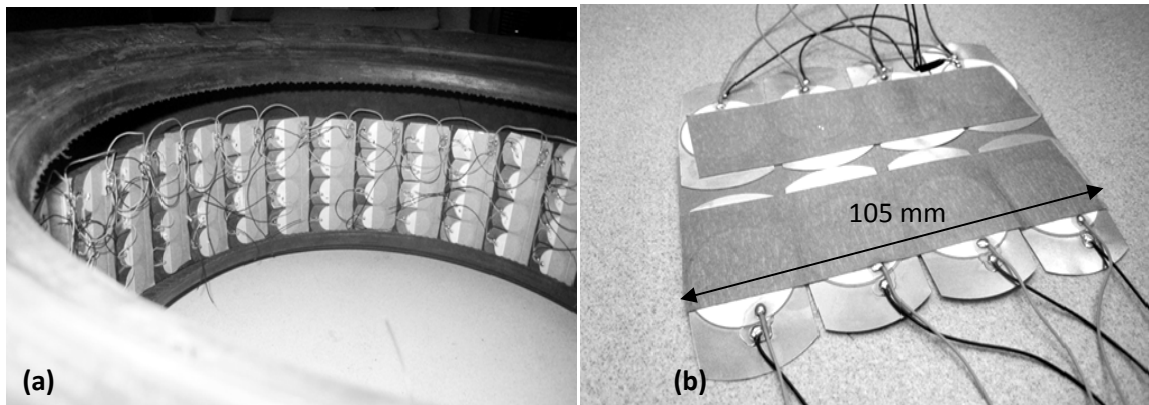


Figure 5-4: (a) PZT bender patch installed on the treadwall of the tire. (b) 2-row small patch ready to be bonded to the tire

Though, the assembly of the patch was greatly simplified, the rubber base increased the weight of the patch significantly without contributing towards power generation. For the second and final patch 2 rows of PZT elements were grouped together for easy adhesion to the tire (Figure 5-4 b). Paper tape was temporarily used to keep the elements together until they bonded to the tire and then removed.

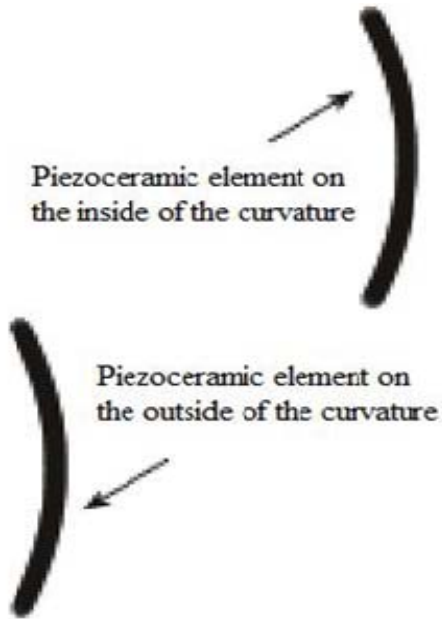


Figure 5-5: Concave and convex deformation of piezoceramic elements

The piezo elements are capable of bending more in concave manner i.e. with the ceramic on the inside of the curvature rather than on the outside (convex). Figure 5-5 shows the concave and convex deformation of PZT bender element. When the vehicle is driven on smooth even road surface, the tire deformation causes the PZT element bonded to it to deform as intended. However, while driving over pits, bumps and other road irregularities the tire experiences extreme irregular deformations that could damage the PZT element. To prevent extreme concave and convex deformations the adhesive was only applied on the centerline of the elements, as shown in Figure 5-6 (b), rather than over the entire element area. This technique ensures optimal concave deformation while significantly reducing convex deformations. Figure 5-6 (a) displays the bendability of the rubber-base patch created using this bonding technique.

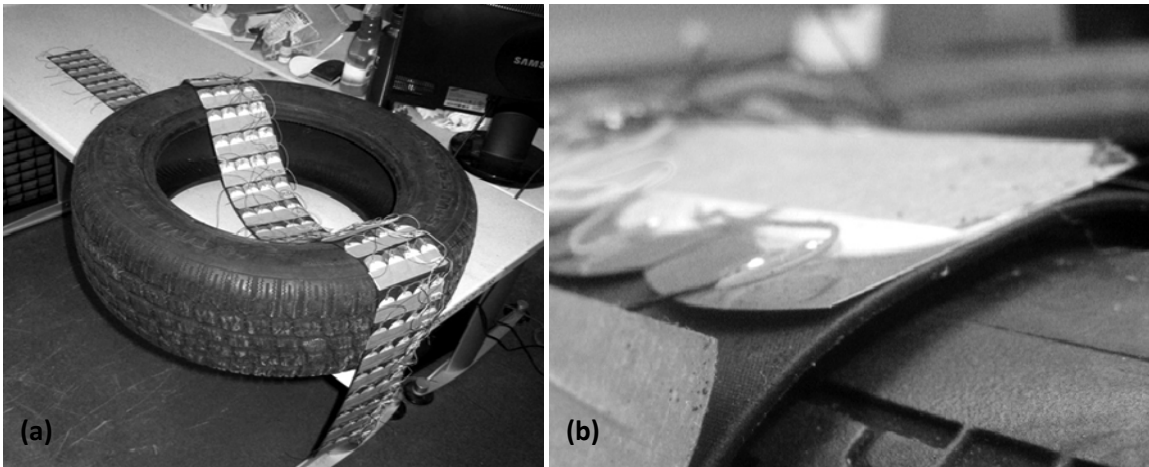


Figure 5-6: (a) Flexibility of the piezo patch. (b) Centerline bonding of the piezo element onto rubber substrate

The choice of adhesive to bond piezo elements to the tire was influenced by the harsh environmental conditions that exist inside the wheel assembly during driving. The basic requirements for the selection of appropriate adhesive included:

- 1) Wide temperature range (-40 to 70 C) – for high temperatures developed during driving and low temperatures experienced during winter<sup>3</sup>.
- 2) Excellent adhesion to metals and rubbers
- 3) Adequate flexibility – to allow deformation of PZT material with tire.
- 4) Moisture resistant

A cyanoacrylate adhesive was used at first due to quick bonding (within 45 seconds) making it easy to attach the piezo elements to the tire but proved to have poor flexibility during testing. Parmatex® Weatherstrip Adhesive [37] proved to be a better choice due to its flexibility, excellent adhesion to rubber and metals, wide operating temperature range (-54 to 204 C), vibration, oil, grease and moisture resistance.

### 5.3 TESTING

The tires were tested using the Tire Dynamometer described in chapter 2.

## 5.4 EXPERIMENTAL RESULTS

Power measurements from the tire were conducted by rotating the tire at different RPM and applying the voltage across known resistance values. Capacitor charging was also conducted to determine optimal capacitance values that could be used in situations where power has to be temporarily accumulated before regulation as is commonly the case with battery charging.

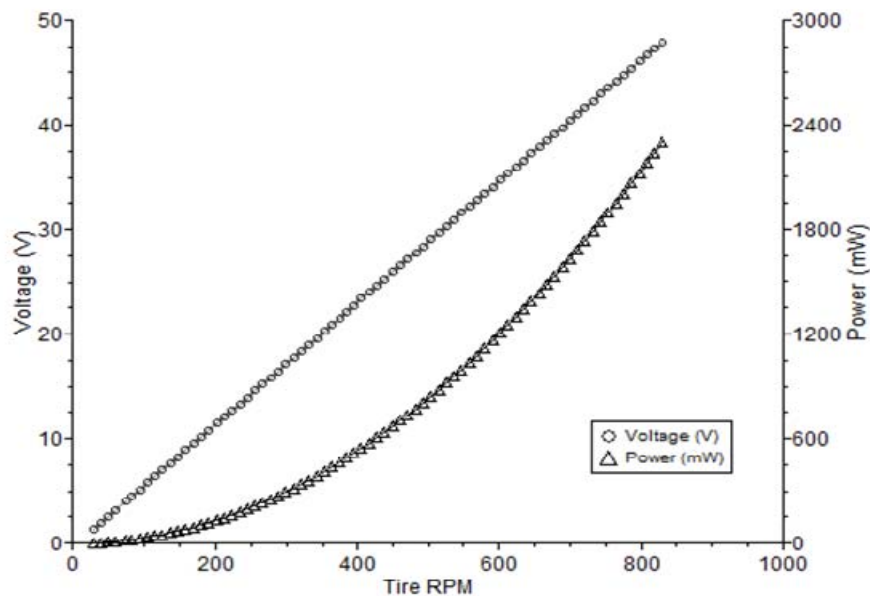
When a resistive load is applied, the average voltage changes with both the load value as well as the RPM. Power in excess of 2 watts can be produced across a  $1000\ \Omega$  load at 854 RPM, equivalent to 100 km/h on the road, by a single layer of PZT bender array. Figure 5-7 shows the power and voltage across a  $1000\ \Omega$  load as a function of RPM. As evident, the power output increases as the deformation frequency of piezo benders increase with RPM.

It has previously [18] been experimentally shown that power is doubled by stacking two layers of piezo benders on top of each other so that the surface area remains the same, in which case the power would effectively double to 4.6 watts.

Figure 5-8 presents the power output across various resistive loads at 60 and 100 km/h equivalent RPM values. The decline in power with the increase in resistance is due the change in maximum voltage, which is 48V at a load of  $1000\ \Omega$  (Power = 2304 mW). For load values other than  $1000\ \Omega$ , the maximum voltage also changes resulting in a change in power values as shown in Figure 5-8.

The power harvested by bonding piezo benders on the inner tire treadwall surface depends upon three factors, namely: 1) Inner treadwall surface area, 2) RPM at 100 km/h, and 3) Piezo bender end-to-end deflection. All of these factors are a function of tire radius i.e. larger radii will results in larger treadwall surface area, lower RPM and lower bender deflection.

Power and Voltage output from piezo-tire vs. tire RPM at 1K Ohm load



$\mu$

Figure 5-7: Power and voltage across a  $1\text{ k}\Omega$  load as a function of RPM

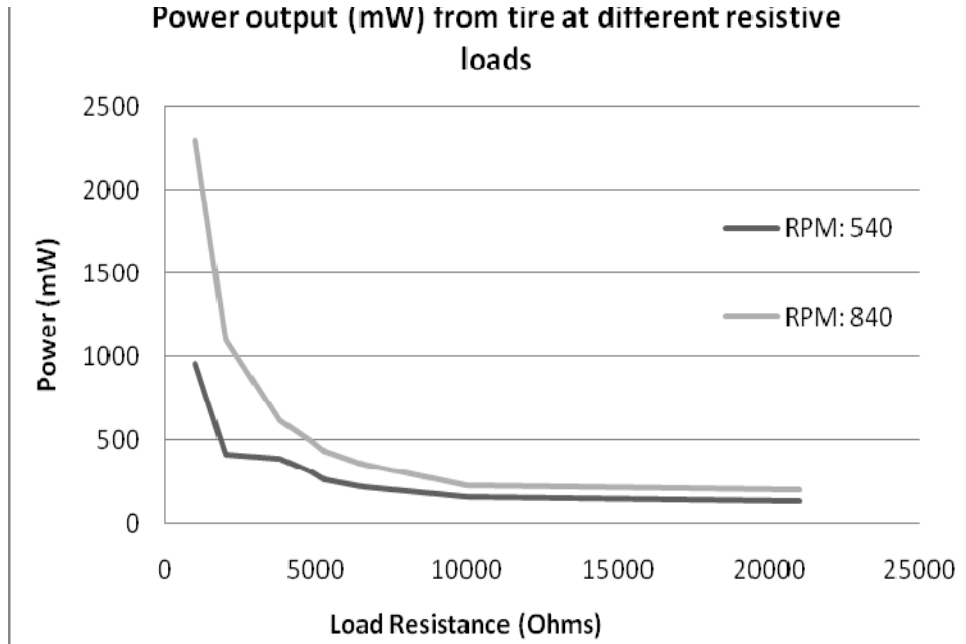


Figure 5-8: Power vs. resistive load at 540 RPM (60km/h) and 840 RPM (100 km/h)

Since power is generated by deformation of the piezo bender elements, the degree of deformation affects and has a positive correlation with the power output i.e. higher deformation of the elements results in a higher power output. The deformation is in turn negatively proportional to the radius of the tire i.e. piezo benders attached to tires of smaller radii would undergo high deformation and thus generate more power than on tires of larger radii. However, larger tires can accommodate more piezo benders due to larger surface area and more piezo benders translate into more power output. Table 5-4 lists the maximum number of elements that can be bonded to the treadwall of tires of various sizes and the end-to-end deformation values for 44mm (1.73 inches) long piezo benders. Tires of large radii also need to rotate fewer times for vehicle speed of 100 km/h and since power output is positively correlated with RPM (Figure 5-7), less power would be generated. Hence, the following relationships are established:

$$Power \propto Surface\ area\ (A)$$

$$Power \propto RPM$$

$$Power \propto Piezo\ bender\ deformation\ (df)$$

Table 5-4: Effect of tire radius on number of piezo benders and their end-to-end deflection

No.	Vehicle	Tire number	Tire Inner Radius (in)	Inner treadwall area (in <sup>2</sup> )	Max # of PZT benders	Deflection angle	Bender deflection (in)
1	Hyundai Accent	P175/70R13	10.32	317.15	176	4.801	0.145
2	Nissan Sentra	P185/65R14	11.23	372.94	207	4.412	0.133
3	Chevy Impala	P225/60R16	12.31	530.67	294	4.024	0.121
4	Pontiac Solstice	P245/45R18	12.34	592.83	329	4.016	0.121
5	BMW X5	P285/45R19	13.55	784.96	436	3.658	0.110
6	Jeep Liberty	P265/75R16	14.82	785.52	436	3.343	0.101
7	GMC Yukon	P235/85R16	14.86	677.29	376	3.334	0.101

Table 5-5: Required RPM of various tire sizes for speeds of 60 and 100 km/h

No.	Vehicle	Tire number	Section width (X)	Rim size (Z)	Aspect ratio (Y)	Tire Radius (in)	RPM (60km/h)	RPM (100km/h)
1	Hyundai Accent	P175/70R13	175	13	0.7	11.32	553	922
2	Nissan Sentra	P185/65R14	185	15	0.65	12.23	512	854
3	Chevy Impala	P225/60R16	225	16	0.6	13.31	471	784
4	Pontiac Solstice	P245/45R18	245	18	0.45	13.34	470	783
5	BMW X5	P285/45R19	285	19	0.45	14.55	431	718
6	Jeep Liberty	P265/75R16	265	16	0.75	15.82	396	660
7	GMC Yukon	P235/85R16	235	16	0.85	15.86	395	658

#### 5.4.1 Power Output and tire contact patch length ( $L$ )

As discussed earlier, deformation of piezo benders occurs at the tire contact patch: piezo bender is bent (concave) just prior to arriving at the contact patch, flattens out at the patch and deforms again as it exits the contact patch. The length of the contact patch depends upon the air pressure in the tire and the load on it. Even though power output is not affected by neither the air pressure nor tire loading, experiments were conducted to determine the dependence, if any, of the on power output on contact patch length.

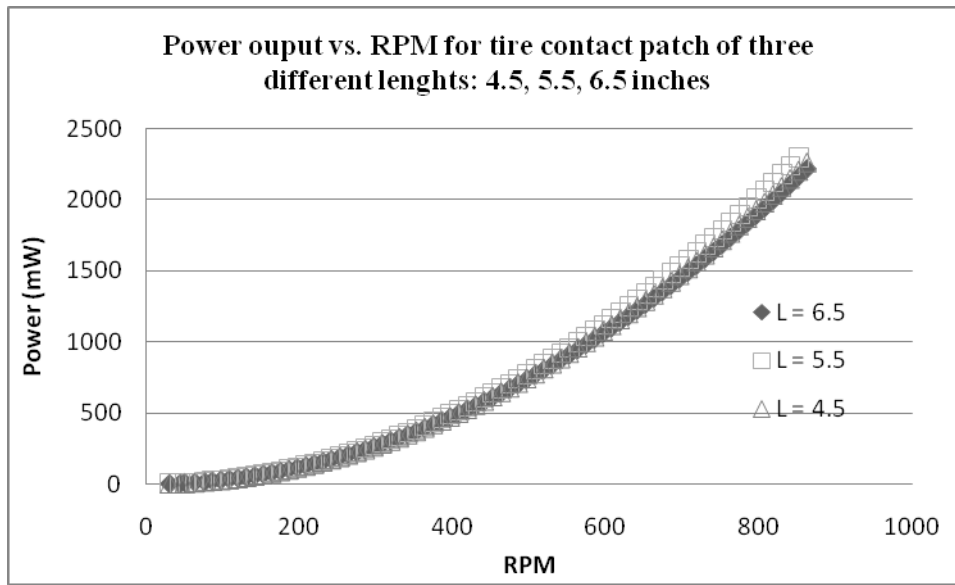


Figure 5-9: Demonstration of the independance of power output on tire contact patch length.

Other factors which affect power include: charge constant of piezoelectric material (d33), thickness of piezoelectric material (d), and piezo element coverage density as described later.

As evident Figure 5-9, the contact patch length does not affect the power output in any meaningful manner. However, for the piezo element to fully flatten out in the contact patch (zero angle of deflection) and produce maximum power, the contact patch length must be at least equal to that of piezo bender i.e. 1.73 inches for the currently employed benders.

$$\text{Contact patch length } (L) \geq \text{piezo bender length}$$

## 5.5 ELECTRICAL CIRCUITRY

As mentioned earlier, the circuit consists of 4 piezo elements of a row connected in parallel to a rectifier bridge, with all rows connected in parallel to each other. In this manner, the row of elements producing power acts as a voltage/current source while the rest of the rows act as open circuits due to diodes in the rectifier bridges functioning in reverse biased mode.

### 5.5.1 Power transmission from piezo patch to rim

Power harvested from the tire has to be transferred to the outer side of the rim before it can be measured or used in chassis components. It is first established that the tire doesn't slide on the rim. There are two reasons for this: 1) tire sliding on the rim would throw the wheel off-balance resulting in vibrations 2) the bead sealer along with the air pressure in the tire provides for sufficient friction to keep the tire from sliding on the rim even during hard breaking. Moreover, a sliding tire is a hazard as it greatly affects the braking ability and vehicle dynamics.

To extract power from the inside of the rim, two holes were made in the rim and insulated with plastic tubing to achieve electrical isolation. Bolts were passed through the tube with steel and rubber washers on either side to prevent air leakage from the tire. Wires from the rectifiers on the tire are connected to the bolt heads on the inner of the rim. Two

more wires were connected to the nuts on the outer side of the rim thus using the bolt-nut combination as airtight electrodes. Figure 5-10 (a) shows the view of the inner side of the side rim with wires connected to the bolts. Figure 5-10 (b) presents a close up view of the bolts. Here the steel washers can be seen on top of the rubber washers, which provide electrical isolation as well as preventing air leakage.

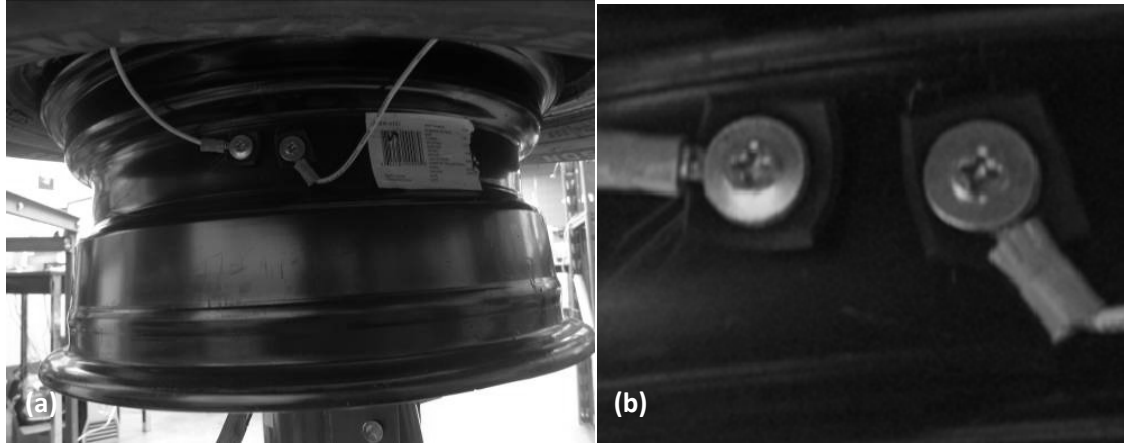


Figure 5-10: (a) Inner side of the rim with wires connected to the steel electrodes. (b) Close-up of the electrode assembly with wire, bolt, steel and rubber washer visible

### **5.5.2 Power loss in Commutator:**

The two brushes of the commutator act as resistors in series with the load resistor. Each brush has a resistance of  $0.7\Omega$  while resistance of load for which maximum power is derived is  $1000\Omega$ . Thus, the load acts as current limiting resistor and the calculations follow:

$$I_{load} = \frac{V}{R} = \frac{48}{1000} = 0.048 \text{ A}$$

Since series circuits have same current flowing across all resistive loads, the power loss in the brushes can be calculated as:

$$P_{brush} = I^2 R_{brush} = (0.048)^2 (0.7) = 1.6 \text{ mW}$$

So, the combined power loss through both brushes is 3.2 mW; 0.14% of power generated at 100 km/h

### **5.5.3 Power loss across rectifiers.**

No electrical component is perfect and diodes are no exception. The losses in the diodes include the voltage drop across it when operating in forward mode and leakage current in reverse mode. The diodes employed in the rectifier bridges have low forward voltage drop of 0.41V and extremely low reverse current leakage of 0.1  $\mu$ A. Each row of piezo benders has its own rectifier bridge and each bridge has 4 diodes; a total of 160 rectifiers for 40 rows. Since only one row produces current at a time, the rectifier diodes in the other 39 rows operate in reverse mode and thus power is lost through reverse current leakage. The total power loss can be calculated as:

$$P_{diode-loss} = (39)(4)(0.0000001 A)(48 V)$$

$$P_{diode-loss} = (39)(4)(0.0000001 A)(48 V)$$

$$P_{diode-loss} = 0.75 \text{ mW}$$

Thus only 0.75 mW of power is lost through 156 rectifiers at operating voltage of 48V.

## **5.6 IDENTIFIED METHODS OF INCREASING POWER OUTPUT**

### **5.6.1 Piezo element density**

Piezo element density simply refers to percentage of piezo-patch area actually covered by piezoceramic elements. The total patch area used on the P185/65R14 tire is 200322 mm<sup>2</sup> of which only 74612 mm<sup>2</sup> is actually covered with piezoceramic material resulting in a patch-to-piezo ratio of 2.68:1. The low coverage density is solely due to the choice of piezo benders used. However, if the entire patch area can be covered with piezoceramic material having similar properties the output can be increased by a factor of 2.68; from 2.3 watts to 6.18 watts per layer.

### ***5.6.2 Piezo stacking***

The 2.3 watts of power generated here was with the use of a single layer of piezoelectric elements. However, multiple layers of elements can be easily stacked on top of each other to multiply the power output. With the current setup of elements, 3 layers can be stacked without requiring any modification of the layout. If 100% piezo density can be achieved as discussed in section 7.1 then the power output can be incremented from 6.18 watts to 18.54 watts.

### ***5.6.3 Sidewall coverage***

Attempts were initially made to cover the inner surface of the sidewalls with piezoelectric ceramics but high and abrupt deformation of the sidewall during installation of tire on the rim and its removal made the usage of PZT elements impossible due to their limited flexibility. A more bendable bender would allow for sidewall energy to be harvested increasing the overall power generation in the tire. PVDF composites are perfect candidates for such high deformation application due to their inherent flexibility. Section 9 presents further details of work being done in this regard.

## *Chapter 6: PIEZOELECTRIC POWER GENERATION FOR SENSOR APPLICATIONS: DESIGN OF A BATTERY-LESS WIRELESS TIRE PRESSURE SENSOR*

### **6.1 INTRODUCTION**

The need to monitor the air pressure of the tire has already been established as one of the basic safety requirements for vehicles especially in North America [29][28]. While TPMSs have been around for more than a decade, they still primarily rely on battery as the source of power. Since battery capacity is limited and its replacement labor intensive and costly, various techniques are utilized to conserve power including the use of micropower electronic components such as microcontrollers, wireless transmitters etc and the incorporation of vehicle motion detection systems to limit the TPMS operation only to periods of vehicle operation. Latter systems are either mechanical, limiting sensor life due to mechanical failures or electronic in which case they often themselves consume power. Furthermore, batteries are environmentally non-friendly since they require proper handling and disposal at the end of product life. A TPMS module that uses energy harvested from piezoelectric materials is not plagued with the above discussed issues and presents itself as the ideal solution for monitoring of air pressure inside the tire. Present alternatives to battery powered TPMS include Surface Acoustic Wave (SAW) based systems [3] as well as piezoelectric energy harvesting modules mounted on the tire [32] rather than the rim. As PZT energy harvesting elements are attached to the tire such sensors are typically installed on the tire [26] itself rather than the rim. This paper discusses two different power generation techniques with two different TPMS module mounting options: one that is mounted on the tire and an alternative design that can either be mounted on the tire or the rim [38].

## 6.2 POWER GENERATION METHODOLOGY

Two different techniques of power generation have been explored and presented leading to fundamental difference in the overall pressure sensor design. The first approach relies on tire bonded PZT benders [36] to generate power resulting in a pressure sensor that is attached to the inner tire surface, whereas the second one discusses a novel approach of power generation within the wheel assembly resulting in a rim mounted pressure sensor; the latter being a more favorable option since it requires minimal changes to the current TPMS sensors.

### 6.2.1 Approach I – Tire mounted PZT benders

The first approach uses the same method of power generation as described earlier in Chapter 5. Figure 6-1 shows the smaller PZT patches used for this application.

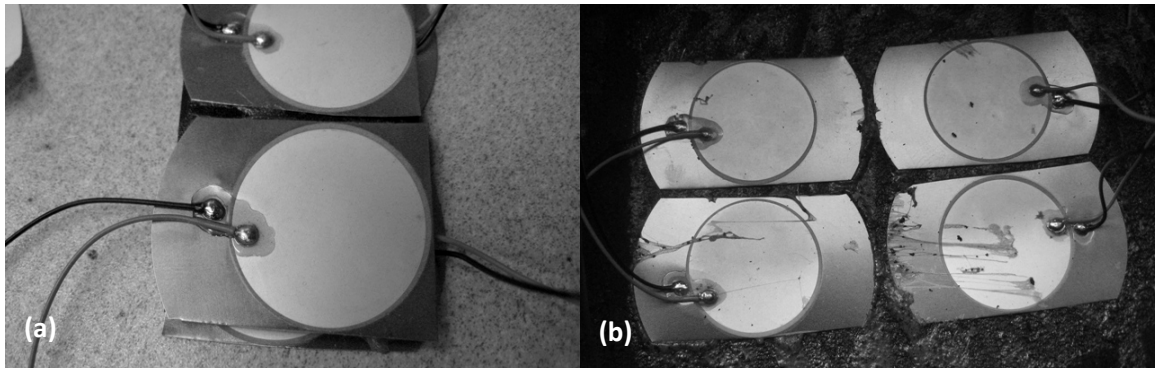


Figure 6-1: (a) PZT bender element of size 1" x 1.5". (b) PZT bender elements bonded to the inner treadwall of the tire.

Figure 6-2 shows voltage build up in various capacitors with the tire rotating at 80 RPM, equivalent to 10 km/h. In all cases, 10V is built up before the capacitor is discharged through a controlled circuit. Since the PZT bender elements produce power solely due to deformation, vehicle weight and air pressure within the tire are not factors affecting the power output<sup>3</sup> and are omitted. These PZT bender elements can handle and end-to-end deflection that is 5 times greater than that experienced on the tire. Moreover, flexibility of adhesive allows the absorption of minor vibrations resulting from road roughness and minor bumps. The PZT bender weighs less than 4 grams and can operate at temperatures

in excess of 100 °C without deterioration in power output thus making them suitable for power generation in tires.

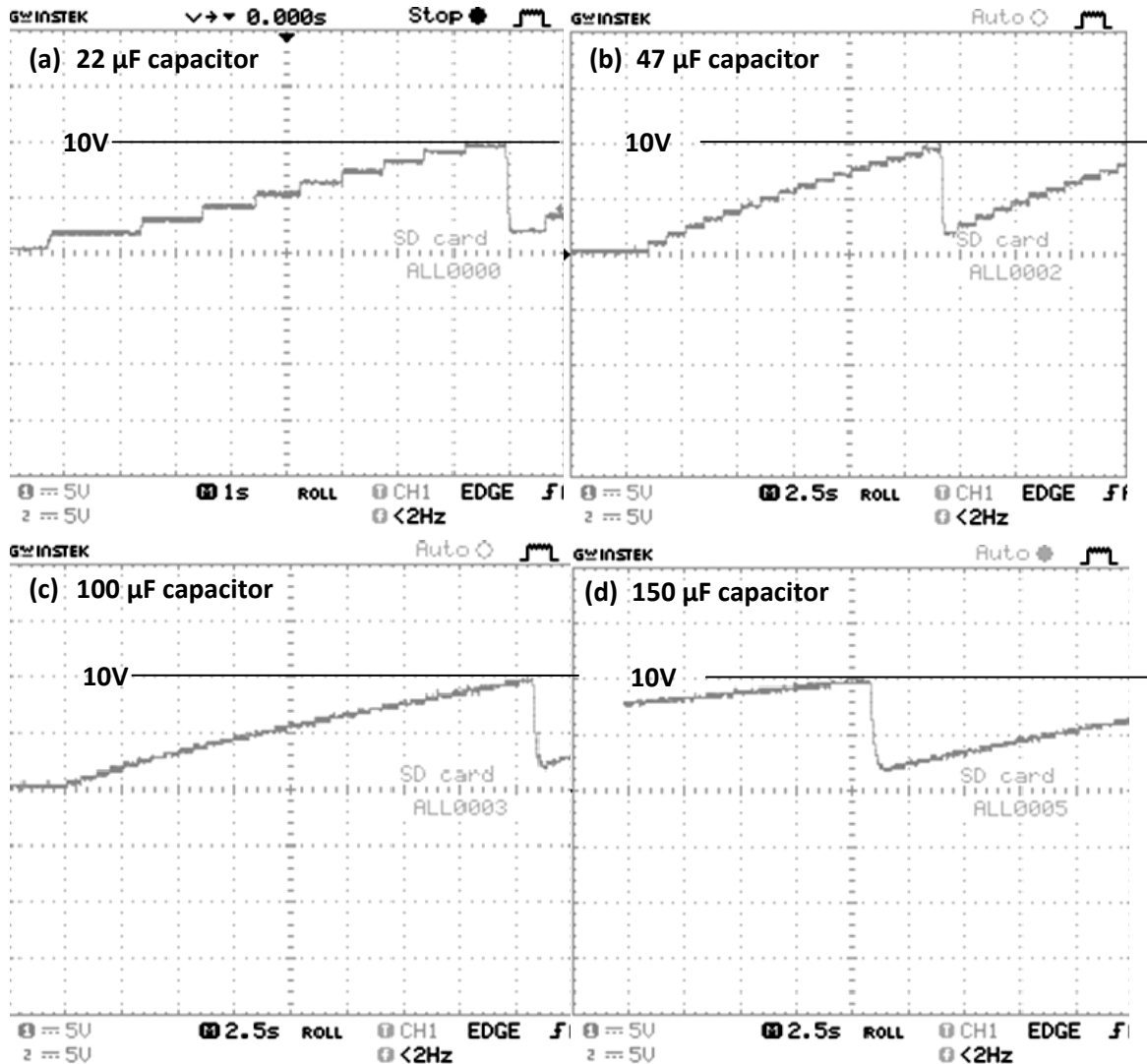


Figure 6-2: Charging of (a) 22 µF, (b) 47 µF, (c) 100 µF, and (d) 150 µF capacitor from tire bonded PZT benders at 80 RPM (~10 km/h)

### 6.2.2 Approach II – Wheel mounted PZT element

A novel method of power generation within the wheel assembly is studied for powering wheel mounted sensors such as TPMS. It involves placement of a very thin piezoceramic (PZT) element between the rim and the tire bead as shown in Figure 6-3. Under normal circumstances when the vehicle is stationary, the air pressure within the tire exerts a

constant force on the tire bead forcing it outwards against the rim. This force is uniform all around the bead-rim interface except for the area of the bead just above the tire contact patch. As shown in Figure 5-1 (b) the sidewalls of the tire above the contact patch also undergo deformation due to vehicle weight and bulge outwards exerting an additional force on the tire bead section just above it. This results in higher force acting on the area of the bead just above the tire contact patch i.e. a net difference in force exists in the bead area above the contact patch and the rest of the tire bead. Thus, a PZT element placed at the bead-rim interface experiences a change in strain due to the difference in pressure-force on the bead as the wheel rotates and as a result generates power.

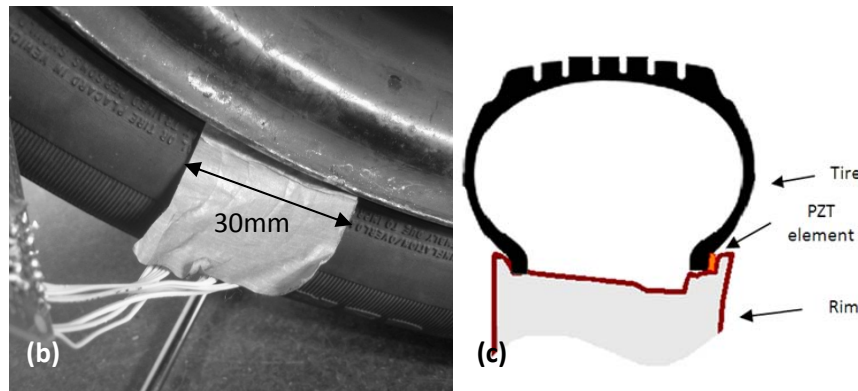


Figure 6-3: (a) PZT element for tire bead-rim interface (b) element placed between the rim and tire at the bead-rim interface (c) graphical representation of PZT element placement

Figure 6-4 shows voltage across a  $22 \mu\text{F}$  capacitor from PZT element placed at the bead-rim interface at a rotational speed of 80 RPM. It takes 180 seconds, 240 rotations, for the voltage to reach the threshold of 10V as compared to 6.76 seconds, 9 rotations, required by the tire mounted PZT bender element. Even though it takes much longer to reach the same voltage level it is still usable harvested power for the purpose of powering TPMSs.

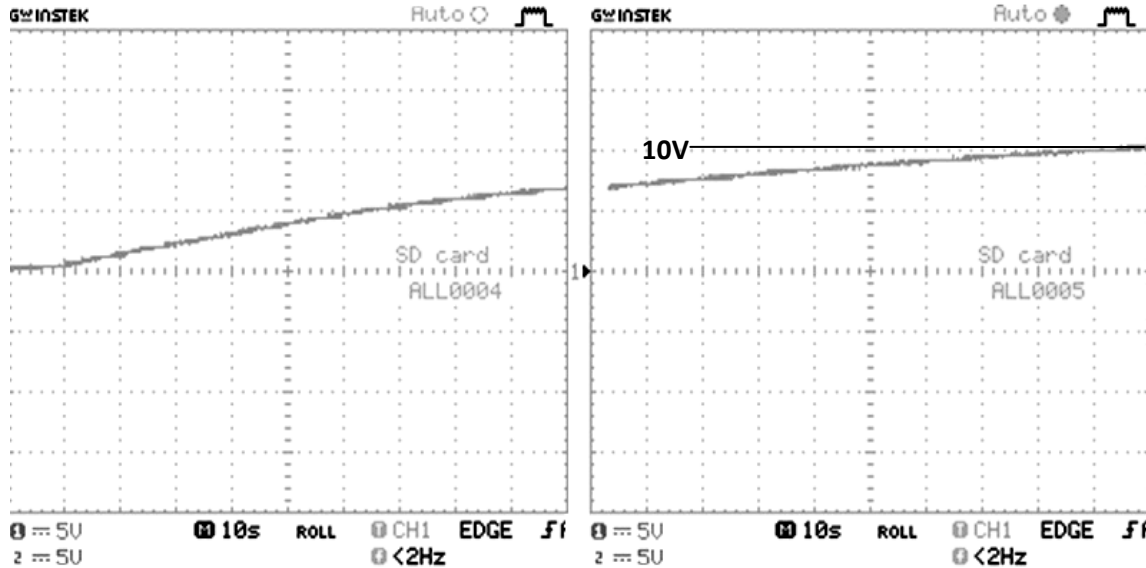


Figure 6-4: Voltage build up in a  $22 \mu\text{F}$  capacitor from rim mounted PZT element

### 6.3 TIRE PRESSURE MONITORING SYSTEM DESIGN

The system consists of a pressure sensor that is read by a microcontroller which converts the sensor reading into a pressure value before it is transmitted by a 433MHz transmitter. Two different low power pressure sensors have been tested one of which outputs an analog voltage reading between 0 to 295 mV depending upon the air pressure and the other outputs a series of digital pulses.

The entire system from the sensor to the transmitter is powered intermittently to read the pressure and transmit it. Unlike the conventional battery powered TPMS sensors, this power is harvested from the piezoceramic (PZT) elements mounted on the wheel as discussed previously. The AC output from the PZT element(s) is rectified and stored in a capacitor. When enough voltage has built up in the capacitor it is discharged and regulated down to 3.0V to meet the requirement of the electronic components. The system schematic is shown in Figure 6-5.  $\mu$

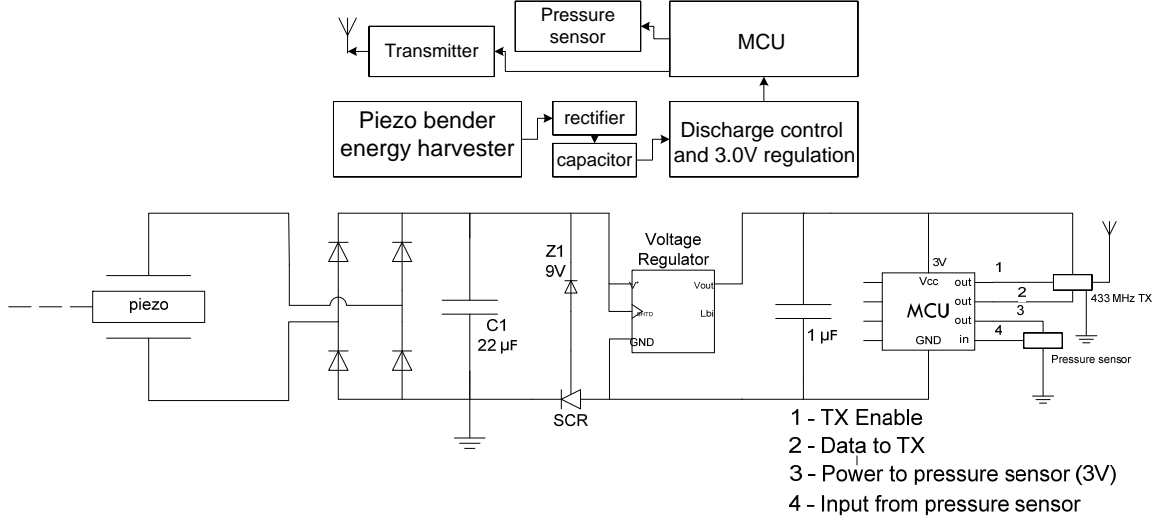


Figure 6-5: Schematic and circuit of the TPMS module

Capacitor discharging is controlled by a zener diode, Z1, and the silicon controlled rectifier (SCR) combination. When the storage capacitor, C1, voltage rises above 10V as determined by Z1, current passes through it into the gate of the SCR. The SCR gets triggered and allows the voltage regulator to turn on by connecting its ground to that of the capacitor. Current flows through the regulator which supplies 3 V to the microcontroller and the transmitter until C1 voltage drops down to 4 V at which point the regulator shuts down and the current consumptions reduces to 10  $\mu$ A, which is insufficient to keep the SCR triggered. Thus SCR turns off and the C1 voltage starts rising again from PZT excitation until it once again reaches 10 V and the cycle repeats itself. The idea is similar to the regulated discharge used by Kymissis [19] for his piezo powered shoe mounted RF tag. However, the circuit has been greatly simplified and uses minimal number of components reducing the quiescent current of the entire circuit as well as the circuit footprint.

3 V supply components have been used to eliminate the need of multiple voltage regulators. The transmitter and pressure sensor are controlled by the microcontroller allowing them to be turned on precisely when they are needed and turned off when not in use thus allowing efficient use of power. The microcontroller requires 1.1 mA while the

transmitter requires between 3.0 - 3.5 mA. The analog pressure sensor runs at 0.9 mA whereas the digital sensor requires a mere 10  $\mu$ A. The total current consumption with the analog sensor, microcontroller and the transmitter running simultaneously is around 5.5 mA. However, the transmitter doesn't need to be powered while the pressure sensor is being read and similarly the pressure sensor can be turned off while the data is being wireless transmitted. Thus with the pressure sensor and microcontroller running, the current consumption is about 2mA whereas the microcontroller and transmitter consume between 3.5 to 4.5 mA. Through this selective component powering approach, the consumption is reduced considerably allowing for a smaller storage capacitor to be used increasing the frequency of transmission.

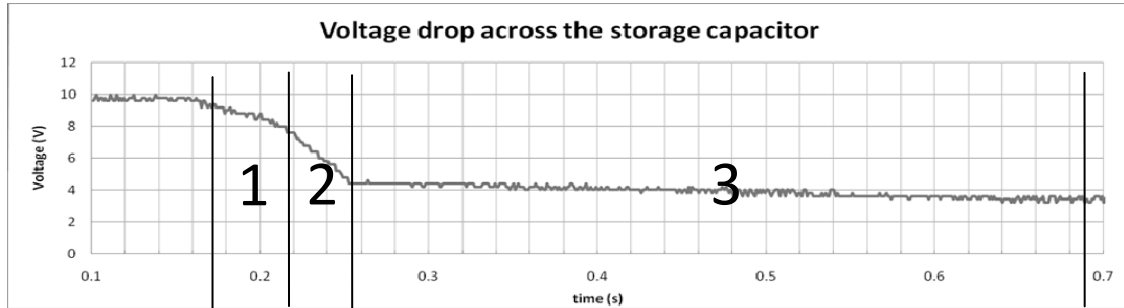


Figure 6-6: Voltage drop across the storage capacitor during different TPMS operation phases 1) Reading pressure from the sensor, 2) Wireless transmission of data and 3) Low power Sleep mode

Figure 6-6 shows voltage drop across the storage capacitor, C1, during the three different phases of TPMS operation: 1) Microcontroller acquiring pressure sensor data, 2) data being wireless transmitted to the onboard receiver, and 3) microcontroller in low power consumption mode. The rate of voltage drop is lower in the first phase than in the second phase due to the transmitter being off and only the pressure sensor and microcontroller operating in active mode. In phase 2, the microcontroller disables the pressure sensor while the transmitter is enabled to allow data transfer increasing power consumption resulting in a higher rate of voltage drop. In phase three, the transmitter is disabled and the microcontroller switches to a lower power sleep mode. In Figure 6-6, the C1 voltage does not rise again after phase 3 because the tire was brought to a stop and no power was being harvested from the PZT benders.

## 6.4 RESULTS

Sufficient power is generated by both PZT harvesters to intermittently supply the TPMS module. Since a capacitor is used to store charge overtime, power generated by PZT harvester per deformation does not need to be as high as the power consumed by TPMS module for each transmission.

Table 6-4**Error! Reference source not found.** shows the length of time in milliseconds for which various capacitors can support a 4mA~ load at regulated voltage of 3V. When the initial voltage of the capacitor is 0V, it takes 21 revolutions to charge a  $61\mu\text{F}$  capacitor up to 10V whereas the same capacitor requires 17 steps when the initial voltage is 3.5V. The voltage regulator stops the flow of current to the sensing and transmission circuit as the capacitor voltage drops to 3.5V and thus the capacitor starts recharging from that level.

Table 6-1: Time for which a 4.5mA load can be supported by various capacitances

Capacitance, C1 ( $\mu\text{F}$ )	# of Revolutions required to charge C1 from 0V to 10 V	# of Revolutions required to charge C1 from 3.5V to 10 V	C1 discharge time for a 4.5mA load (ms)
100	32	23	125
69	24	19	104
61	21	17	100
57	20	16	98

## 6.5 FREQUENCY OF OPERATION

Both of the PZT harvesters produce power at each revolution increasing the voltage of the storage capacitor in steps as can be seen in Figure 6-2. Higher the vehicle speed higher the RPM and more quickly voltage in the storage capacitor builds up to the 10V threshold. Thus the frequency of operation of the TPMS module depends upon the speed

of the vehicle allowing the module to transmit pressure information to the onboard receiver more frequently at higher speeds. This is important because dramatic pressure changes at higher speeds allow less reaction time for the driver to take preventative measures and thus timely information of tire pressure is vital. This is not possible with conventional pressure sensors that transmit pressure at a fixed frequency. Using a  $61 \mu\text{F}$  storage capacitor, transmission occurs every 2.5 seconds at 60 km/h and every 1.5 seconds at 100 km/h as shown in Figure 6-7.

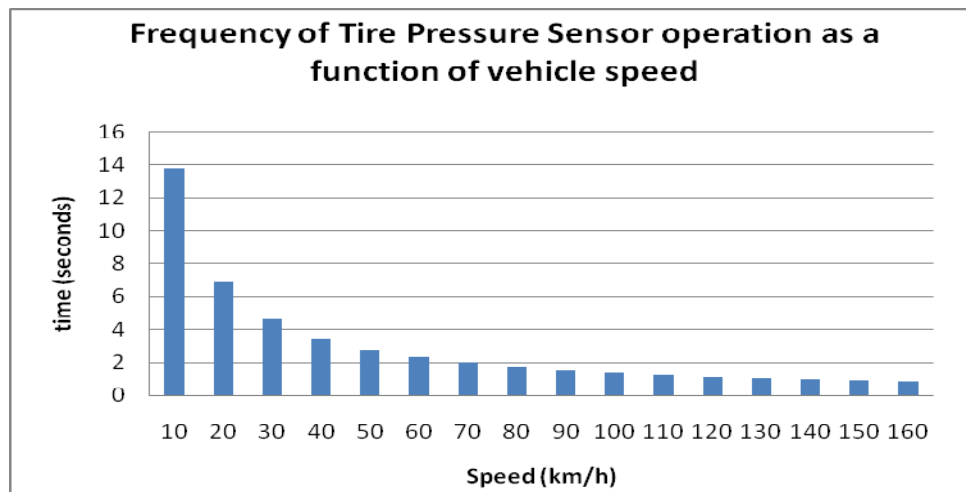


Figure 6-7: Frequency of pressure reading transmission at various vehicle speeds

### 6.5.1 *Elimination of Motion detection*

In conventional TPMS modules battery power conservation is a major problem, which not only requires use of expensive micropower electronic components but also requires rotation sensing circuitry to detect when the vehicle is in operation so that power to the module could be cut off when the vehicle is stationary. These approaches increase the complexity of the system, the number of components and the cost of the module. In contrast, PZT harvesters eliminate the need of motion sensing circuitry as there is no finite storage reservoir i.e. energy is harvested during vehicle operation and consumed once accumulated up to a certain level.

### 6.5.2 Power consumption

The current configuration of the TPMS module takes between 90-100 ms to sense and transmit pressure data. Hence the storage capacitor is appropriately sized to allow sufficient discharge time i.e. not too small that the transmission cannot complete and not too big that it reduces the frequency of the transmission. 61  $\mu\text{F}$  was experimentally found to be the most appropriate capacitance. Figure 6-8 shows the discharge characteristic of 4 different capacitors. Each of the capacitor drains sharply for 100 ms while the transmission is taking place before slowing down during sleep mode which only consumes 300  $\mu\text{A}$ . If the power consumption of TPMS is reduced, a lower size storage capacitor can be utilized increasing the frequency of operation.

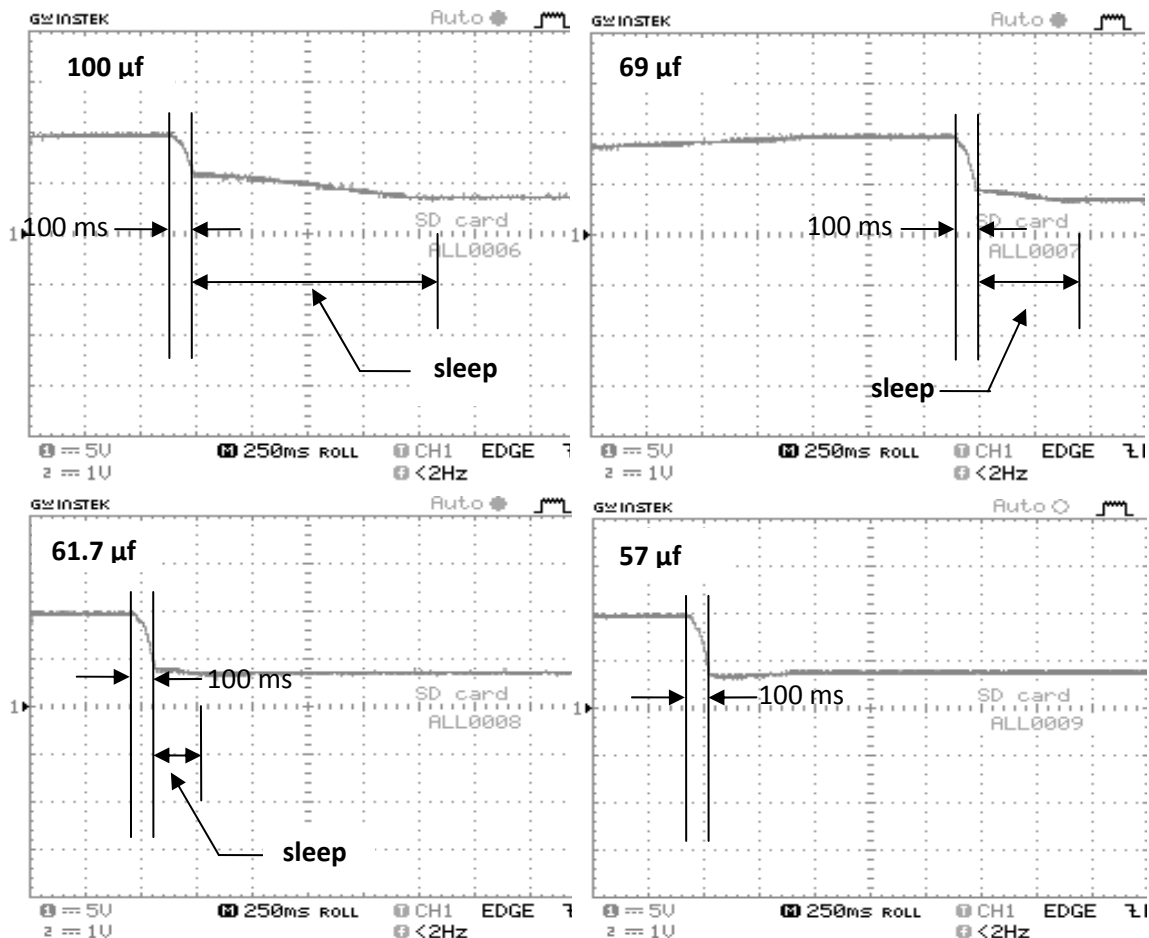


Figure 6-8: Discharge characteristics of various capacitors into a 4.5 mA load

Furthermore, the sleep mode does not provide any real benefit besides slowing down the rate of power consumption but has just been presented for the purpose of comparison. The  $61 \mu\text{F}$  capacitor just allows enough time for the transmission to complete after which the voltage of C1 drops down to the cut off limit of the voltage regulator and current ceases to flow. Hence the power to the microcontroller is cut off before it enters sleep mode.

### ***6.5.3 TPMS Module placement options***

Inner tire treadwall bonded PZT energy harvester requires that the TPMS module be mounted on the tire at the same site. This location on the tire is more favourable compared to the sidewalls where the PZT harvesters are more susceptible to damage due to extreme deformations during removal of the tire from the rim and installation thereof. Since the sensor only weight 25 grams tire balancing can be done in a regular manner without any added difficulties.

The bead-rim interface bonded PZT energy harvester provides more flexibility in the placement of TPMS module. If made thin enough, the entire sensor could be mounted at the interface. Another possibility is to keep the entire sensor on the rim by using the existing valve stem integrated pressure sensors. Such an arrangement requires minimal change to the existing design of battery powered TPMS modules i.e. replacement of the battery, which is the largest component of the sensor by size, with PZT energy harvesters.

Figure 6-9 (a) shows the TPMS module built for test purposes. It consists of the entire circuit on a small chip that can be easily mounted inside the wheel for testing. The transmitter and antenna can be seen on the left with the microcontroller and pressure sensor in the middle. Rectifier, storage capacitor and voltage regulation circuitry occupies the upper right portion of the board. Receiving side consists of a matching receiver connected to a microcontroller as seen in Figure 6-9 (b).

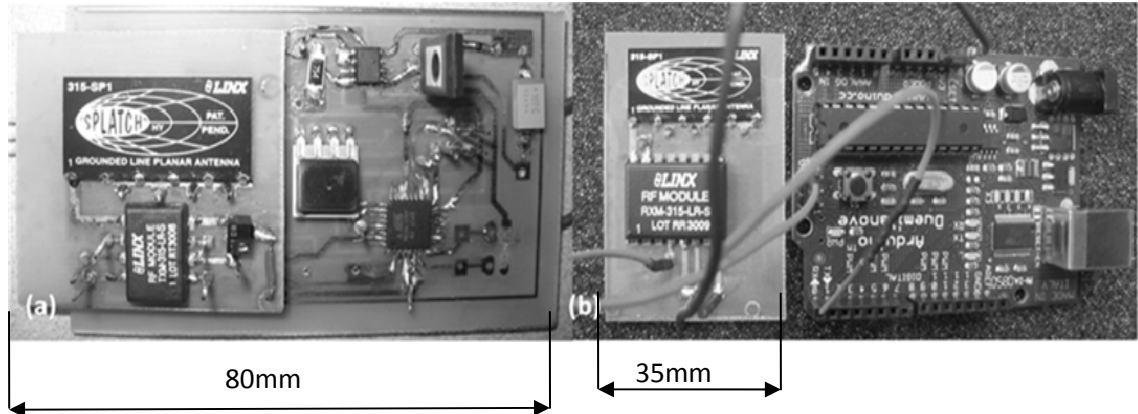


Figure 6-9: (a) TPMS module built for testing and (b) receiving unit

## *Chapter 7: PIEZOELECTRIC POWER GENERATION FOR SENSOR APPLICATIONS: DESIGN OF A PIEZO-POWERED WIRELESS VEHICLE SPEED SENSOR*

### **7.1 INTRODUCTION**

Knowledge of the vehicle speeds requires the measurement of the rotational speed of one of the driveline components usually in the transmission using a Hall Effect or magnetic sensor [4]. This method is applicable in the majority of conventional gasoline vehicles, electric vehicles (EVs) and Plug-In Hybrid Electric Vehicles (PHEVs). However, EVs and PHEVs that use Hub motors and near-wheel mounted motors make incorporation of such sensors difficult.

A novel RPM sensor is presented that is mounted within the tire in a fashion similar to the energy harvesting Tire Pressure Monitoring Sensors (TPMSs) [38]. The sensor makes use of PZT bender to sense the tire rotational speed as well as generate power to charge the battery [39].

### **7.2 VEHICLE SPEED SENSING**

A PZT bender element is glued to the tire as shown in Figure 7-1. When the element is deformed, it generates an AC sinusoidal voltage curve. Connecting the piezo element in parallel with a Zener diode and diode allows the current to flow only in one direction when the voltage increases beyond 2V as determined by the two diodes. Furthermore, the diodes keep the voltage level steady at 2V creating a switch type circuit that when interfaced with a MCU is read as a digital signal switching between high and low. The MCU calculates the time interval between the voltage peaks in order to determine the RPM which is transmitted via a wireless transmitter (TX). The piezoelectric sensing element interface circuit is shown in Figure 7-2.

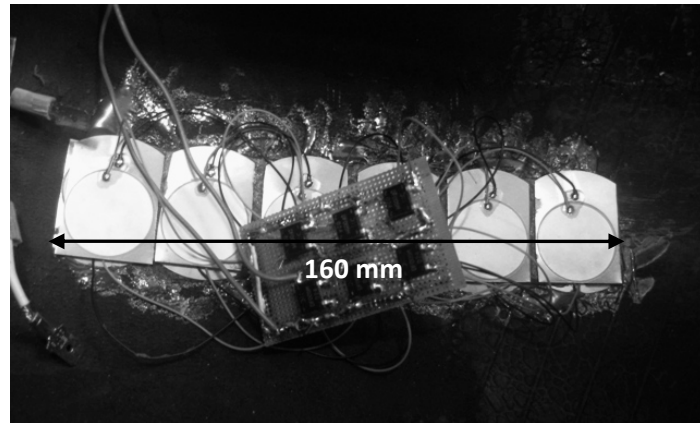


Figure 7-1: PZT bender elements attached to the inner surface of a tire. Rectifiers can be seen above the elements

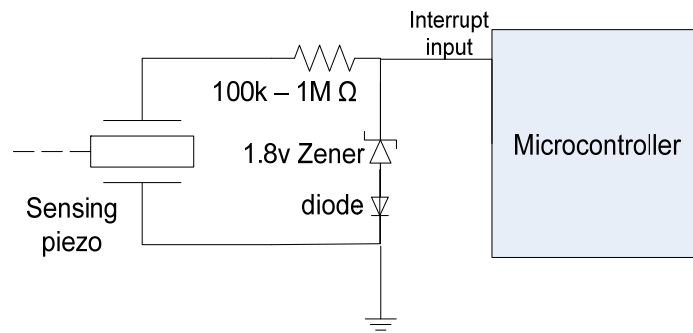


Figure 7-2: Piezo sensing circuit used for RPM measurements

Figure 7-3 shows the voltage response from the piezoelectric element connected to a digital input of the MCU allowing it to be read as high when deformed and low when relaxed. Attaching the sensing circuitry to the interrupt input of the MCU allows the controller to detect motion of the vehicle and put itself to sleep when the vehicle is stationary.

The MCU counts the duration between pulses to determine the time required for 1 RPM - PZT element is bent at the start/end of each rotation. Then the speed is calculated as in Eq. 7-1:

$$\text{Speed} = \text{Circumference of the tire} / \text{time duration} \quad \dots(7-1)$$

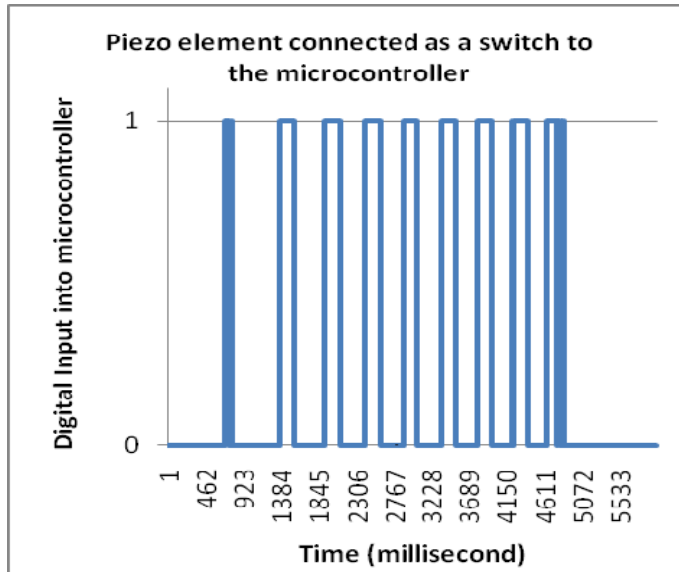


Figure 7-3: Output of the sensing circuitry as read by the controller

### 7.3 POWER GENERATION

A two layer PZT stack comprising of 12 circular bender elements is used for this purpose as shown in Figure 7-1. It measures 6 inches x 1.5 inches and is glued to the tire in a manner that allows maximum flexibility. The rise in  $22 \mu\text{F}$  and  $47 \mu\text{F}$  capacitor is shown in Figure 7-4. The capacitor voltage rises once per rotation of the wheel due to the deformation of the PZT elements. As evident, it takes 3 rotations to raise the  $22 \mu\text{F}$  capacitor voltage to 10V while a  $47 \mu\text{F}$  capacitor requires 7 rotations to reach the same threshold. The difference in charging time of the two capacitors is due to the different rotational speeds used for charging. The time required to charge the capacitor is a function of the wheel RPM i.e. the faster the tire rotates the faster the capacitor charges. Thus more power is generated at higher RPM.

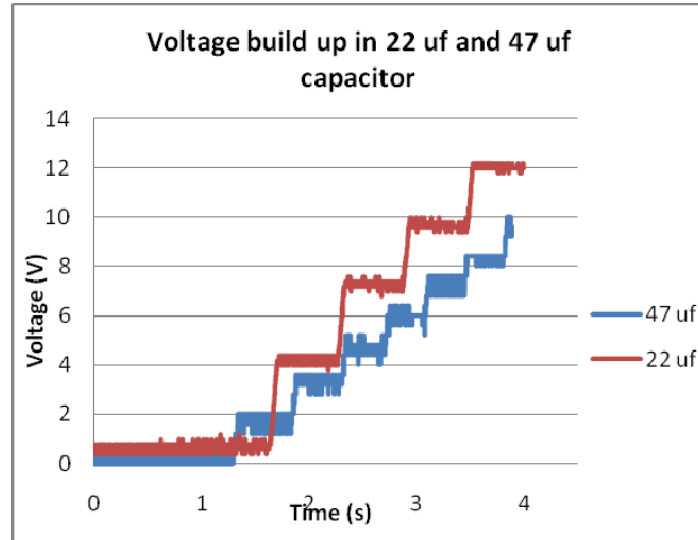


Figure 7-4: Voltage buildup in two different capacitors from piezo charging

Power output from PZT harvesters was tested by using various resistive loads and measuring the average voltage across them. A maximum of 8.3 mW is delivered to a 12 kΩ load as shown in Figure 7-5.

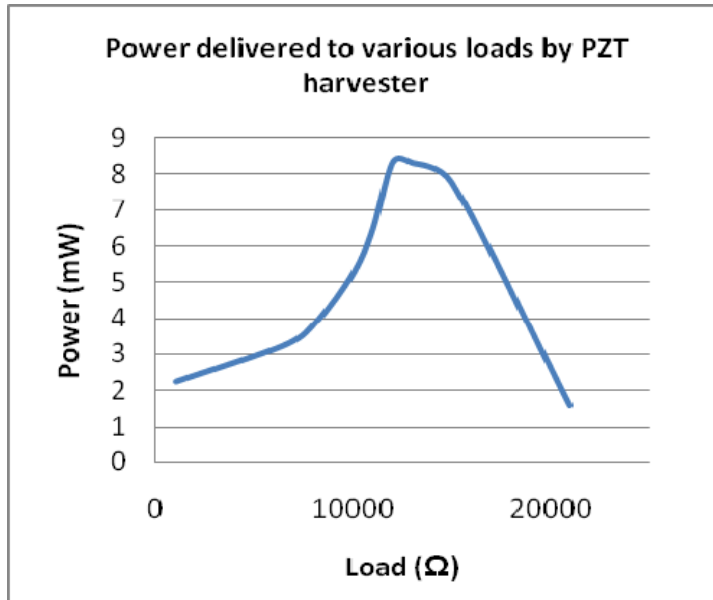


Figure 7-5: Power delivered to various loads by PZT harvester

## 7.4 SYSTEM PERFORMANCE

For the purpose of achieving an adequate battery life, the relationship in Eq. 7-2 must hold true:

$$\text{Power Generation} \geq \text{Power Consumption} \quad \dots(7-2)$$

If power harvested from the tire is not enough for maintaining the battery level then it will slowly discharge ultimately draining out completely rendering the sensor nonfunctional.

### 7.4.1 Power Consumption

A moderately low power MCU, atmega328P, is used to calculate RPM and transmit the signal via a 315 MHz lower power TX. Running at 1 MHz, the MCU uses 0.5 mA while operating in normal mode at a voltage of 1.8V: power consumption of 0.9 mW. The TX is configured to use 1.7 mA at 3.0V: power consumption of 5.1 mW. However, the transmitter is only powered when data needs to be transmitted and remains off at other times consuming 0.01  $\mu$ A. To conserve power, the RPM reading is only transmitted once or twice every second depending upon the vehicle speed. It takes 50ms to transmit the RPM reading for which the TX needs to be powered, total of 100 ms for two transmissions. The average power consumption per second is thus calculated as in Eq. 7-3:

$$\text{Power} = 0.9 \times 1 + 5.4 \times 0.1 = 1.41 \text{ mW} \quad \dots(7-3)$$

The above calculation is based on the fact that MCU operates continuously while the transmitter is only powered for 0.1 seconds.

### 7.4.2 Power Reservoir – Battery

The battery serves as the primary power source to achieve stable operation of the wireless RPM sensor while the PZT energy harvesting patch is used to recharge the battery preventing it from draining down to a level inadequate for the sensor operation. Based on

the power calculations above, the average current drawn from the battery is 0.47 mA at a regulated voltage of 3V. Two batteries were tested for use in the sensor: a 3V 45 mAh coin cell and a 3V 11mAh coin cell providing a maximum theoretical sensor life of 95.74 hours and 23.4 hours respectively with no recharging.

#### 7.4.3 Battery Charging

An SCR based circuit [38][39] is used to discharge the capacitor once it reaches 10V. A linear voltage regulator, MAX666, provides a steady output voltage of 3.1V used for direct charging of Li-Ion battery. The regulator discharges the capacitor down to 4.0V from where it starts charging again to a level of 10V. Since the battery is charged by draining the 22  $\mu$ F capacitor, the charging current is supplied to the battery only intermittently and cutoff while the the capacitor is still charging up to 10V. The charging circuit is shown in Figure 7-6.

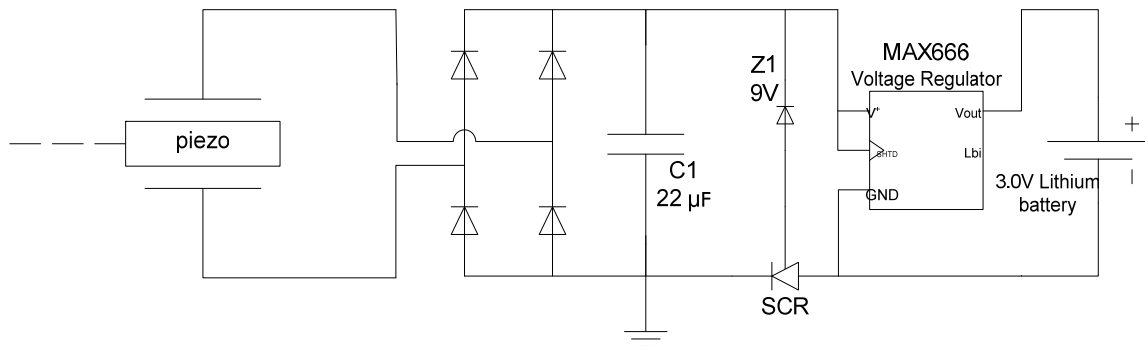


Figure 7-6: PZT harvester battery charging circuit

Since only constant volatge (CV) charging is used, the current drawn by the battery is a function of its resistance and decreases with the increasing battery voltage. When the battery is discharged through the sensor with the TX transmitting 10 times every 3 seconds i.e. one and half times more frequently than the intended rate of transmission, the battery lasts for 360 minutes from a starting voltage of 2.94V draining down to 2.2V, Figure 7-7. The same battery when charged from 2.3V upto 3.02V with a charging voltage of 3.1V requires just under 385 minutes to charge as shown in Figure 7-8. Thus at lower transmission frequency or higher vehicle speed, sufficient power would be produce

to charge the battery faster than it depletes.

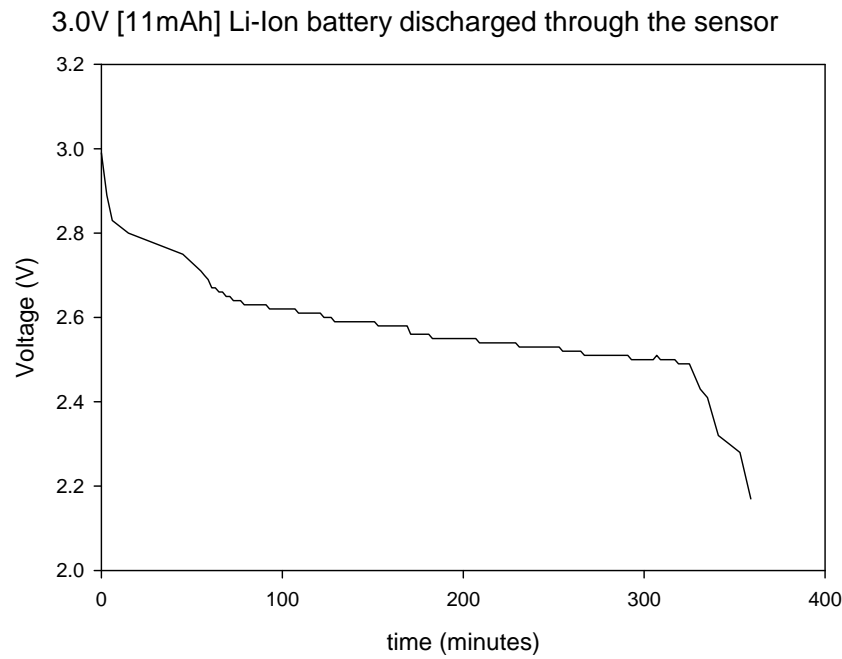


Figure 7-7: 3.0V [11 mAh] battery discharging test

3.0V [11mAh] battery charging from PZT harvester at 30 km/h

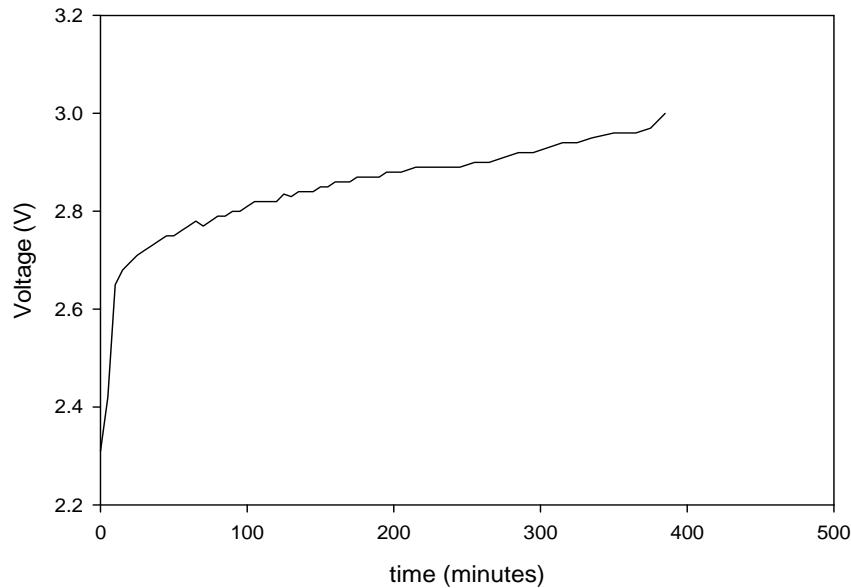


Figure 7-8: 3.0V [11 mAh] battery charging tests

Even though Constant Current (CC) charging is not used on the Li-Ion rechargeable batteries, it does not create any issues since the current produced by PZT benders is limited to only a few millamps. Moreover, since current drawn by the battery is a function of the battery voltage, it is significantly low at high battery voltages due to small voltage difference between the charging voltage and battery voltage by Eq. 7-4:

$$I = V_s / R_b = (V_s - V_b) / R_b \quad \dots(7-4)$$

Where  $V_s$  is the constant supply voltage of 3.2V,  $V_b$  is the battery voltage at a particular point in time and  $R_b$  is the batteries internal resistance which is assumed to be constant. It can be clearly seen that as the battery charges to a higher voltage the current draw decreases. Since the battery management system of the RPM sensor charges battery as soon as the voltage drops below 2.6, the current draw remains low and damage to the battery is minimized.

Low speed short duration power harvesting tests were conducted on tire dynamometer discussed in Chapter 2. Due to difficulties associated with running this dynamometer for long periods of time required for battery charging tests, simulated charging was conducted using a function generator with pulsed output. Based on Figure 7-4, it takes 2 rotations to charge the 22  $\mu\text{F}$  capacitor from 4V to 10V. At 30 km/h, a P185/65R14 tire takes 0.223s to complete one rotation. Thus the capacitor takes 0.45s to charge to 10V before it is drained by the regulator i.e. 2.13 charging cycles are completed every second. By using an RC circuit with the function generator the 22  $\mu\text{F}$  capacitor was charged to 10V every 0.45s and allowed to discharge through the regulator into the battery. Figure 7-9 shows the similarity between capacitor charged using PZT harvester bonded to the tire spinning at 50 RPM on the dynamometer and the capacitor charged using a function generator through a resistance,  $R$ . The time constant,  $T=RC$ , which dictates the charging time of the capacitor can be controlled by changing  $R$  simulating various capacitor charging frequencies.

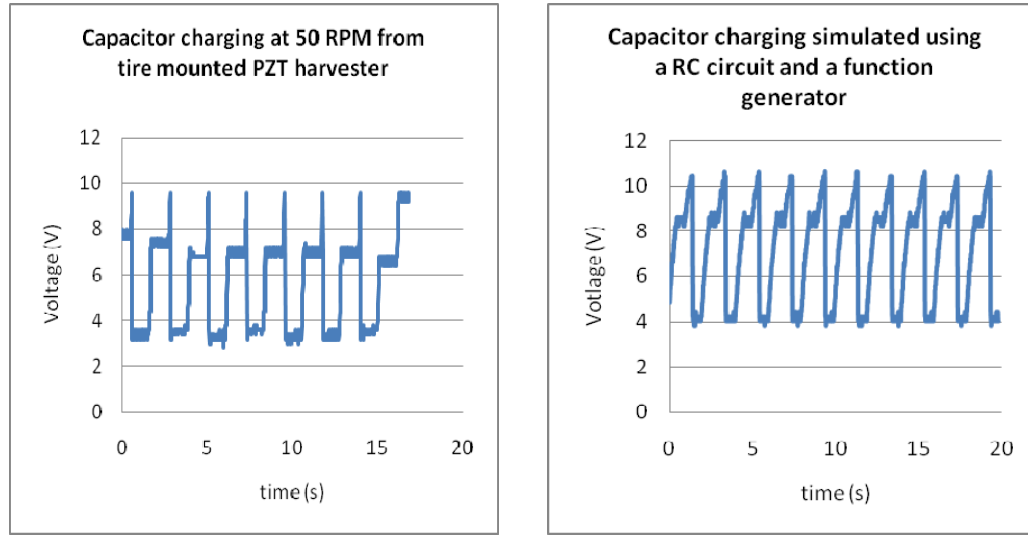


Figure 7-9: Similarities between capacitor charging using PZT harvester and function generator

Table 7-1 summarizes charging frequencies of a  $22 \mu\text{F}$  capacitor at some common vehicle speed with a P185/65R14 tire. The capacitor is charged more frequently at higher speeds resulting in charge being dumped into the battery more often. This also allows more frequent transmission of RPM data while still maintaining battery voltage.

Table 7-1: Capacitor charging frequencies

Speed (km/h)	RPM	<b>22 <math>\mu\text{F}</math> Capacitor charging frequency (Hz)</b>
10	87.0	0.73
30	261.1	2.18
50	435.1	3.63
60	522.2	4.35
100	870.3	7.25

#### 7.4.4 Power Conservation

To conserve battery power and elongate sensor life, it is vital for the sensor to be able to detect vehicle idling periods and turn itself off preventing battery drainage. The MCU has

been programmed to cut power to itself and the TX circuitry isolating the battery when it does not detect a voltage peak from the RPM sensing PZT element for 2 minutes. This is achievable only because the PZT elements do not produce any charge when the tire is not rotating allowing the differentiation between vehicle operation and idling periods. However, special circuitry is needed to cutoff power to various components of the sensor and will be discussed later.

## 7.5 VEHICLE SPEED SENSOR SYSTEM

A complete system schematic is shown in Figure 7-10. As stated before, PZT benders produce voltage peaks which are rectified and stored in a capacitor. MAX666 linear voltage regulator, R1, is configured to deliver an output of 3.3V. A normally open single pole double throw (SPDT) electronically switch, SW1, is used to channel the voltage output either to the battery or to the microcontroller. This switch as well as SW2 use battery as their power source and are controlled by the MCU. In the normally open position, SW1 channels the 3.3V regulated output of R1 to the microcontroller whereas SW2 supplies the microcontroller from SW1. The advantage of this configuration is its ability to wake up the microcontroller as soon as the vehicle starts to move after a long break. The rotation of tire deforms PZT elements that charge the store capacitor, C1, and start R1. As R1 conducts, the microcontroller is supplied via normally open SW1 and SW2 and the 1.8V buck regulator, R2. Once the microcontroller wakes up, it closes the two SPDT switches, SW1 and SW2, and operates on battery power from there onwards. Closing SW1 channels the R1 output to the battery thus charging it. Thus SW1 allows the PZT harvested energy to be used for MCU operation or battery charging. SW2 allows the microcontroller to choose its power source: Li-Ion battery or PZT. A Linx Technologies LR series 433 MHz wireless transmitter (TX) is used to transmit vehicle speed readings to a matching onboard receiver. TX is always powered from the battery but can be disabled by the microcontroller by a control signal allowing it to be powered off when not needed.

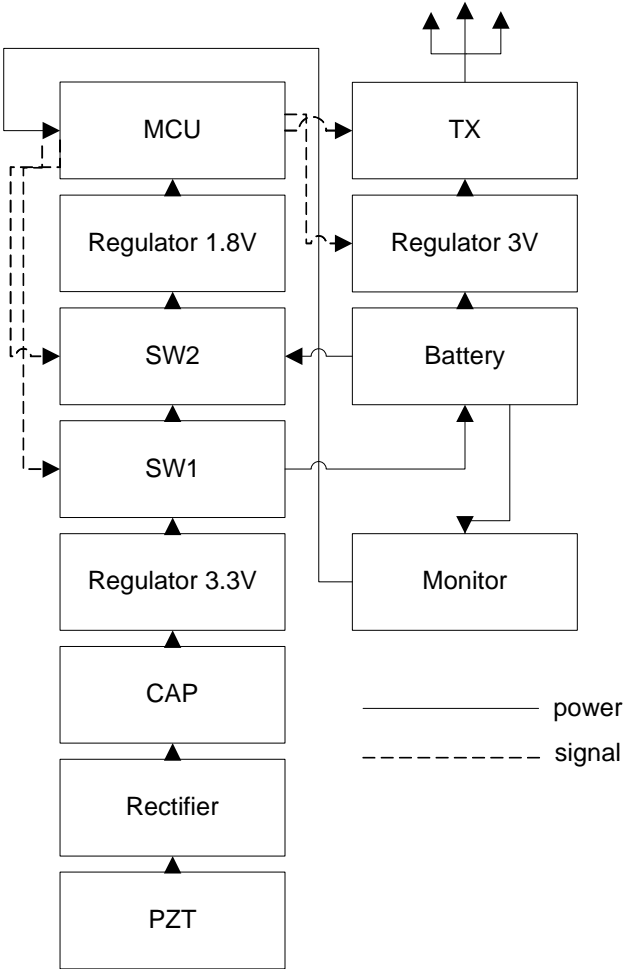


Figure 7-10: Vehicle speed sensor schematic

A battery monitor keeps track of the battery voltage and communicates to the microcontroller to allow it to control battery charging.

### 7.5.1 *Sleeping*

When no voltage pulse is detected from PZT bender element for a period of 2 minutes, the MCU initiates a sleeping sequence. It ensures that R3 that powers TX is disabled first followed by opening SW1 switch directing R3 output to SW2. Then it disables the battery monitor and finally cuts off the power to itself by opening SW2. The sequence is shown in the Figure 7-11.

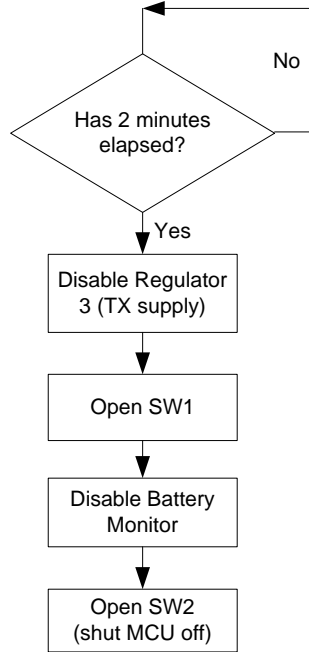


Figure 7-11: Sleeping sequence

### 7.5.2 *Wakeup circuit*

The system has the ability to wake itself up thanks to the voltage generated by PZT benders. After a long pause, once the vehicle starts moving the PZT benders generate charge that is stored in the storage capacitor, C1. A  $22 \mu\text{F}$  capacitor requires two revolutions to charge to 10V after which R1 conducts. The output of R1 passes through SW1 to SW2 and from there to the MCU. MCU powers up and closes SW1 and SW2 to run on the battery, which is a more reliable power source at low speeds. There onwards, the sensor operates normally as described previously. The wake up sequence is shown in Figure 7-12.

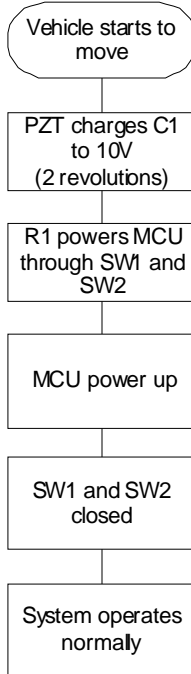


Figure 7-12: Wakeup sequence

### 7.5.3 *Battery-Free operation*

With the current PZT harvesting patch enough power is generated at speeds above 50 km/h to be able to sustain MCU and TX operation. The MCU can be programmed to close SW1 and SW2 above this speed to use PZT power and conserve battery. Even with a different harvesting patch, appropriate speed levels can be determined above which battery power is not needed. This approach increases battery life as well as the overall life of the sensor.

## 7.6 MULTIFUNCTIONALITY

In the Vehicle speed sensor (VSS) the use of PZT elements thus serves three purposes: 1) Power generation, 2) RPM sensing and 3) Vehicle motion detection eliminating the need of a separate motion sensing circuit as required in conventional battery powered TPMSs.

## *Chapter 8: ELECTRONICS DIFFERENTIAL FOR PHEV*

An innovative conversion of a commercially available Dune Buggy into a plug-in dual fuel (Gasoline/Hydrogen) extended range electric vehicle (EREV) prototype makes use of two near-wheel propulsion assemblies with one motor mounted to each of the rear wheels of the vehicle [40]. The drive train design excludes a conventional mechanical differential to minimize the overall weight of the vehicle, reduce the number of components contributing to the system inefficiency, and to simplify the driveline. Instead, in order to allow proper turning and cornering, minimize tire wear and reduce the probability of structural damage an Electronic Differential System (EDS) had to be developed.

Since the EREV is rear wheel driven, the front wheels are followers and the rear wheels' rotational speed must be differentiated. Moreover, due to the near-wheel design of the driveline where each of the rear wheels have their own motors and gearbox attached directly to the wheel without a central axes, a conventional differential is impossible to implant. However, the electrical driveline does provide for an opportunity to utilize an electronic differential whereby the rotational speeds of the two motors can be controlled individually to achieve the differential affect.

### **8.1 BACKGROUND INFORMATION**

#### ***8.1.1 Differential***

A differential is a specialized gearbox with one input shaft and two independent output shafts. The independence of the two outputs is an important characteristic as it allows to bodies connected to it to turn at different rates, a property extremely desirable in road vehicles. During a turn, wheels on left and right side of the vehicle follow paths of different radius and must cover different distances. If the wheels are connected together by a rigid axle, they are forced to turn together resulting in slippage and improper turning

leading to increased wear of the tires and poor turning/cornering characteristics. In order to allow the wheels to turn at different rates they must be independent of each other while still connected to the main shaft drive shaft coming from the transmission. The differential sits between the two wheels and allows the outer wheel to spin faster than the inner wheel as required during turning [41].

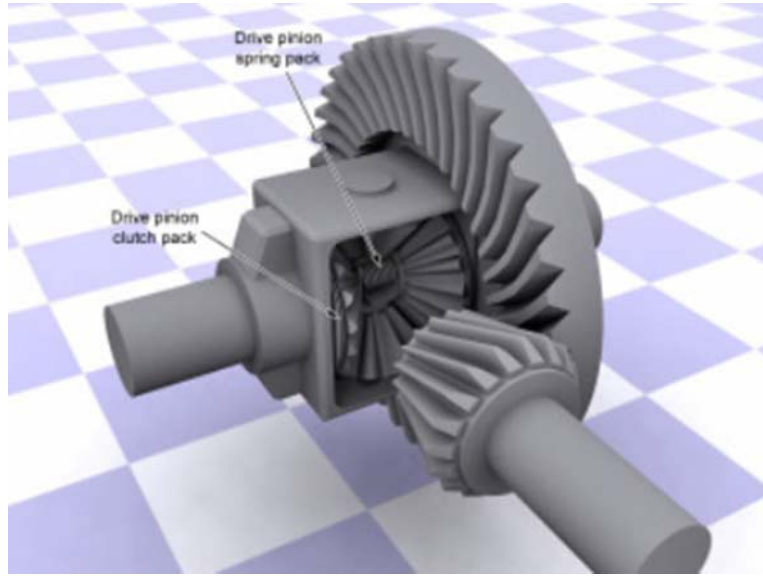


Figure 8-1: A Mechanical differential

Figure 8-1 shows a picture of the differential unit commonly used in commercial gasoline powered vehicles [42]. Normally, such mechanical differentials require minimal electronics for control unless the vehicle features active braking and traction control in which case additional torque/slip limiters are used.

### ***8.1.2 Differential for Electric Vehicles***

Besides commercial vehicles utilizing Internal Combustion Engine (ICE) many electrical vehicles (EVs), Hybrid Electric Vehicles (HEVs) and Plug-in hybrid Electric Vehicles (PHEVs) utilize a mechanical different similar to the one shown above. They are required when the ICE is replaced with a single motor that drives both of the driven wheels. However, EVs and PHEVs that make use of separate motors for each of the driving wheel as is the case with the Plug-in Hybrid Extended Range Electric Vehicle (EREV) at

UOIT can no longer utilize a mechanical differential as both the driving wheels have independent axles and power sources. In such cases, the differential effect must be achieved electronically using sensors to monitor the rotational speed (RPM) of each wheel, the steering angle and the throttle/brake position. A microcontroller is used to continuously monitor the state of the three user inputs (steering, brake and throttle) as well as the feedback data from the two wheels and determine the appropriate adjustments necessary for improved handling as determined by the designer.

### 8.1.3 Theoretical background and principal of operation

During a turn, the front inner and outer turning wheels turn at different angles to enable the vehicle to turn with minimum slippage. The rear inner and outer wheels turn about circles of different radius given by  $R - d/2$  and  $R + d/2$  respectively, where  $R$  is turning radius measured from the center of the vehicle – Figure 8-2. The difference in turning radii requires that the inner and outer rear wheel rotate at different speeds denoted by  $\omega_{in}$  and  $\omega_{out}$ . In conventional vehicles, this differential in rotational speed is achieved with the use of a differential on the driving wheels i.e. front axle for front wheel drive and rear axle for rear wheel drive vehicles. The angle ( $\delta$ ) each of the two turning wheels make relative to the direction of motion is also different i.e. the inner angle ( $\delta_{in}$ ) is greater than the outer angle ( $\delta_{out}$ ) as shown below [43].

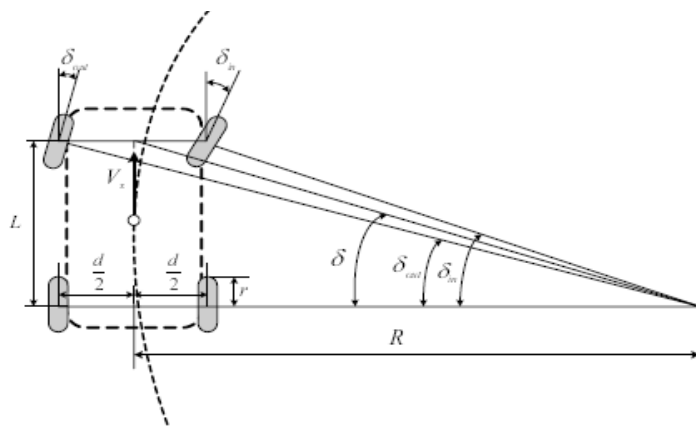


Figure 8-2: Geometry of Ackermann angle during a turn. The difference of inner and outer wheel angles is noticeable.

The differential logic is based on the Ackermann equations [43] for differential inner and outer wheel speed, given below:

$$\omega_{in} = \frac{V}{2\pi r} \left( 1 - \frac{d \tan(\delta)}{2L} \right) \quad \dots (8-1)$$

$$\omega_{out} = \frac{V}{2\pi r} \left( 1 + \frac{d \tan(\delta)}{2L} \right) \quad \dots (8-2)$$

Where V is the linear velocity of the buggy, r is the radius of the tire, d is half the distance between the inner and outer tire, L (called the wheel base) is the distance between front and rear tire  $\delta$  is the average or the Ackermann angle of the inner and outer front wheels denoted by  $\delta_{in}$  and  $\delta_{out}$  [43]:

$$\delta = \frac{\delta_{in} + \delta_{out}}{2} \quad \dots (8-3)$$

In equations (8-1) and (8-2), r,d and L are constants based on the chassis or the vehicle in question. The only two variables are the vehicle velocity (V) and the steering angle ( $\delta$ ). V is determined by either monitoring the throttle position or the RPM of each wheel while the steering angle can be measured by using a angular position sensor attached to the steering wheel [43].

#### **8.1.4 Simplification of the Ackermann equation**

The use of equation (8-1) and (8-2) would require the knowledge of the vehicle's current velocity. To eliminate the need to have the knowledge of the current velocity, the equations (8-1) could be divided by (8-2) to get a ratio. Thus:

$$\omega_{in} / \omega_{out} = \left( \frac{2L - d \tan(\delta)}{2L + d \tan(\delta)} \right) \quad \dots (8-4)$$

$$\text{Let } x = \left( \frac{2L - d \tan(\delta)}{2L + d \tan(\delta)} \right) \quad \dots (8-5)$$

Then combining (8-4) and (8-5)

$$\omega_{in} / \omega_{out} = x \quad \dots(8-6)$$

$$\text{Or } \omega_{in} = x\omega_{out} \quad \dots(8-7)$$

Equations (8-6) and (8-7) are only dependant upon the Ackermann angle which is easily acquirable by monitoring the steering status.

If a tire were to be placed at the midpoint between the two rear wheels, its rotational velocity would be just the average of the inner and outer wheel velocity i.e.

$$\omega = \frac{\omega_{in} + \omega_{out}}{2} \quad \dots(8-8)$$

Where  $\omega$  is the just the vehicles actual velocity. If the rotational speed  $\omega$ ,  $\omega_{in}$  and  $\omega_{out}$  are taken in relative terms as factors of the vehicle heading velocity rather absolute then  $\omega = 1$  always. Moreover,  $\omega_{in}$  is always less than  $\omega$  or 1 and  $\omega_{out}$  is always greater than  $\omega$ . Then equation (8-8) could be combined with (8-7) and rewritten as:

$$1 = \frac{\omega_{in} + \omega_{out}}{2}$$

$$1 = \frac{x\omega_{out} + \omega_{out}}{2}$$

$$\omega_{out} = \frac{2}{(x+1)} \text{ or } \omega_{out} = \frac{2\omega}{(x+1)} \quad \dots(8-9)$$

Equation (8-7) and (8-9) can easily be utilized to calculate the factored speed of the inner and outer wheels respectively. The table below shows how the factors  $\omega_{out}$  and  $\omega_{in}$  change with respect to steering angle

Table 8-1: Variation in inner and outer wheel angle with Ackermann

Speed (factor)	Calculated using equation (1) and (2)				Calculated using equations (7) and (8)				
	Ackerman angle ( $\delta$ )	$\omega_{in}$	$\omega_{out}$	Difference	$\omega$	x	Differential amplitude (ad)	$\omega_{in}$ $[(2^*w)/(x+1)]$	$\omega_{out}$ (wi * x)
1	0.000	1.000	1.000	0.000	1	1.000			
1	2.763	0.992	1.008	0.016	1	1.016	0.008	0.992	1.008
1	5.525	0.984	1.016	0.033	1	1.033	0.017	0.984	1.016
1	8.288	0.975	1.025	0.049	1	1.051	0.025	0.975	1.025
1	11.050	0.967	1.033	0.066	1	1.068	0.034	0.967	1.033
1	13.813	0.958	1.042	0.083	1	1.087	0.043	0.958	1.042
1	16.575	0.950	1.050	0.101	1	1.106	0.053	0.950	1.050
1	19.338	0.941	1.059	0.119	1	1.126	0.063	0.941	1.059
1	22.100	0.931	1.069	0.137	1	1.148	0.074	0.931	1.069

The ‘Differential Amplitude’ in the above table is the difference between  $\omega_{in}$  and  $\omega$  or  $\omega$  and  $\omega_{out}$ .

The table below compares the ratio  $\omega_{in}/\omega_{out}$  for sample speed of 100 km/h and that obtained using the speed factor.

Table 8-2: Sample RPM values for 100 km/h

Speed (km/h)	Calculated using equations (1) and (2) for V = 100 km/h and r=0.127 m					speed factor	Calculated using (7) and (9) with speed factor of 1			
	Ackerman angle ( $\delta$ )	$\omega_{in}$	$\omega_{out}$	$\omega_{in}/\omega_{out}$	$\omega$		x	$\omega_{in}$ $[(2^*w)/(x+1)]$	$\omega_{out}$ (wi * x)	$\omega_{in}/\omega_{out}$
100	0.000	357.910	357.910	<b>1.000</b>	357.9	1	1.000			
100	2.763	354.988	360.832	<b>0.984</b>	357.9	1	1.016	0.992	1.008	<b>0.984</b>
100	5.525	352.052	363.768	<b>0.968</b>	357.9	1	1.033	0.984	1.016	<b>0.968</b>
100	8.288	349.088	366.731	<b>0.952</b>	357.9	1	1.051	0.975	1.025	<b>0.952</b>
100	11.050	346.083	369.737	<b>0.936</b>	357.9	1	1.068	0.967	1.033	<b>0.936</b>
100	13.813	343.021	372.799	<b>0.920</b>	357.9	1	1.087	0.958	1.042	<b>0.920</b>
100	16.575	339.885	375.935	<b>0.904</b>	357.9	1	1.106	0.950	1.050	<b>0.904</b>
100	19.338	336.657	379.162	<b>0.888</b>	357.9	1	1.126	0.941	1.059	<b>0.888</b>
100	22.100	333.319	382.501	<b>0.871</b>	357.9	1	1.148	0.931	1.069	<b>0.871</b>

### 8.1.5 PID Controller

It is naïve to assume that the speed of the wheel will be exactly related to the voltage signal supplied by the microcontroller to the motor controller. It is because uncontrollable variables such as weight on the vehicle, the air pressure inside the tire, the battery pack voltage and the internal resistance of the motor and gearbox because of poor lubrication are factors that can affect the response of the motor to the applied voltage. For this reason, a feedback control loop similar to one shown in Figure 8-3 must be used to monitor the rotational speed of the motor-wheel combination, compare it with the reference speed and apply appropriate correction all within a short period of time [44].

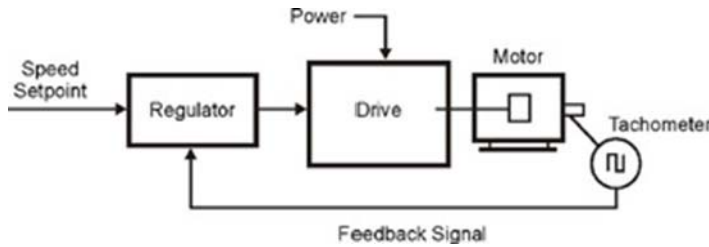


Figure 8-3: Closed loop control logic with Feedback for motor control

Proportional Integral Derivative (PID) control logic allows adequate control of many industrial and motor control processes [45]. The basic form of a PID controller is shown below in Eq. 8-10 [45]. The error signal,  $e(t)$ , given in Eq. 8-11 is used to develop the proportional, integral and derivative terms which are then summed together.  $U(t)$  becomes the input to be sent to the device being controlled; a DC motor in this case. The three constants:  $K_p$ ,  $T_i$ , and  $T_d$  are experimentally chosen to achieve the best system response through a process known as tuning.

$$u(t) = K_p \left[ e(t) + \frac{1}{T_i} \int_0^t e(\tau) d\tau + T_d \frac{de(t)}{dt} \right] \quad \dots(8-10)$$

$$e(t) = r(t) - y(t) \quad \dots(8-11)$$

In case of controlling the speed of a motor, the error is the difference between the reference speed of the motor and its actual speed.

Figure 8-4 shows how the performance of the PID controller varies with the individual change in the three constants. A  $K_p$  value of 1 gives the fastest response time but a high overshoot while higher values of  $T_i$  and  $T_d$  provide better damping [45].

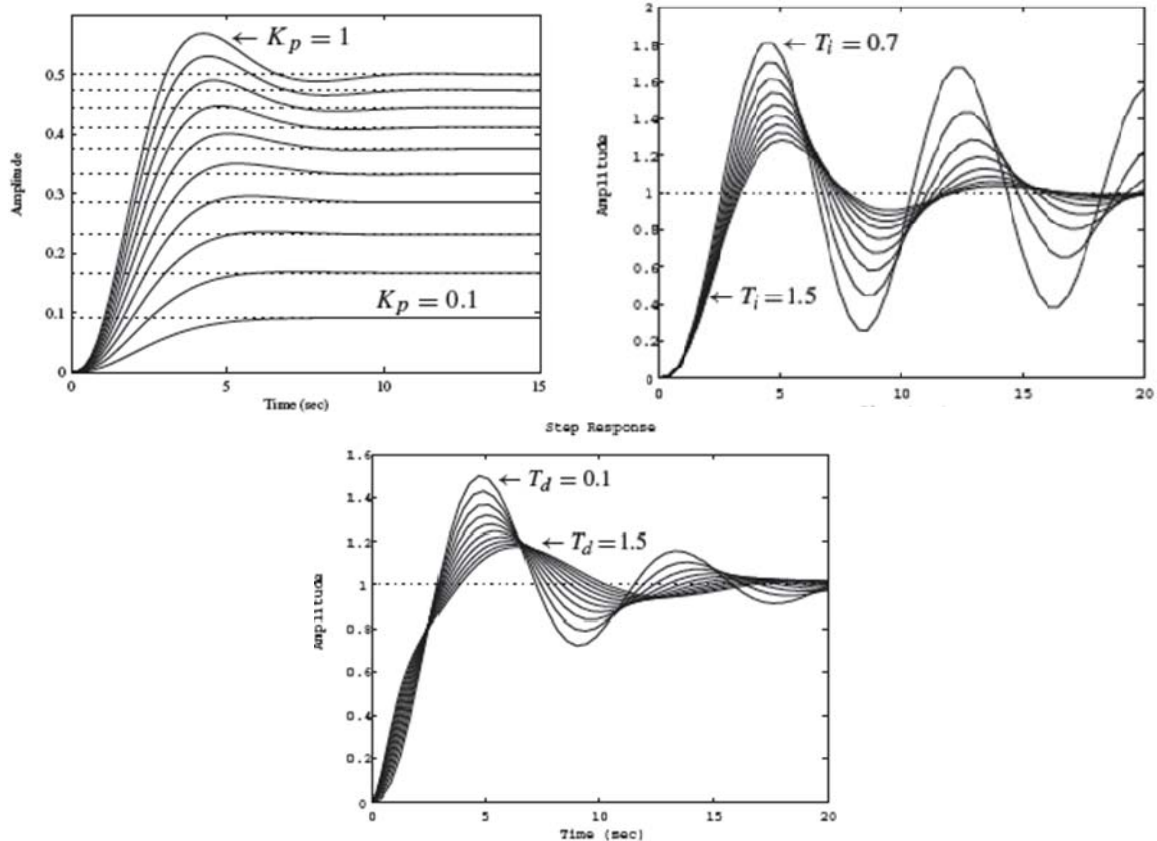


Figure 8-4: Affect of Proportional, Differential and Integral constants on PID controller.

## 8.2 HARDWARE

### 8.2.1 Speed control of Motors

The two DC motors are controlled by their own PWM motor controller. The controller accepts two forms of inputs; a 0-5KΩ and a 0-5V throttle to allow controlling the speed of the motor. The 0-5V range controls the input to the battery from 0 to the maximum of

the battery pack. Dune buggy has a 48V battery pack designed to match the specifications of the DC motors.

The brief description of all the contributing and required elements of the differential system is presented below:

### **8.2.2 DC Motors**

Two Mars Electric Etek Permanent magnet DC motors, Figure 8-5, are mounted to each of the two rear driving wheels. The motors have a maximum operating voltage of 48V and are rated at 6060W each drawing a peak continuous current of 148 amps. They have a no load speed of 3600 while a maximum loaded speed of 3200 rpm. The motors are attached to a 4:1 planetary gearbox thus reducing the effective maximum speed of the wheel to 800 rpm.



Figure 8-5: Mars Electric 0708 motor. The motor has a diameter of 9 inches.

### **8.2.3 Motor Controller**

Kelly Controls KD72V401 PWM motor controllers, Figure 8-6, are used to control the speed of each motor. They are rated at up to 72V and continuous current of 180A with peak supportable current of 400A for 2 minutes. The two means of controller motor speed through these controllers has already been stated in the previous section. These controllers have Regenerative braking capability and accept brake input as either 0-5V or 0-5kΩ. The controllers have built-in overcurrent protection and fault detection.

The 0-5V inputs of the controller enable easy integration of a microcontroller (MCU) into the system for electronic control of speed.



Figure 8-6: Kelly KD72401 motor controller

#### 8.2.4 Microcontroller

An 8-bit 20 MHz Atmega328P microcontroller is used at the heart of the electronic differential. This controller is also available as the more famous ‘Arduino’ package shown in Figure 8-7. It features 2 interrupts, 12 bidirectional digital input/output pins, 6 analog inputs with a 10-bit resolution and 6 PWM outputs. It can be programmed from the computer through either Serial-to-USB or SPI interface. The microcontroller can operate on supply voltages between 3 to 12V and accepts 5V inputs and can send 5V output signals with the maximum sink current of 40 mA on each pin.

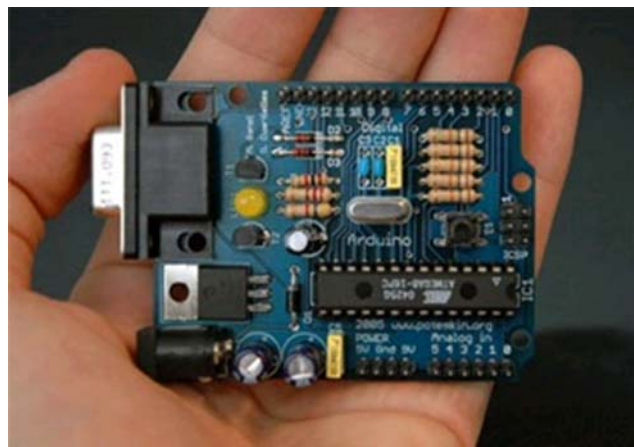


Figure 8-7: Arduino microcontroller board

### 8.2.5 Driver Input Parameters

#### 1. Throttle position sensor

A  $5K\Omega$  potentiometer pedal is used as the throttle input. The pedal interfaces with a MCU and is read as an analog signal. Since the Analog-to-Digital (A/D) converter of the MCU has a resolution of 10 bit, a 5mV resolution is achieved on all analog sensors. The actual pedal installed on the Dune Buggy is shown in Figure 8-8 below.

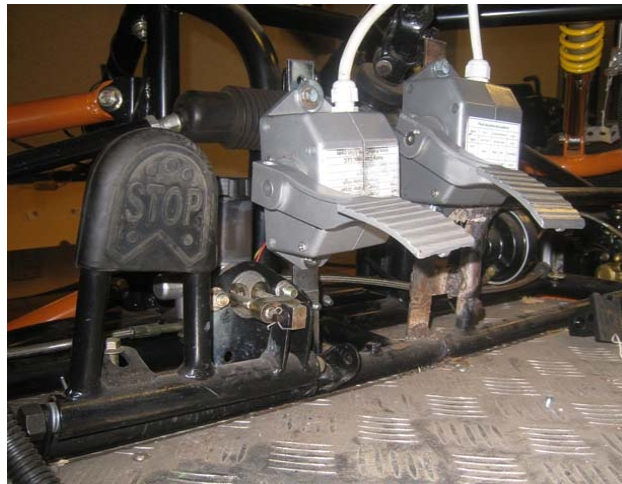


Figure 8-8: Identical electronic acceleration and brake pedals

The throttle is interfaced with the microcontroller as follows:

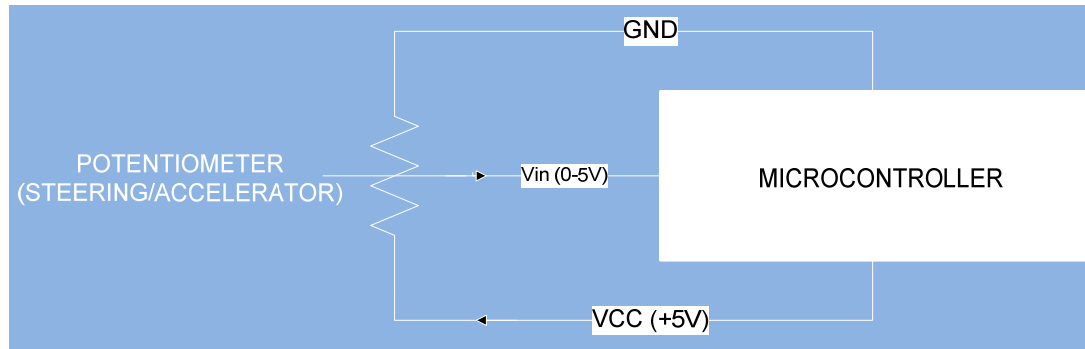


Figure 8-9: Throttle, steering Interface with MCU

#### 2. Brake position sensor

A  $5\text{K}\Omega$  potentiometer pedal is also used as the brake input. The pedal is identical to the one used for throttle and interfaces in a same manner. The MCU is programmed to ignore throttle input once it detects that the brake is being applied.

### 3. Steering position sensor

Calculation of the differential factor to be applied to the rotational speed of the two wheels requires the knowledge of the turning wheel angles. The wheel angles are themselves a function of the steering wheel angle. A close approximation of the Ackermann angle can be achieved by measuring how much each wheel turns for a fractional change in the steering wheel angle. Ultimately the steering wheel angle becomes the only input required to calculate the differential factor as determined by Eq. (8-5) and (8-9) presented earlier in this chapter.

The steering angle is measured by attaching a precision potentiometer to the steering wheel through a 1:1 gear ratio. The potentiometer is also read as an analog input by the microcontroller. The Figure 8-10 below shows the change in potentiometer reading with changing steering angle.

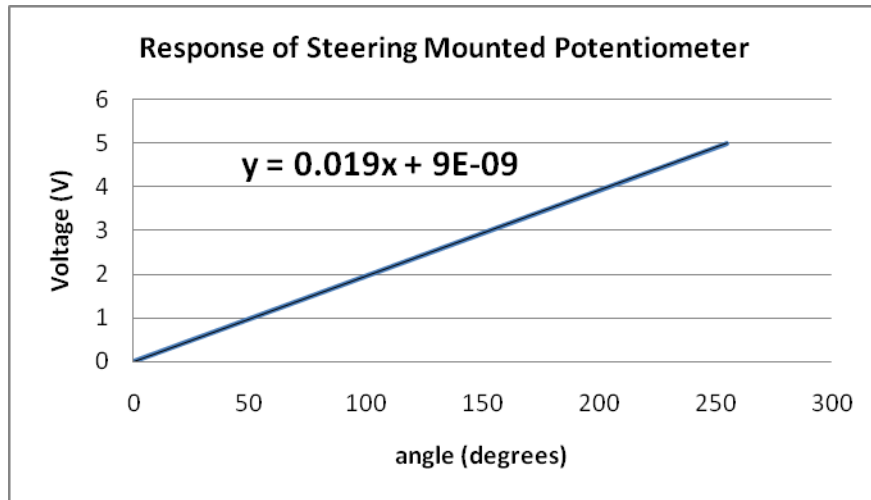


Figure 8-10: Feedback of Potentiometer mounted at the steering wheel

### 8.2.6 Feedback - RPM Measurement

The calculation of differential speed of the two motors and sending appropriate voltage signals to the two motor controllers may not result in the motors actually spinning at the desired speeds due to various uncontrollable and unforeseen factors including wear and tear of motor bearings, different load on the motor, fault in motor controllers, different surface friction and roughness etc. To ensure that the motors spin at the desired rate a closed loop PID controller needs to be implemented for which the individual wheel speed has to be monitored. Bipolar latching Hall Effect sensors have been mounted on each wheel for this purpose. These sensors switch from high output to a low output based on the magnetic pole they are exposed to i.e. exposing the sensor to north magnetic pole pulls the output high while a South Pole pulls it low. The removal of magnetic pole does not affect the output state which is why they are called ‘latched’. The Figure 8-11 shows the sensor components and the actual sensor mounted on the Buggy.

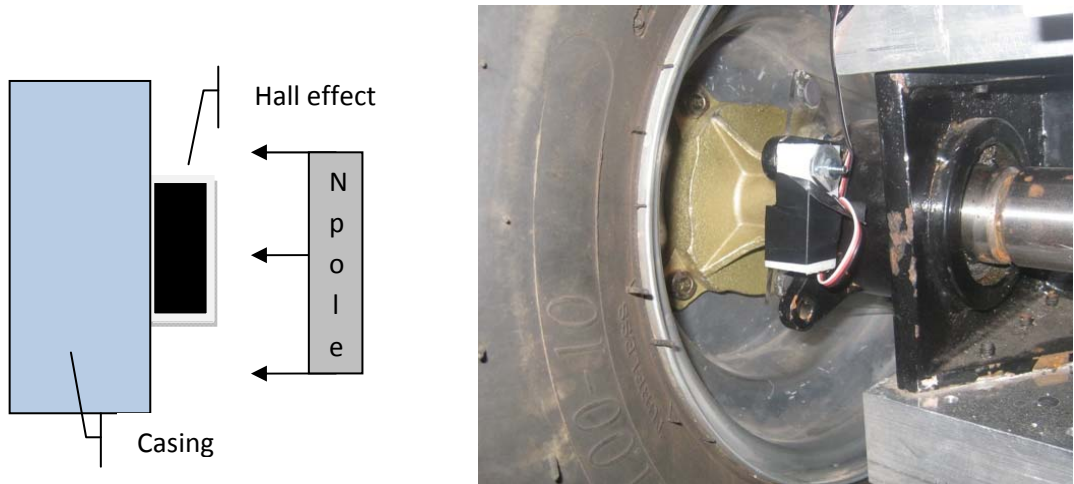


Figure 8-11: Hall effect RPM sensor

The sensor by the 5V supply of the board and switches output between 0 to 5 volt when subject to alternating magnetic fields. Figure 8-12 below shows the output from the RPM sensor mounted on the rear wheels. The different speed of the two wheels is evident from the different waveforms of the blue and red signals.

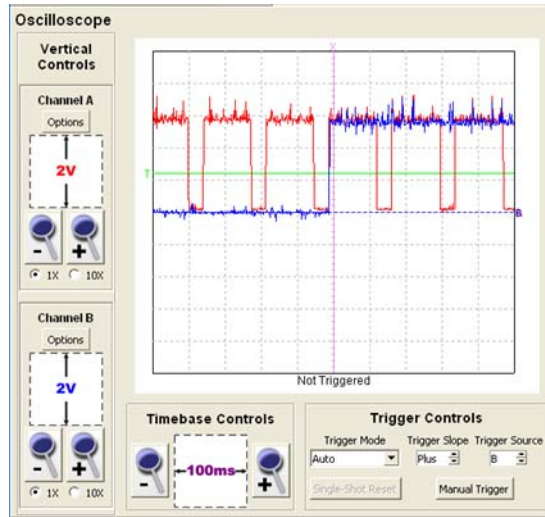


Figure 8-12: Output of Hall effect RPM sensor

## 8.3 RESULTS AND DISCUSSION

### 8.3.1 *Overall Differential System*

The system consists of RPM sensors and inputs including throttle, brake and steering interfaced with the MCU, which monitors the state of these inputs continuously and applies a corrective signal to the motor controllers. The motor controllers in turn supply the motors with the voltage/current based on the input from MCU. Figure 8-13 shows the entire system schematic.

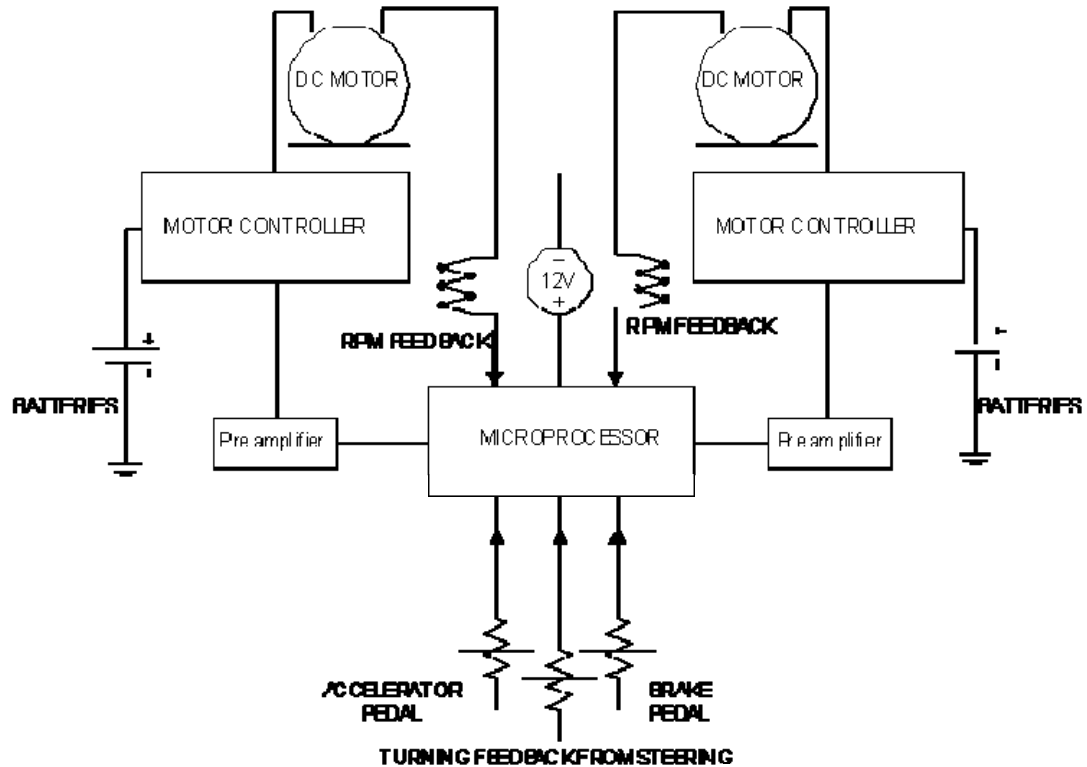


Figure 8-13: Electronic Differential schematic

### 8.3.2 Steering and Calculation of Ackermann angle

The steering has a total side to side rotation of 260 degrees i.e. 130 degrees either to left or right. The 130 degree rotation of steering results in an outer wheel angle,  $\delta_{out}$ , of 24.82 degrees and 19.38 degrees on the inner wheel,  $\delta_{in}$ . Then according to equation (8-3), the maximum Ackermann angle is:

$$\delta = \frac{\delta_{in} + \delta_{out}}{2} = \frac{24.82 + 19.38}{2} = 22.1$$

The variation in Inner wheel, Outer wheel and Ackermann angle with the changing steering angle is shown in Figure 8-14.

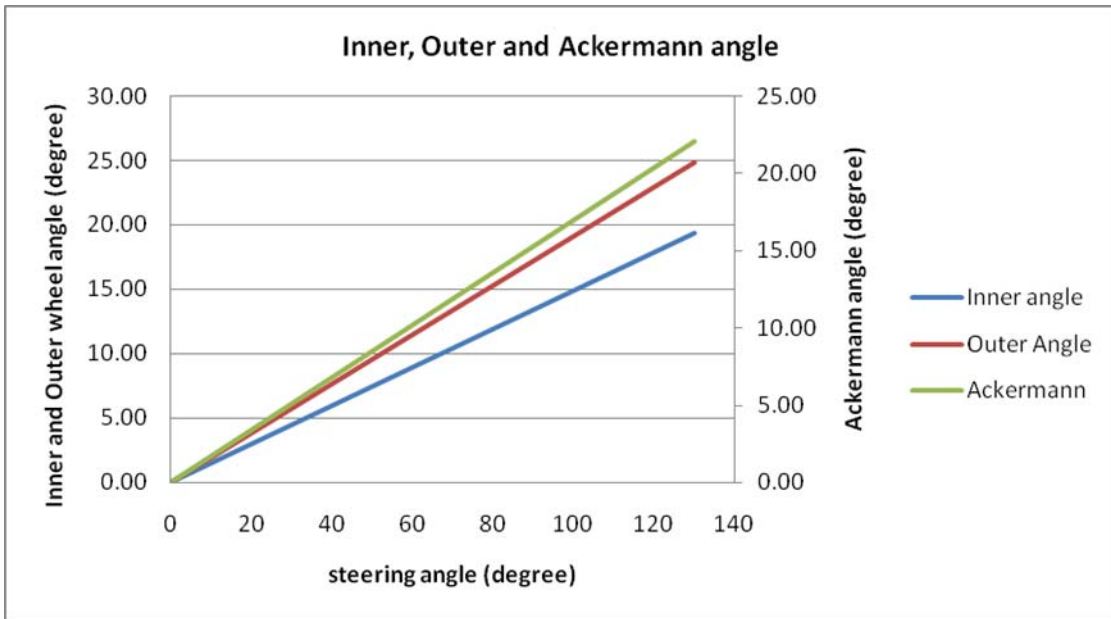


Figure 8-14: Variation in Ackermann angle with steering wheel rotation

### 8.3.3 Inner and Outer Wheel Rotational Speed Difference

The inner and outer wheel speeds are given by the numerator and denominator of equation (4). As this equation does not include the vehicle's actual speed, the two wheel rotational speeds are relative and related to each other by the factor  $x$  as given in equation (5) and to the vehicle's 'imaginary' rotational speed as per equation (8). The imaginary rotational speed is defined as the speed at which a very thin tire would rotate if placed at the horizontal center of the vehicle between the two driven wheels. Recapping the equations from the 'Theoretical Background' section:

$$\frac{\omega_{in}}{\omega_{out}} = \left( \frac{2L - d \tan(\delta)}{2L + d \tan(\delta)} \right) \quad \dots (8-4)$$

$$x = \left( \frac{2L - d \tan(\delta)}{2L + d \tan(\delta)} \right) \quad \dots (8-5)$$

$$\omega = \frac{\omega_{in} + \omega_{out}}{2} \quad \dots (8-8)$$

Table 8-3 shows the change in the inner and outer wheel rotational speeds with changing steering wheel angles. This table presents factored speeds of the two wheels that are applicable to any vehicle velocity i.e. at 60 km/h (569.6 RPM) the inner wheel's RPM would be 530 ( $0.93 \times 569.6$ ) and the outer wheel would spin at 608 RPM ( $1.07 \times 569.6$ ) when the steering is turned a full 130 degrees.

Table 8-3: Variation in Ackermann angle with steering angle

Relative Vehicle Speed (w)	Steering angle (deg)	Inner angle (deg)	Outer angle (deg)	Ackerman angle (deg)	Inner and Outer RPM difference factor (x)	amplitude difference (ad)	Inner Wheel RPM factor (w - ad)	Outer Wheel RPM factor (w + ad)
1	0.00	0	0	0	1	0	0	0
1	16.25	2.42	3.10	2.76	1.02	0.01	0.99	1.01
1	32.50	4.85	6.21	5.53	1.03	0.02	0.98	1.02
1	48.75	7.27	9.31	8.29	1.05	0.03	0.97	1.03
1	65.00	9.69	12.41	11.05	1.07	0.03	0.97	1.03
1	81.25	12.11	15.51	13.81	1.09	0.04	0.96	1.04
1	97.50	14.54	18.62	16.58	1.11	0.05	0.95	1.05
1	113.75	16.96	21.72	19.34	1.13	0.06	0.94	1.06
1	130.00	19.38	24.82	22.10	1.15	0.07	0.93	1.07

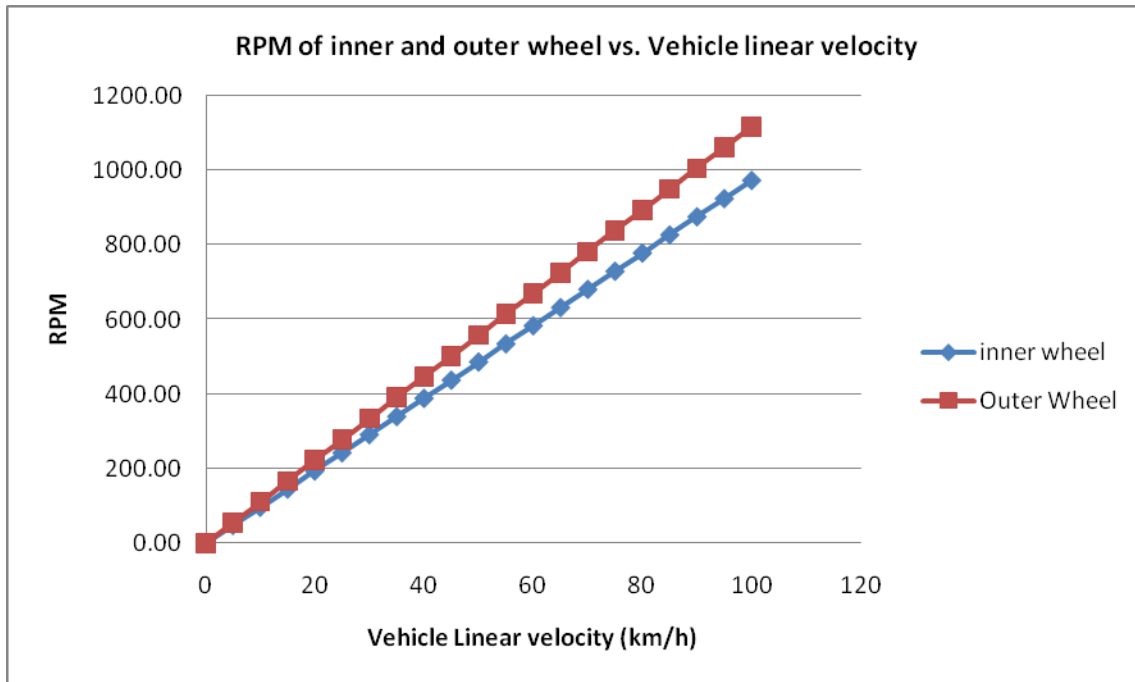


Figure 8-15 Variation in inner and outer wheel RPM with varying speed during full turn

Figure 8-15 shows the RPM of inner and outer wheels as a function of vehicle's linear velocity for a full steering turn i.e. Ackermann angle of 22 degrees.

Figure 8-16 shows the distance travelled by the inner and outer wheels as a function of Ackermann angle, which in turn is a function of steering angle.

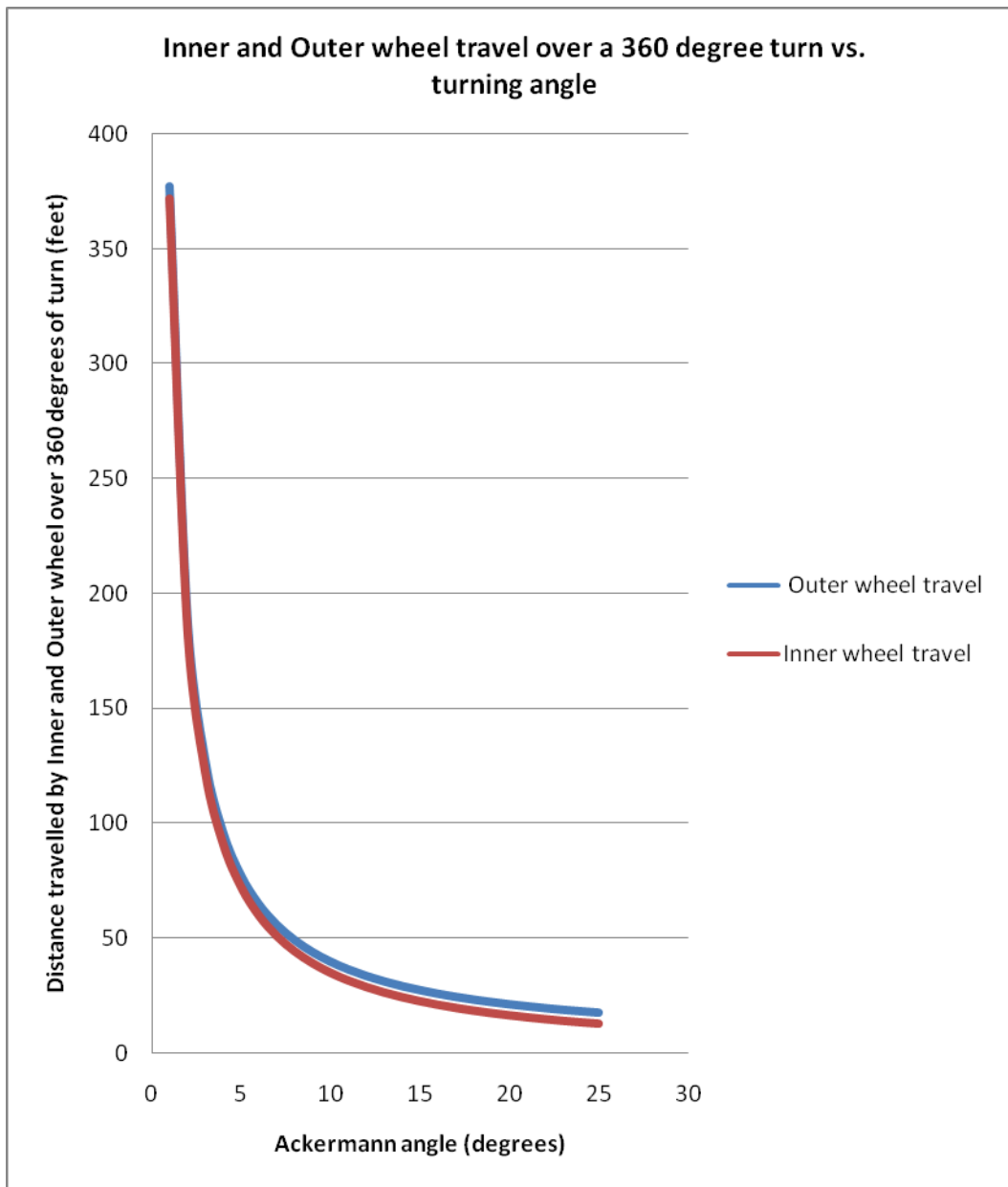


Figure 8-16: Distance travelled by inner and outer wheel during turns of various radii

### 8.3.4 Differential Software Logic

The MCU has been programmed to carry out the Electronic Differential on the Dune Buggy as shown in Figure 8-17. The MCU monitors the steering and throttle position and calculates the required factor,  $x$ , required for the differential of the two wheels. The MCU then compares the result of that calculation with the feedback RPM reading from the wheel mounted RPM sensors. If the reading from the sensor is the same as the calculated speed of the two wheels then no correction is required and the MCU maintains the signal being sent to the motor controller. The difference between the calculated speed and the RPM feedback is called the ‘error’ (err) in the speed:

$$\text{Err} = \text{Calculated speed} - \text{feedback} \dots (8-12)$$

When the error is nonzero, the MCU calculates the required correction to be applied to the signal being sent to the motor controller according to the PID equation.

As described earlier, PID controller has three parts namely Proportional, Integral and Differential and is given below:

$$\text{PID} = K_p x \text{err} + K_i x \text{err} + K_D x \text{err} \dots (8-13)$$

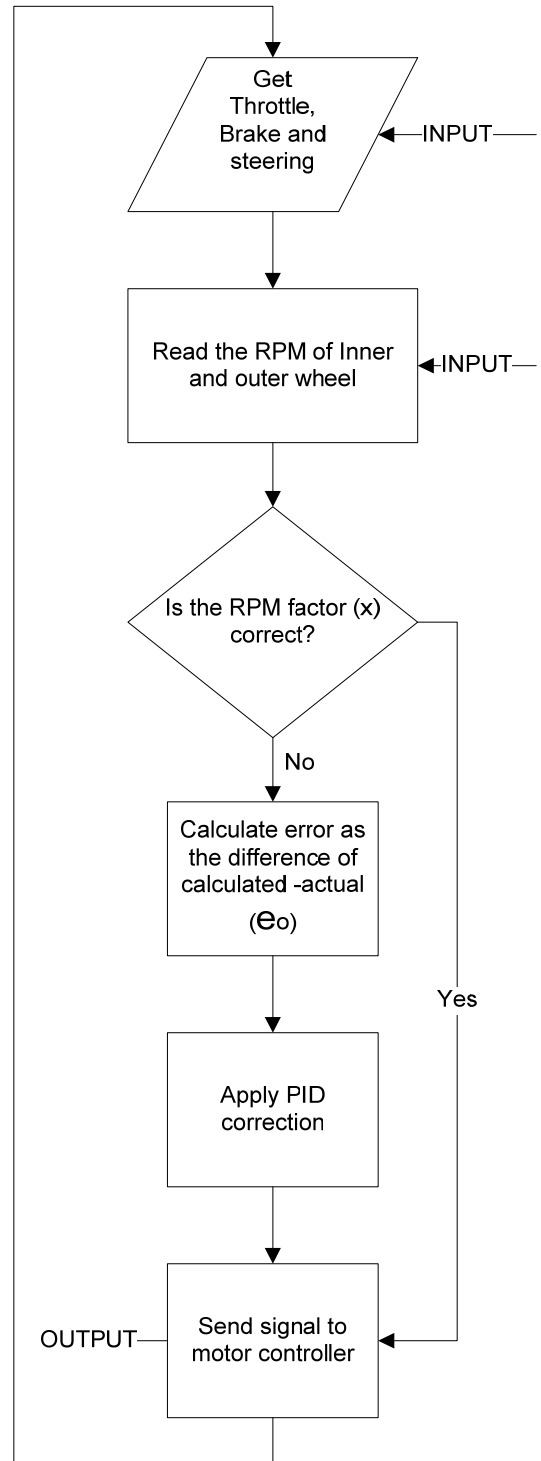


Figure 8-17: Software side PID controller logic

$K_p$ ,  $K_D$  and  $K_I$  values of 1, 1.5 and 1.5 have been used respectively.

### 8.3.5 Various PID test results

Figure 8-18 shows the test for matching the speeds of the two wheels. With the same input signal, the two wheels spin at different rates for reasons that could not be determined. To compensate for the difference in response of the two motors, speed matching algorithms were applied and tested, the results of which are shown below. The two wheels spin at different rates initially but as the speed matching routine is started, the speed difference narrows down.

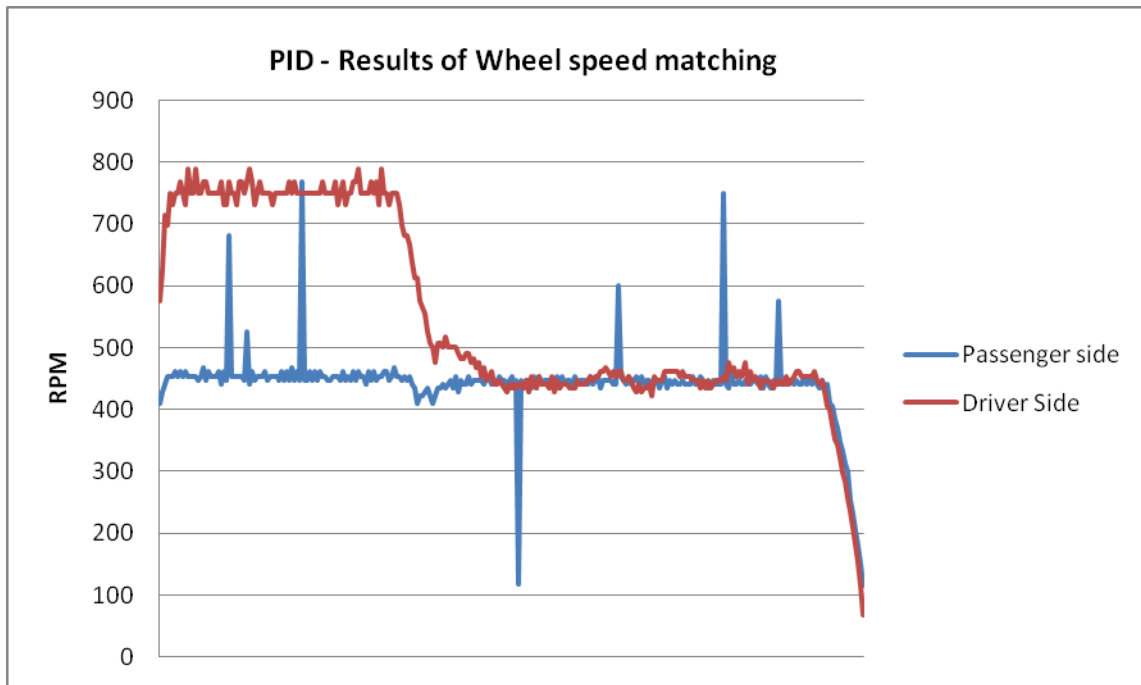


Figure 8-18: PID wheel speed matching results

Figure 8-19 shows the result of PID controller during mixed driving conditions. The five (5) regions and their description is given below:

- a) Straight line constant speed motion
- b) Deceleration during turning – Driver wheel turns at a different rate than the passenger one (right turn)
- c) Acceleration during turning – Passenger wheel turns faster than the driver side wheel (left turn)
- d) Straight line acceleration
- e) Deceleration

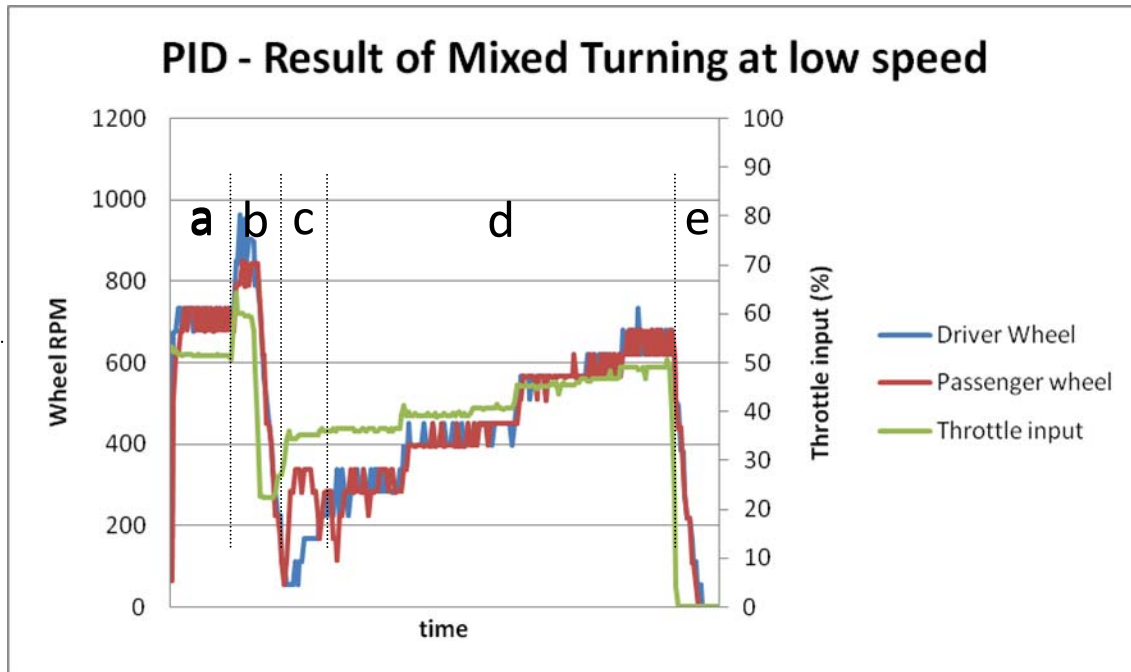


Figure 8-19: PID – Mixed turning results

Figure 8-20 shows the results of PID controller during a one sided turning at constant speed, followed by brief acceleration, deceleration and then acceleration and final total stop.

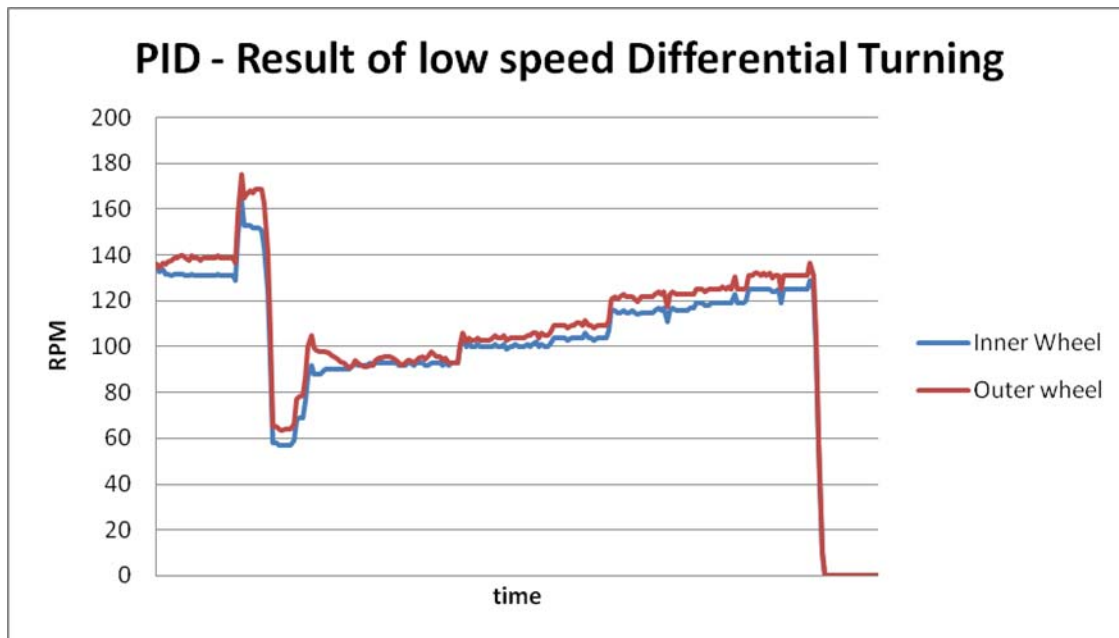


Figure 8-20: PID - low speed differential turning

#### 8.4 FURTHER TESTING

More work needs to be performed to improve the response of the electronic differential and optimize the proportional, integral and differential constant to achieve a better response from the PID controller. However, due to persistent problems with the current battery pack and extremely low usage time of less than 5 minutes further testing is very difficult to conduct. The battery pack has been redesigned and is under thorough examination including repetitive battery charging and discharging cycles. Once the state of the current battery pack is determined, it will either be reinstalled or replaced followed by continuation of testing and improvements.

## 9. COST

Besides multifunctionality, another attractive feature of the composite made here is its low cost. Each piezoceramic bender used for all the projects costs less than \$2. A four (4) layer PZT bimorph stack costs \$9 if a single unit is produced, with the cost dropping down to **\$5** if 100 units are produced. These prices are based on the present market price of the PZT bimorph elements used in this research and are not a projection of cost for an approximate mass production number unlike other research papers. The THUNDER element used by Kymisis [18] costs in excess of \$100 per unit and the PVDF stack costs more than \$200; based on a price of \$250 for a 8.5" x 11" sheet of 110  $\mu\text{m}$  metallized and polished PVDF sheet offered by Measurement Specialities [46].

As discussed previously, reduction of components and elimination of motion detection circuit reduces the overall cost of the sensors. Even in applications where PZT harvesters replace batteries such as TPMS module, the price remains unaffected as batteries cost as much if not more than PZT. Hence, not only is the energy harvesting approach better from design perspective but also economical making it a highly practical candidate for TPMSs.

## **10. FUTURE WORK**

A PVDF based composite is under development for use on high deformation surfaces of the tire which can be employed to harvested power from sidewalls. It will consist of 6 inch square PVDF films sandwiched between metallic foils, reducing the number of benders down from 160 to a mere 10 simplifying construction as well as electrical circuitry.

For sensor applications, further experimentation is required to reduce the size of PZT harvesters reducing overall size and weight of module. It is also favourable to improve the bendability of piezoelectric harvesters without significantly compromising power output. PZT fibres have already been proven to have high deformation making them an ideal candidate for such tire based applications.

The Tire pressure sensor and Vehicle Speed Sensor developed in this research project will be installed on the Dune Buggy to be used as primary sensors for the operation of Electronic Differential.

## **11. CONCLUSION**

Multifunctional layered composites were successfully developed using PZT layers for power generation in shoes and tires. Embedding these components within structural layers improves the value of the overall system. The primary approach of power harvesting in tires and shoes relies on the bending of PZT elements attached to and embedded within the system in question and provide sufficient output to power various sensors. In case of tires, sufficient power can be generated and taken on to the chassis to recharge batteries or run onboard electronics.

In TPMS modules, PZT harvesters replace batteries by allowing the generation of power within the wheel using its inherent motion. Piezoelectric elements themselves are used in a multifunctional way in the Vehicle Speed Sensor by providing power for the sensor, sensing the rotation of the wheel and allowing the detection of vehicle motion necessary for putting the sensor to low power sleep mode and wakeup when required.

The feasibility of using piezoelectric materials in Multifunctional composites for use in Automotive as well as other mobile system has successfully been demonstrated.

The preexisting setup of the Dune Buggy was modified to incorporate the Electronic Differential mimicking the effects of a mechanical differential used in typical commercial vehicles. Sensors were installed to monitor the RPM of the wheels, electronic inputs for throttle, brake and steering position were included and programmed using a microcontroller to achieve the differential affect on the two rear driven wheels on the Dune Buggy. The microcontroller programming was based on the PID control method and the results were experimentally verified.

## REFERENCES

- [1] Kagan, V., A., "Understanding of a New Paradigm in High Modulus Nylon 6 Grades for Load Bearing and Light Weight Applications", *The Journal of Injection Molding Technology, Society of Plastic Engineers (SPE)*, 6(1): 18-36, Mar. 2006.
- [2] Khameneifar, F. and Arzanpour, S., "Energy Harvesting From Pneumatic Tires Using Piezoelectric Transducers", *ASME Conference on Smart Materials, Adaptive Structures and Intelligent Systems, ASME 2008*, pp. 331-337, 2008. doi: 10.1115/SMASIS2008-426
- [3] Dixon, B., Kalinin, V., Beckley, J., and Lohr, R., "A Second Generation In-Car Tire Pressure Monitoring System Based on Wireless Passive SAW Sensors", *International Frequency Control Symposium and Exposition, IEEE 2006*, pp.374-380, 2006.
- [4] Shaout, A., and Jarrah, M. A, "Cruise control technology review", *Computers & Electrical Engineering*, Volume 23, Issue 4, pp. 259-271, 1997. doi: 10.1016/S0045-7906(97)00013-X
- [5] Pereira, T., Guo, Z., Nieh, S., Arias, J., and Hahn, H. T., "Embedding thin-film lithium energy cells in structural composites", *Composites Science and Technology*, Volume 68, Issues 7-8, pp. 1935-1941, June 2008. doi: 10.1016/j.compscitech.2008.02.019.
- [6] Monti, M., Natali, M., Petrucci, R., Kenny, J. M., and Torre, L., "Carbon nanofibers for strain and impact damage sensing in glass fiber reinforced composites based on an unsaturated polyester resin". *Polymer Composites*, Volume 32, Issue 5, pp. 766–775. Apr. 2011. doi: 10.1002/pc.21098
- [7] Gautier, K. B., L'Hostis, G., Laurent, F., and Durand, B., "Mechanical performances of a thermal activated composite", *Composites Science and Technology*, Volume 69, Issues 15-16, pp. 2633-2639, Dec. 2009. doi: 10.1016/j.compscitech.2009.08.004.

- [8] Liu, P., Sherman, E., and Jacobsen, A., “Design and fabrication of multifunctional structural batteries”, *Journal of Power Sources*, Selected Papers presented at the 14th INTERNATIONAL MEETING ON LITHIUM BATTERIES (IMLB-2008), Volume 189, Issue 1, pp. 646-650, Apr. 2009, doi: 10.1016/j.jpowsour.2008.09.082.
- [9] Schwartz, M. M. ,*Smart material*, CRC Press, 2009
- [10] APC International, “Piezoelectricity”, Retrieved Aug. 2010, from [http://www.americanpiezo.com/piezo\\_theory/piezo\\_theory.pdf](http://www.americanpiezo.com/piezo_theory/piezo_theory.pdf), 2002.
- [11] Heywang, W., Lubitz, K., Wersing, W. (Eds), “Piezoelectric PZT Ceramics”, *Helke ,G.,Lubitz, K, Piezoelectricity: Evolution and Future of a Technology*, pp. 89-130, Springer, 2008.
- [12] Malysh, T., and Erhart, J., “Electric Field Applicability Limits for PZT Ceramics”, *Ferroelectrics*, Volume 319, Issue 1, 2005.
- [13] Cheng, C. H., Chen, S.C., Kuo, H. C., and Chou, Z. B., “The poling design of a shear mode piezoelectric actuator”, *Journal of Micromechanics and Microengineering*, Volume 15, Issue 11, 2005. doi: 10.1088/0960-1317/15/11/024
- [14] Ostaševičius, V., Milašauskaitė, I. , Daukševičius, R., and Baltrušaitis, V., “Experimental characterization of material structure of piezoelectric PVDF polymer”, *Mechanika*, Volume 6, pp. 78-82, 2010
- [15] Sencadas, V., Lanceros-Méndez, S., and Manob, J.F., “Characterization of poled and non-poled [beta]-PVDF films using thermal analysis techniques”, *Thermochimica Acta*, Volume 424, issues 1-2, Dec. 2004. doi: DOI: 10.1016/j.tca.2004.06.006.
- [16] Measurement Specialities, “Piezo film sensors – Technical Manual”, *Measurement Specialities*, Retrieved Aug. 2010 from <http://www.media.mit.edu/resenv/classes/MAS836/Readings/MSI-techman.pdf>
- [17] Professional Plastics, “Kynar film datasheet”, *Professional Plastics*, Retrieved Aug. 2010 from <http://www.professionalplastics.com/professionalplastics/content/PVDFFilmDataSheet.doc>

- [18] Kymissis, J., Kendall, C., Paradiso, J., and Gershenfeld, N., "Parasitic power harvesting in shoes," *Wearable Computers, 1998. Digest of Papers. Second International Symposium on*, vol., no., pp.132-139, 19-20, Oct. 1998. doi: 10.1109/ISWC.1998.729539
- [19] Ding, H., and Kaajakari, V., "Microstructured Polymer For Shoe Power Generation", *Solid-State Sensors, Actuators and Microsystems Conference, 2009. TRANSDUCERS 2009. International*, pp.1393-1396, Jun. 2009. doi: 10.1109/SENSOR.2009.5285832
- [20] H. A Sodano., D. J. Inman, Comparison of piezoelectric energy harvesting devices for recharging batteries. *J. Intell. Mater. Syst. Struct.*, 2005, 16(10), 799–807
- [21] Electronics Lab, "How to rebuild a Li-Ion battery pack", *Electronics Lab*, Retrieved Nov. 2010 from [http://www.electronics-lab.com/articles/Li\\_Ion\\_reconstruct/](http://www.electronics-lab.com/articles/Li_Ion_reconstruct/)
- [22] Face International, "Thunder Actuators", *Face International*, Retrieved Jun. 2010 from <http://www.prestostore.com/cgi-bin/pro23.pl?ref=thunderonline&ct=36234>
- [23] Fourie, D., "Shoe-Mounted PVDF Piezoelectric Transducer for Energy Harvesting", *MIT*, 2002.
- [24] Manla, G., White, N.M., and Tudor, J., "Harvesting energy from vehicle wheels", *Solid-State Sensors, Actuators and Microsystems. Transducers 2009*, pp. 1389-1392, Oct. 2009. doi: 10.1109/SENSOR.2009.5285831
- [25] Milao, A.V., "Method for Generating An Electric Current Within A Tyre", *U.S. Patent Application Publication*, US 2003/0000615 A1, Feb. 2003.
- [26] Tyndall, P, "Power conversion from piezoelectric source", *European Patent Application*, EP 1612059 A1, Jan. 2006.
- [27] Mancosu, F., Matrascia, G., Villa, D., "Vehicle Tire And System For Generating Electrical Energy In The Tire", *U.S. Patent*, US 6992423B2, Jan. 2006.
- [28] Velupillai, S., Guvenc, L., "Tire Pressure Monitoring [Applications of Control]," *Control Systems, IEEE*, Volume 27, Issue 6, pp. 22-25, Dec. 2007.doi: 10.1109/MCS.2007.909477

- [29] Toyota, "Protect What You Believe In" , *Toyota Tundra – Features and Benefits*, Retrieved Sep. 2010,  
<http://www.toyota.ca/toyota/en/vehicles/tundra/features-benefits/safety>
- [30] Löhndorf, M., Kvisterøy, T., Westby, E., and E. Halvorsen, "Evaluation of energy harvesting concepts for tire pressure monitoring systems of a micro-electric generator for microsystems", *Technical Digest PowerMEMS 2007*, Freiburg, Germany, pp. 331–334, 2007.
- [31] Ostertag, T., and Kunzmann, S., "Batteryless tire pressure monitoring system with bulk acoustic resonators", *IQ-Mobil GmbH*, Germany, Nov. 2003.
- [32] Wu, Liji, Wang, Y., Jia, C., and Zhang, C., "Battery-less piezoceramics mode energy harvesting for automobile TPMS." *IEEE 8th International Conference on ASIC.*, pp. 1205 – 1208, Oct. 2009. Doi: 10.1109/ASICON.2009.5351190
- [33] Ho, I., Chung, J., Chen, H., and Chiu, H., "A Battery-Less Tire Pressure Monitoring System," *Vehicular Technology Conference, 2009. IEEE 69th*, pp.1-5, April. 2009. Doi: 0.1109/VETECS.2009.5073285
- [34] Piezotag Limited, "Piezotag", Retrieved Sep. 2010 from  
<http://www.piezotag.com/>
- [35] Sakai, I., Chilton, N.J., Pacaud, S.J., Hazelden, R.J., and Prosser, S.J., "Optical speed-over-ground sensors for on-board vehicle speed measurement" *IEEE Colloquium on Automotive Sensors*, pp.7/1-7/3, May 1992.
- [36] Makki, N., Pop-Iliev, R., "Pneumatic Tire-based Piezoelectric Power Generation", *Proceedings of SPIE Smart Structures/NDE*, Volume 7977, Mar. 2011. doi:10.1117/12.880636
- [37] Parmatex, "Parmatex Super Weather strip adhesive datasheet", Retrieved Nov. 2010 from <http://www.permatex.com/documents/tds/Automotive/81731.pdf>
- [38] Makki, N., Pop-Iliev, R., "Piezoelectric power generation for sensor applications: Design of a battery-less wireless tire pressure sensor", *Proceedings of SPIE Microtechnologies*, Volume 8066, Apr. 2011. doi:10.1117/12.887112
- [39] Makki, N., Pop-Iliev, R., "In-wheel Piezoelectric Wireless Rpm Sensor" *Proceedings of CANCAM 2011*, May. 2011.

- [40] Bernacki, M. “Design And Development Of An Extended Range Electric Bywire/Wireless Hybrid Vehicle With A Near Wheel Motor Drivetrain”, *MASc. thesis at UOIT*, May 2009.
- [41] Crolla, D.A., “Chapter 5: Transmission and Driveline”, Happian-Smith, J., *Automotive Engineering: Powertrain, Chassis System and Vehicle Body*, pp. 105-140, Butterworth-Heinemann, 2009.
- [42] F1-dictionary, “Differential”, Retrieved Nov. 2009 from [http://f1-dictionary.110mb.com/Images/differential\\_limited\\_slip.jpg](http://f1-dictionary.110mb.com/Images/differential_limited_slip.jpg)
- [43] Jazar, R.N., “Chapter 2: Vehicle dynamics”, *Vehicle dynamics: theory and applications*, Springer, pp. 379-451, 2008.
- [44] Polka, D., “Chapter 5: Drive control and feedback devices”, *Motors & Drives: A Practical Technology Guide*, pp. 205-229, ISA, 2003.
- [45] Xue, D., Chen, Y., and Atherton, D.P., “Chapter 6: PID controller design”, *Linear Feedback Control: Analysis and Design with MATLAB*, pp. 183-218, SIAM, 2007.
- [46] Measurement Specialities, “PVDF Piezoelectric film sheets”, *Measurement Specialities*. Retrieved Aug. 2010 from <http://www.meas-spec.com/piezo-film-sensors/piezo-film-sheets.aspx>.